Supporting information for:

Combining Metal-Metal Cooperativity, Metal-Ligand Cooperativity and Chemical Non-Innocence in Diiron Carbonyl Complexes

Cody B. van Beek,[a] Nicolaas P. van Leest,[b] Martin Lutz,[c] Sander D. de Vos,[a] Robertus J. M. Klein Gebbink,[a] Bas de Bruin,[b] and Daniël L. J. Broere*[a]

[a] Organic Chemistry and Catalysis, Debye Institute for Nanomaterials Science, Faculty of Science, Utrecht University Universiteitsweg 99, 3584 CG, Utrecht (The Netherlands)

[b] Homogeneous, Supramolecular and Bio-Inspired Catalysis Group, Van 't Hoff Institute for Molecular Sciences, University of Amsterdam, Science Park 904, 1098 XH Amsterdam (The Netherlands)

[c] Structural Biochemistry Chemistry, Bijvoet Centre for Biomolecular Research, Faculty of Science, Utrecht University, Universiteitsweg 99, 3584 CG (The Netherlands)

Table of Contents

Experimental methods

General considerations

All manipulations were performed under inert atmosphere using standard Schlenk techniques or inside of a N_2-filled M. Braun glovebox using dry solvents and reagents, unless stated otherwise. Glassware was dried at 130 °C under a dynamic vacuum, unless noted otherwise. Hexane, Et_2O and toluene were collected from an M. Braun MB-SPS-800 solvent purification system and degassed and stored over 4 Å molecular sieves. THF was dried over benzophenone/sodium, distilled and degassed, subsequently followed by storage over 4 Å molecular sieves. Benzene (Scharlab, >99%), pentane (technical, VWR chemicals) and anisole (anhydrous, Sigma) were degassed, then dried and stored over 4 Å molecular sieves. All non-deuterated solvents were degassed by bubbling N_2(g) through the solvent for at least 30 min. The solvents (1.0 mL) were tested with a standard purple solution of sodium benzophenone ketyl in THF to confirm effective oxygen and water removal (max 1-2 drops for most solvents, max 4 drops for THF and Et_2O). All solvents were checked for water content by Karl-Fischer titration and should be well below 5 ppm for all solvents. Deuterated solvents were obtained from Cambridge Isotope Laboratories except for THF-d_8, which was obtained from ABCR, degassed by the standard freeze-pump-thaw procedure and stored over 4 Å molecular sieves. All commercial reagents were used as received and were obtained from Sigma Aldrich or Acros ($Fe_2(CO)_9$, Et_3NHCl, *n*-butyllithium 1.6 M in hexanes, anhydrous Na_2SO_4). 2,7-dimethyl-1,8-naphthyridine[1], 2,4,6-tri-*tert*-butyl phenoxyl radical[2], 9-(perfluorophenyl)-9H-fluorene[3], 9-phenyl-9*H*-fluorene[4] and triethyl ammonium hexafluorophosphate (TEA)[5] were synthesized according to reported procedures. NMR data was recorded on an Agilent MRF 400 equipped with a OneNMR probe and Optima Tune system or a Varian VNMR-S-400 equipped with a PFG probe at 298 K. All chemical shifts are reported in the standard δ notation of parts per million, referenced to the residual solvent peak. All resonances in ^{1}H NMR and ^{13}C NMR spectra were referenced to residual solvent peaks (^{1}H NMR: 7.16 for C_6D_6, 3.58 for THF-d_8, ^{13}C NMR: 128.06 for C_6D_6, 67.57 for THF-d_8). The resonances in the ^{31}P NMR spectra are referenced using the absolute reference method from a correctly referenced ^{1}H NMR spectrum of the same sample. The assignment of peaks is based on relative integration, chemical shift, and 2D NMR analysis (COSY and HMBC experiments).

IR-data was recorded on a PerkinElmer SpectrumTwo Infrared Spectrophotometer equipped with an ATR-probe. IR-analysis of air-sensitive compounds was performed by dropcasting a THF solution onto the ATR crystal, which was covered by a continues N_2(g) flow. Elemental analysis was performed by MEDAC Ltd. based in the United Kingdom. Electrospray Ionization (ESI) measurements were performed using an Advion Expression CMS mass spectrometer.

Solutions of the irradiated samples were placed in either Schlenk flasks or NMR tubes with a J-Young valve. Cyclic voltammetry measurements were performed with an IVIUM potentiostat/galvanostat using a glassy carbon working electrode, a Pt wire counter electrode, and a silver wire pseudoreference electrode. All measurements were performed inside an N_2-filled glovebox in THF containing 0.2 M $[Bu_4N]PF_6$ as electrolyte. Potentials were referenced to the $Cp_2Fe^{0/+}$ couple using an internal ferrocene standard. The potentiostat was coupled with IviumSoft software for data collection and processing. X-band EPR spectra were acquired on a Bruker EMX X-band spectrometer, equipped with an ER 4112HV-CF100 helium cryostat and a Hoenle Bluepoint 4 light source, and further analyzed and simulated using EasySpin[6] via the cwEPR GUI.[7] Headspace analysis was performed by GC using a GAS CompactGC$^{4.0}$ with grade 5 nitrogen as carrier gas. A sample was collected and measured every four minutes using a

FID for most components. Hydrogen gas was detected using a TCD on four different channels resulting in a measurement every minute.

Syntheses

Synthesis of ^{iPr}PNNP

The 2,7-bis((diisopropylphosphaneyl)methyl)-1,8-naphthyridine (^{iPr}**PNNP**) ligand was prepared as an air sensitive off-white solid in 41% yield through a procedure analogous to that previously reported for the ^{tBu}**PNNP** ligand.[1] The ^{1}H, ^{13}C and ^{31}P NMR spectra in C_6D_6 at 298 K of ^{iPr}**PNNP** show the expected number of resonances for a C_{2v}-symmetric compound. The ^{31}P{^{1}H} NMR spectrum shows a singlet at δ = 11.8 ppm, which is comparable to the mononucleating lutidine-derived ^{iPr}**PNP** ligand.[8] In comparison with ^{tBu}**PNNP**, ^{iPr}**PNNP** displays higher solubility and even dissolves in alkanes.

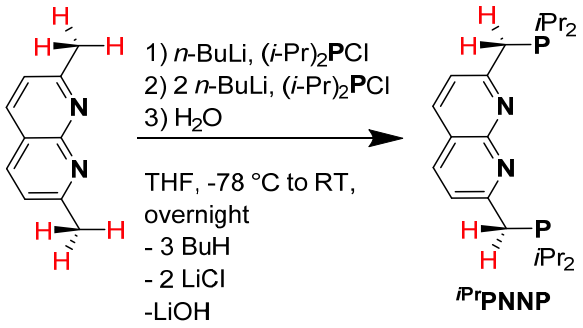

^{iPr}**PNNP**

A Schlenk flask was charged with 2,7-dimethyl-1,8-naphthyridine (3.00 g, 19.0 mmol) and THF (90 mL) and cooled to -78 °C for 40 min. *n*-BuLi (1.6 M in hexanes, 12 mL, 19 mmol, 1 equiv) was added dropwise *via* syringe over the course of ten minutes giving a dark red solution, which was afterwards allowed to warm to ambient temperature. Immediately after the mixture was warmed to ambient temperature, the red solution was cannulated to a stirring solution of P(*i*-Pr)$_2$Cl (3.1 mL, 3.0 g, 19 mmol, 1 equiv) in THF (30 mL) at -78 °C over the course of 20 min. The thick* brown suspension was stirred vigorously while warming to ambient temperature to give a brown solution. This mixture was again cooled to -78 °C forming a yellow-brown suspension to which *n*-BuLi (1.6 M in hexanes, 24 mL, 38 mmol, 2 equiv) was slowly added *via* syringe over the course of 30 min under manual and magnetic stirring. The dark red solution was allowed to warm to ambient temperature and was cannulated to a stirring solution of P(*i*-Pr)$_2$Cl (3.1 mL, 3.0 g, 19 mmol, 1 equiv) in THF (30 mL) at -78 °C. The resulting dark red solution was allowed to warm to ambient temperature. After stirring for 18 h, the dark red mixture was cooled to 0 °C and subsequently quenched with degassed water (30 mL) over the course of 10 min. The resulting orange/yellow biphasic mixture was stirred for 1 h after which volatile organics were removed under a dynamic vacuum. The resulting aqueous suspension was extracted with Et_2O (4 x 40 mL). The extracts were combined, dried over anhydrous Na_2SO_4 (35 g) and concentrated to approx. 20 mL.** The mixture was transferred into a N_2-filled glovebox and cooled to -40 °C. After 2 h, a first crop of pink crystalline material was filtered off, washed with cold (-40 °C) hexane (15 mL) and Et_2O (5 mL), and dried under a dynamic vacuum to give an off-white solid (2.02 g). The mother liquor was combined with the washings, concentrated to approx. 10 mL and cooled at -40 °C. After 16 hours a second crop of crystals was filtered off, washed with cold (-40 °C) hexane (25 mL) and dried under a dynamic vacuum to give a pinkish-white solid (1.05 g). Both the first and second crop contained the monosubstituted PNN compound as a minor impurity of 1% and 5%, respectively. Combined yield 3.07 g, 7.67 mmol, 41%.

* The thick brown suspension can make proper stirring challenging, so the use of a large stir bar is advised.

** The off-white solid that crystallized during the concentration redissolved upon warming to ambient temperature.

^{1}H NMR (400 MHz, Benzene-d_6, 298 K): δ 7.40 (d, $^{3}J_{H,H}$ = 8.3 Hz, 2H), 7.30 (d, $^{3}J_{H,H}$ = 8.3 Hz, 2H), 3.17 (d, $^{2}J_{H,P}$ = 1.8 Hz, 4H), 1.71 (heptd, $^{3}J_{H,H}$ = 7.1 Hz, $^{2}J_{H,P}$ = 1.6 Hz, 4H), 1.05 (dd, $^{3}J_{H,H}$ = 7.1 Hz, $^{3}J_{H,P}$ = 11.3 Hz, 12H), 0.99 (dd, $^{3}J_{H,H}$ = 7.1 Hz, $^{3}J_{H,P}$ = 13.6 Hz, 12H).

^{13}C {^{1}H} NMR (101 MHz, Benzene-d_6, 298 K): δ 165.1 (d, $^{2}J_{C,P}$ = 9.8 Hz), 156.4, 136.3, 122.3 (d, $^{3}J_{C,P}$ = 6.9 Hz), 119.1, 34.3 (d, $^{1}J_{C,P}$ = 24.2 Hz), 24.1 (d, $^{1}J_{C,P}$ = 15.7 Hz), 20.0 (d, $^{2}J_{C,P}$ = 15.4 Hz), 19.2 (d, $^{2}J_{C,P}$ = 10.6 Hz).

^{31}P{^{1}H} NMR (162 MHz, Benzene-d_6, 298 K): δ 11.8 (s).

Anal. Calcd. For $C_{22}H_{36}N_2P_2$: C, 67.67; H, 9.29; N, 7.17. Found C, 67.12; H, 9.48; N, 7.14.

ATR-IR (film, N_2 flow): ν = 3052 (w), 3007 (m), 2962 (s), 2947 (s), 2924 (s), 2889 (m), 2866 (s), 1935 (w), 1604 (s), 1541 (m), 1505 (s), 1462 (m), 1385 (w), 1365 (w), 1312 (m), 1238 (m), 858 (m) cm^{-1}.

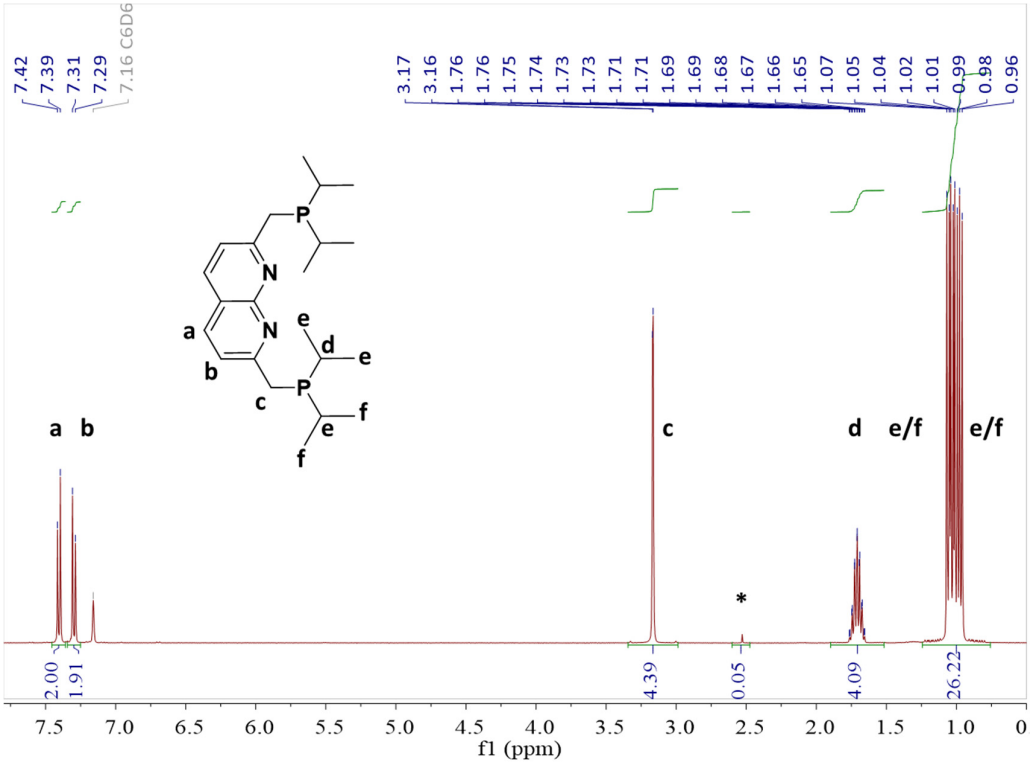

Figure S1: The ^{1}H NMR spectrum of the first crop of crystals of **^{iPr}PNNP** in C_6D_6 at 298 K. The resonance with the star is attributed to the monosubstituted PNN compound.

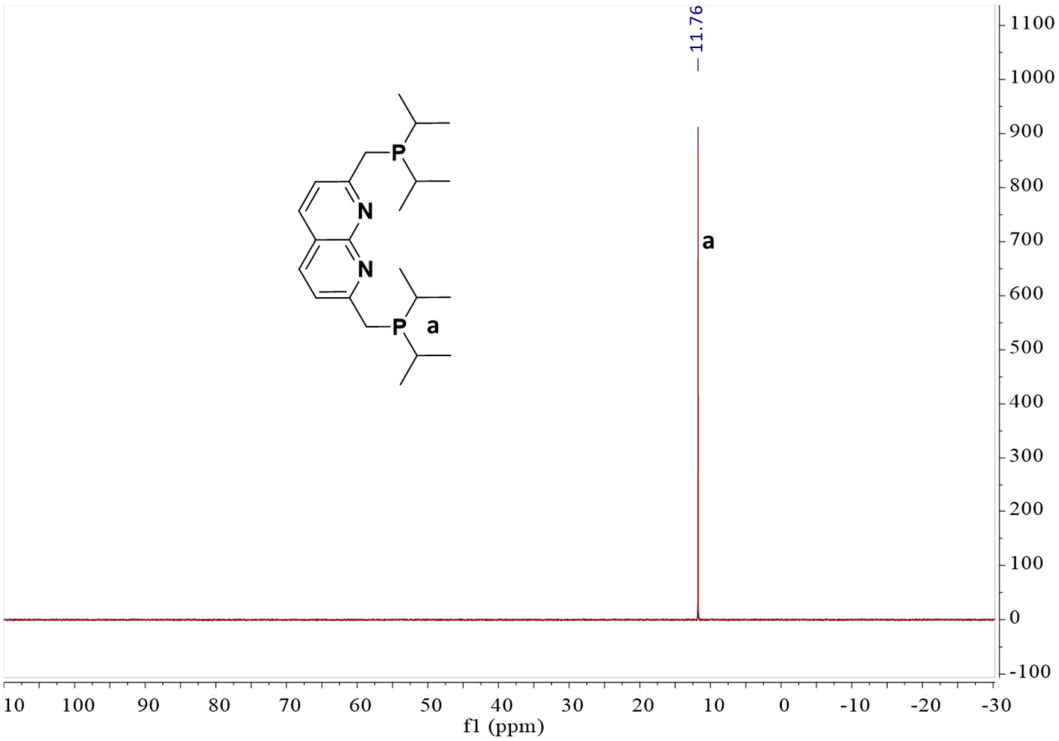

Figure S2: The $^{31}P\{^{1}H\}$ NMR spectrum of the first crop of crystals of ^{iPr}**PNNP** in C_6D_6 at 298 K.

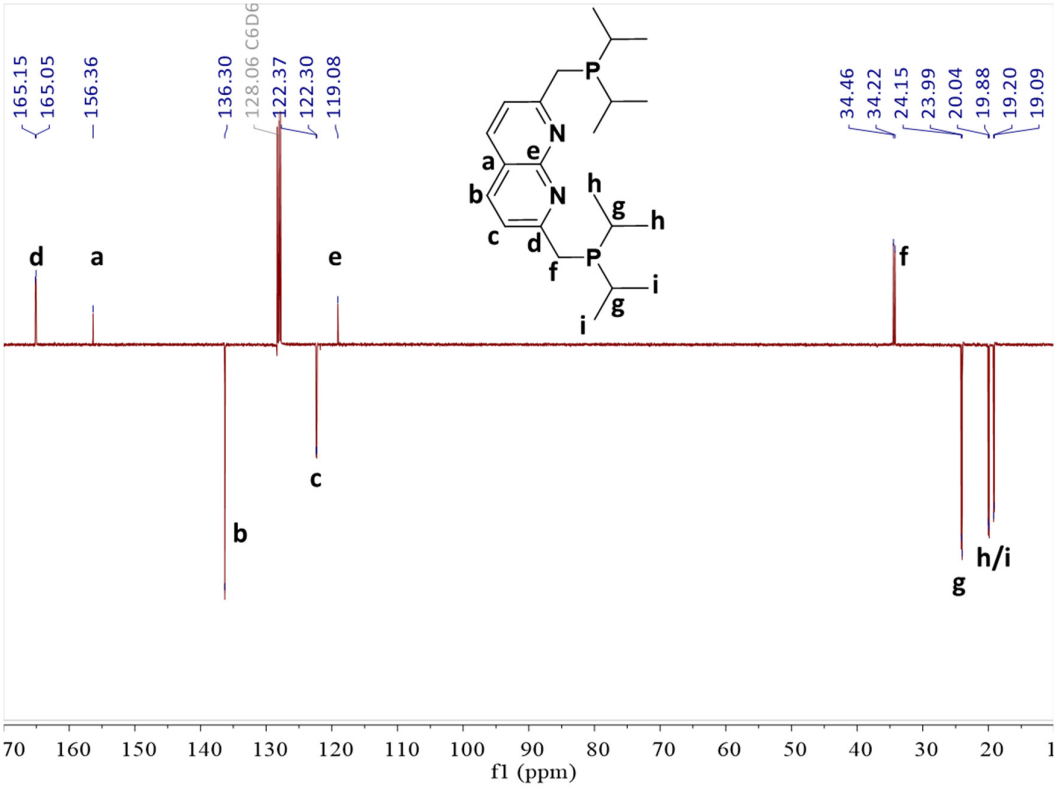

Figure S3: The ^{13}C (APT) NMR spectrum of the first crop of crystals of ^{iPr}**PNNP** in C_6D_6 at 298 K.

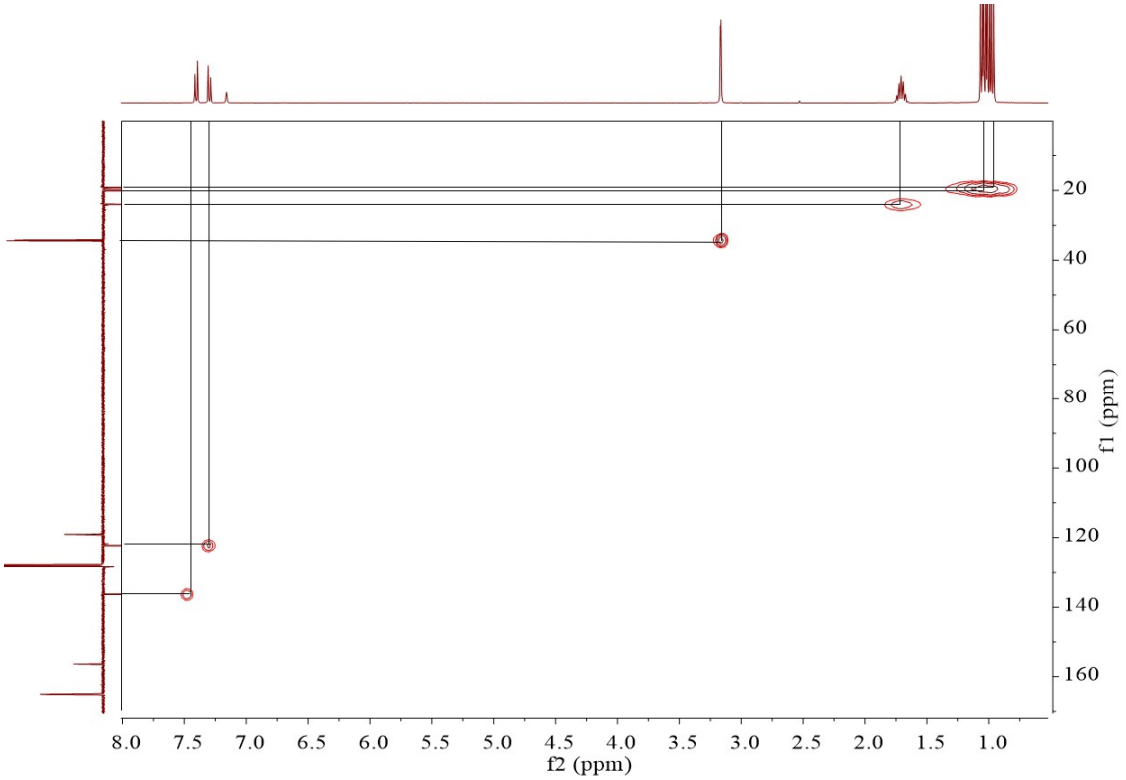

Figure S4: The ^{1}H-^{13}C HMQC NMR spectrum of the first crop of crystals of ^{iPr}**PNNP** in C_6D_6 at 298 K.

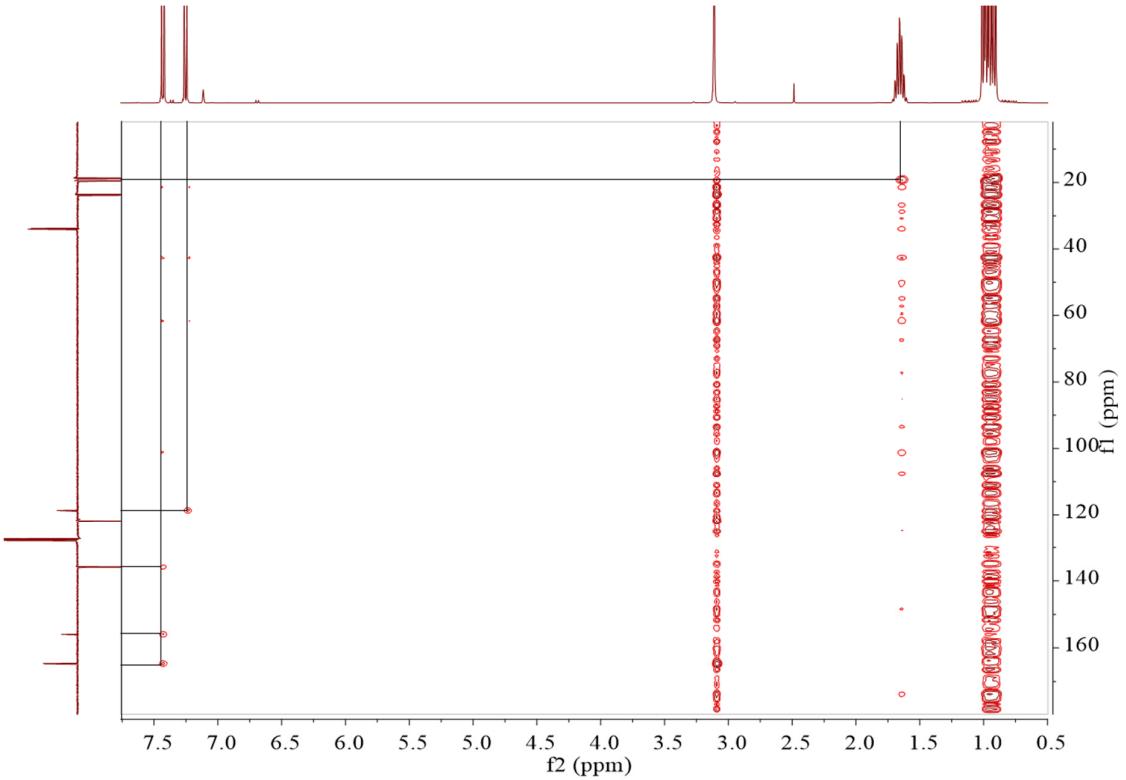

Figure S5: The ^{1}H-^{13}C HMBC NMR spectrum of the first crop of crystals of ^{iPr}**PNNP** in C_6D_6 at 298 K.

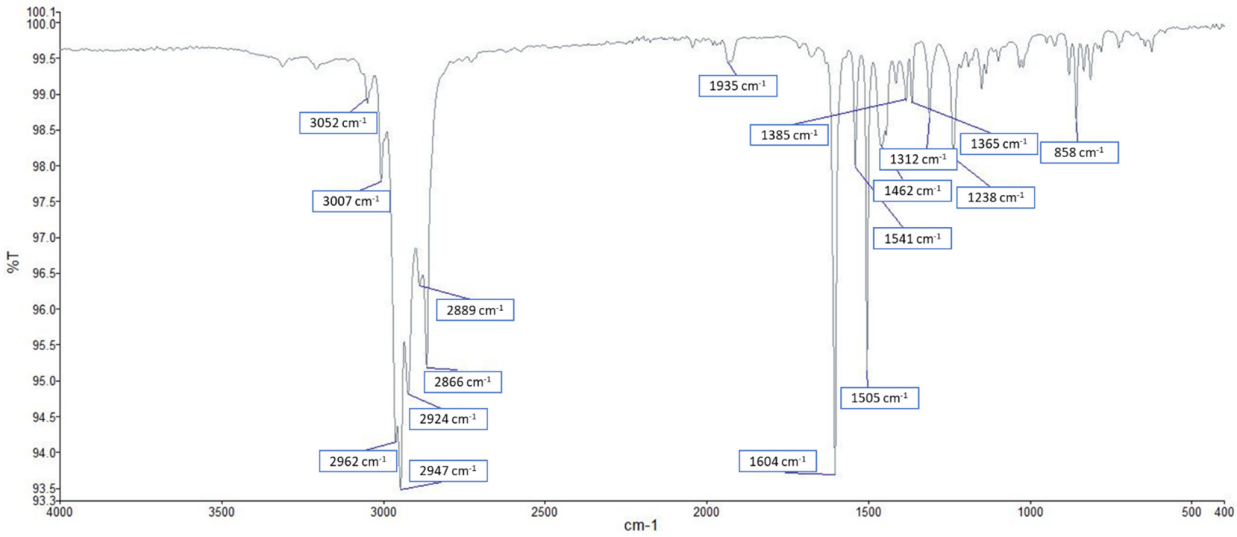

Figure S6: The ATR-IR spectrum of the first crop of crystals of ^{iPr}**PNNP** in C_6D_6 at 298 K.

Synthesis of [Fe_2(^{iPr}PNNP)$(CO)_7$] (1):

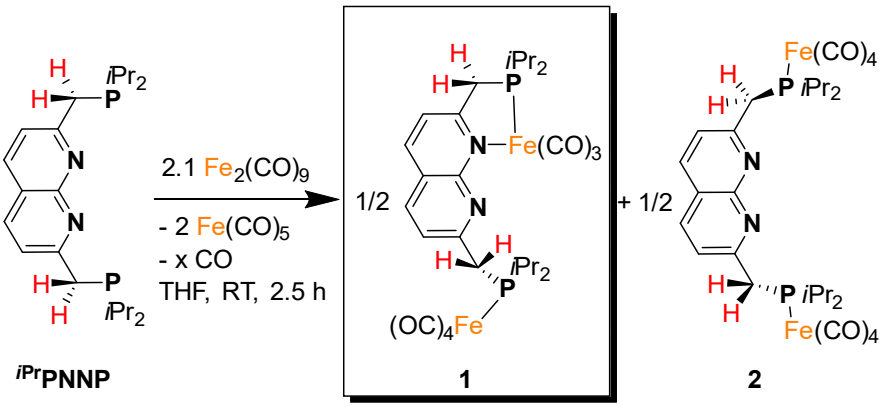

A solution of ^{iPr}**PNNP** (390.5 mg, 1.0 mmol) in THF (15 mL) was added dropwise to a stirred suspension of $Fe_2(CO)_9$ (743 mg, 2.04 mmol, 1.02 equiv) in THF (15 mL) over the course of three minutes in a Schlenk flask. The resulting dark-green mixture in the Schlenk flask was transferred from the glovebox to a Schlenk line, opened to a dynamic N_2(g) flow* and stirred for 20 h at ambient temperature. Subsequently the mixture was concentrated under a dynamic vacuum to give a dark oil. The residue was extracted with hot toluene (8 mL, 70-80 °C) and the hot mixture was filtrated over a glass frit. After cooling to ambient temperature, the dark-green mixture, which already contained a small amount of crystalline solid was stored at -40 °C for 1 week. Dark green crystals were collected by pipetting off the mother liquor and were washed with Et_2O (2 x 1.5 mL) yielding **1** as a dark green solid (180 mg, 0.26 mmol, 26%).

* Performing the reaction in a closed vessel results in an unsuccessful reaction.

^{1}H NMR (400 MHz, Benzene-d_6, 298 K): δ 7.39 (dd, $^{3}J_{H,H}$ = 8.2 Hz, $^{4}J_{H,H}$ = 1.2 Hz, 1H), 7.16 (*overlaps with C_6D_5H*, d, 1H) 7.02 (dd, $^{3}J_{H,H}$ = 8.2 Hz, $^{4}J_{H,H}$ = 1.0 Hz, 1H), 6.40 (d, $^{3}J_{H,H}$ = 8.2 Hz, 1H), 3.47 (d, $^{2}J_{H,P}$ = 10.7 Hz, 2H), 2.81 (d, $^{2}J_{H,P}$ = 9.0 Hz, 2H), 2.78 (*overlaps with doublet,* heptd, $^{2}J_{H,P}$ = 10.4 Hz, $^{3}J_{H,H}$ = 7.0 Hz, 2H), 1.96 (heptd, $^{2}J_{H,P}$ = 13.9 Hz, $^{3}J_{H,H}$ = 7.0 Hz, 2H), 1.46 (dd, $^{3}J_{H,P}$ = 14.9 Hz, $^{3}J_{H,H}$ = 6.9 Hz, 6H), 1.30 (dd, $^{3}J_{H,P}$ = 17.2 Hz, 7.2 Hz, 6H), 1.11 (dd, $^{3}J_{H,P}$ = 16.2 Hz, $^{3}J_{H,H}$ = 7.1 Hz, 6H), 0.81 (dd, $^{3}J_{H,P}$ = 13.8 Hz, $^{3}J_{H,H}$ = 6.9 Hz, 6H).

^{1}H NMR (400 MHz, THF-d_8, 298 K): δ 8.21 (d, $^{3}J_{H,H}$ = 8.0 Hz, 1H), 8.12 (d, $^{3}J_{H,H}$ = 7.8 Hz, 1H), 7.64 (d, $^{3}J_{H,H}$ = 8.1 Hz, 1H), 7.50 (d, $^{3}J_{H,H}$ = 7.8 Hz, 1H), 3.84 (d, $^{2}J_{H,P}$ = 10.8 Hz, 2H), 3.78 (d, $^{2}J_{H,P}$ = 9.3 Hz, 2H), 3.14 (heptd, $^{2}J_{H,P}$ = 10.1 Hz, $^{3}J_{H,H}$ = 7.1 Hz, 2H), 2.38 (heptd, $^{2}J_{H,P}$ = 14.0 Hz, $^{3}J_{H,H}$ = 7.1 Hz, 2H), 1.61 (dd, $^{3}J_{H,P}$ = 14.8 Hz, $^{3}J_{H,H}$ = 6.8 Hz, 6H), 1.41 (dd, $^{3}J_{H,P}$ = 17.0 Hz, $^{3}J_{H,H}$ = 7.1 Hz, 6H), 1.26 (dd, $^{3}J_{H,P}$ = 16.1 Hz, $^{3}J_{H,H}$ = 6.9 Hz, 6H), 1.09 (dd, $^{3}J_{H,P}$ = 13.6 Hz, $^{3}J_{H,H}$ = 6.8 Hz, 6H).

^{13}C{^{1}H} NMR (101 MHz, Benzene-d_6, 298 K): δ 225.8, 214.3 (d, $^{2}J_{C,P}$ = 18.1 Hz), 167.8 (d, $^{2}J_{C,P}$ = 11.2 Hz), 159.4 (d, $^{2}J_{C,P}$ = 3.8 Hz), 155.6 (t, $^{5}J_{C,P}$ = 2.1 Hz), 137.1 (d, $^{4}J_{C,P}$ = 1.5 Hz), 135.8, 125.3 (d, $^{3}J_{C,P}$ = 2.8 Hz), 120.5 (d, $^{5}J_{C,P}$ = 1.9 Hz), 119.8 (d, $^{3}J_{C,P}$ = 8.4 Hz), 39.9 (d, $^{1}J_{C,P}$ = 12.4 Hz), 36.6 (d, $^{1}J_{C,P}$ = 19.7 Hz), 28.6 (d, $^{1}J_{C,P}$ = 22.4 Hz), 25.9 (d, $^{1}J_{C,P}$ = 20.1 Hz), 19.7 (d, $^{2}J_{C,P}$ = 1.9 Hz), 18.4(d, $^{2}J_{C,P}$ = 5.0 Hz), 18.1 (d, $^{2}J_{C,P}$ = 2.2 Hz), 17.6.

^{13}C{^{1}H} NMR (101 MHz, THF-d_8, 298 K): δ 226.5, 214.9 (d, $^{2}J_{C,P}$ = 18.0 Hz), 169.9 (d, $^{2}J_{C,P}$ = 11.2 Hz), 160.0 (d, $^{2}J_{C,P}$ = 4.1 Hz), 156.4 (t, $^{4}J_{C,P}$ = 1.9 Hz), 138.7 (d, $^{4}J_{C,P}$ = 2.2 Hz) , 137.8, 126.0 (d, $^{3}J_{C,P}$ = 2.8 Hz), 122.0 (d, $^{5}J_{C,P}$ = 1.8 Hz), 121.5 (d, $^{3}J_{C,P}$ = 9.6 Hz), 40.7 (d, $^{1}J_{C,P}$ = 13.5 Hz), 37.3 (d, $^{1}J_{C,P}$ = 20.1 Hz), 29.3 (d, $^{1}J_{C,P}$ = 22.5 Hz), 26.7 (d, $^{1}J_{C,P}$ = 20.5 Hz), 20.2 (d, $^{2}J_{C,P}$ = 1.8 Hz), 18.8 (d, $^{2}J_{C,P}$ = 5.2 Hz), 18.6 (d, $^{2}J_{C,P}$ = 2.0 Hz), 18.0.

^{31}P{^{1}H} NMR (162 MHz, Benzene-d_6, 298 K): δ 93.6 (s), 86.5 (s).

^{31}P{^{1}H} NMR (162 MHz, THF-d_8, 298 K): δ 94.4 (s), 87.5 (s).

Anal. Calcd. For $C_{29}H_{36}O_7N_2P_2Fe_2 \cdot$ 0.2 THF: C, 50.22; H, 5.32; N, 3.93. Found C, 50.49; H, 5.14; N, 3.71.

Inclusion of 0.2 equiv of THF for the elemental analysis of complex **1** leads to a satisfactory elemental analysis. The THF is included here, since it is also observed in the ^{1}H NMR spectrum of complex **1**.

ATR-IR (film, N_2 flow): ν = 2962 (m), 2929 (m), 2876 (m), 2043 (s), 1963 (s), 1921 (s), 1872 (s), 1848 (s) 1599 (w), 1509 (w), 1452 (w), 624 (w) cm^{-1}.

ESI-MS: Despite several attempts, no signals corresponding to complex **1** were found, possibly due to the sensitive nature or poor ionization of the sample.

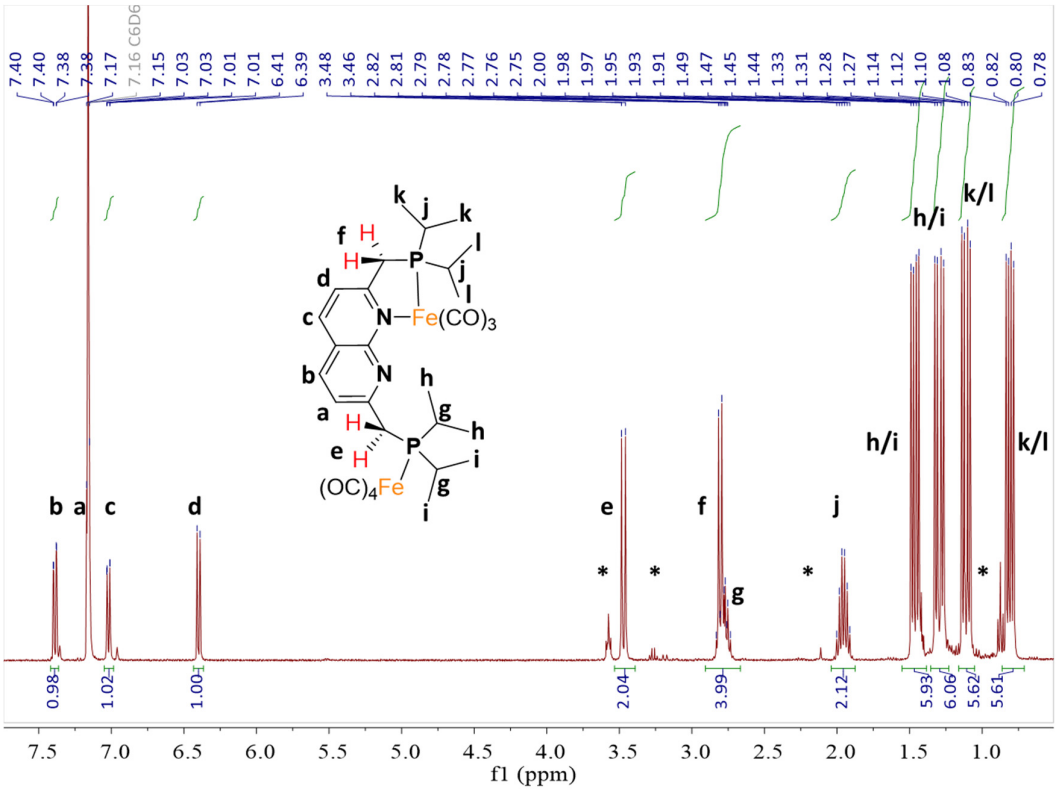

Figure S7: The ^{1}H NMR spectrum of **1** in C_6D_6 at 298 K. The resonances with the star are attributed to residual THF, Et_2O and pentane, respectively.

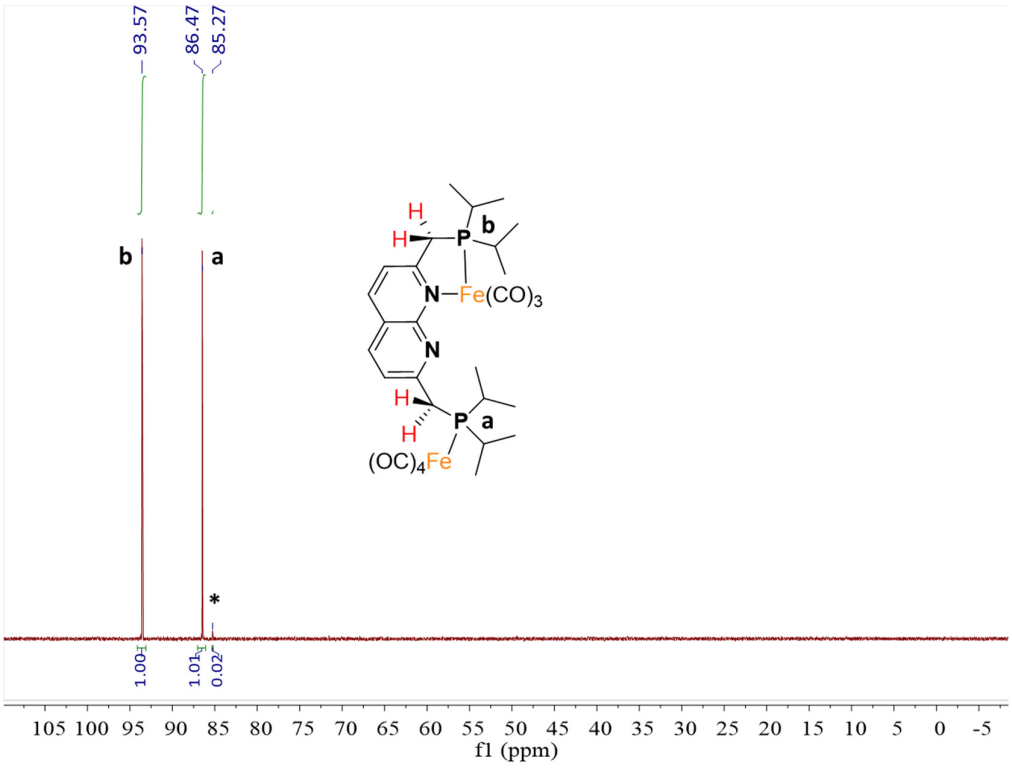

Figure S8: The $^{31}P\{^{1}H\}$ NMR spectrum of **1** in C_6D_6 at 298 K. The resonance with the star is attributed to the impurity complex **2**.

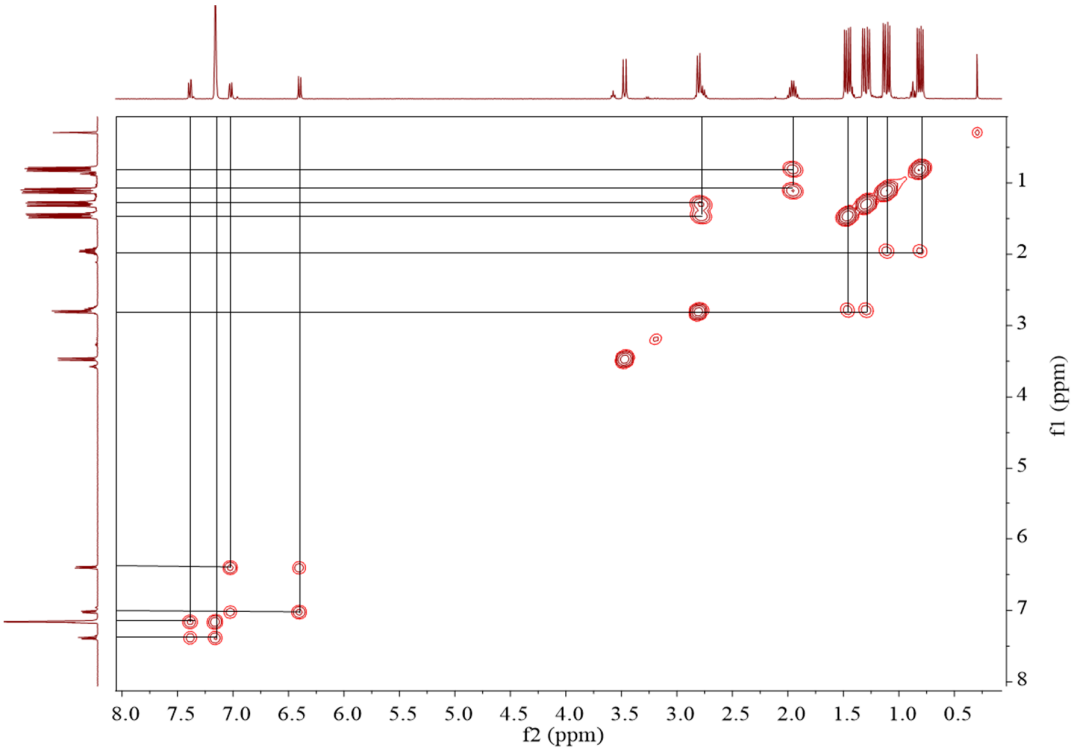

Figure S9: The ^{1}H-^{1}H COSY NMR spectrum of **1** in C_6D_6 at 298 K.

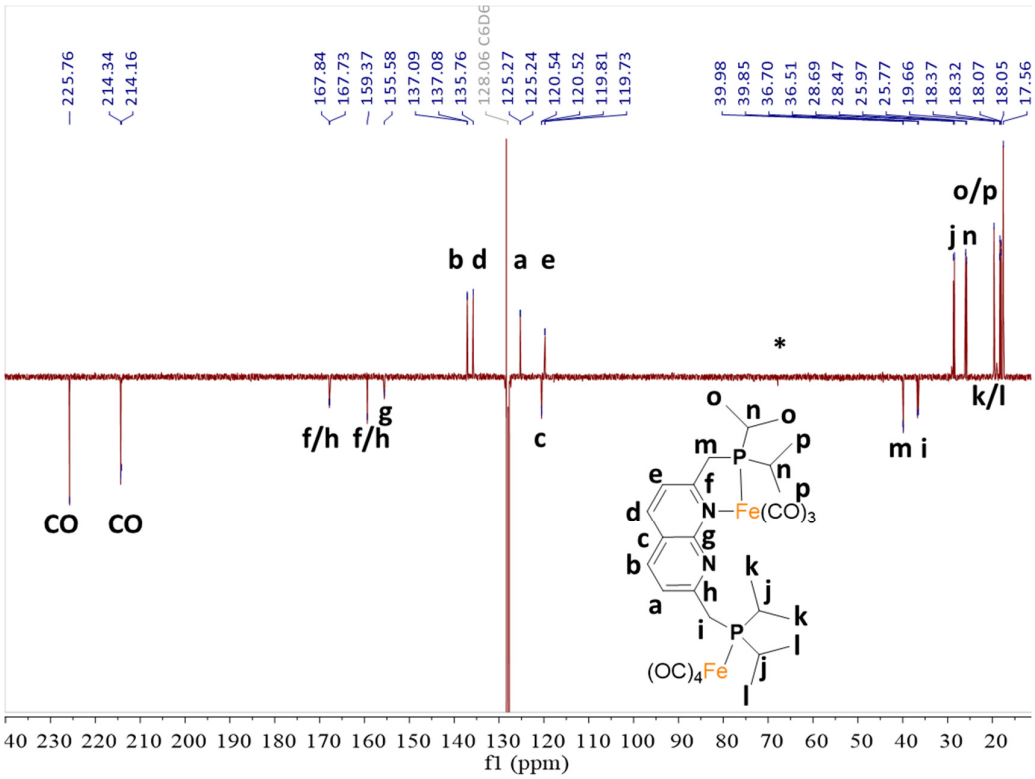

Figure S10: The ^{13}C-APT NMR spectrum of **1** in C_6D_6 at 298 K. The resonance with the star is attributed to residual THF.

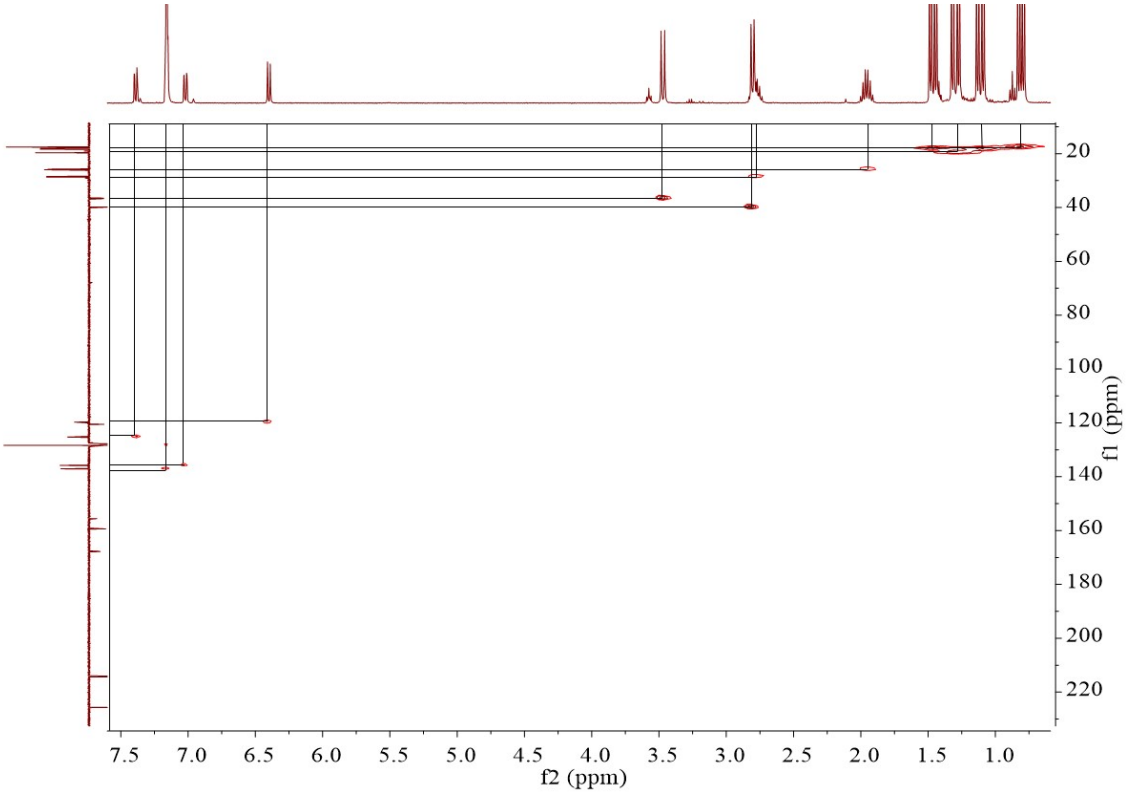

Figure S11: The ^{1}H-^{13}C HMQC NMR spectrum of **1** in C_6D_6 at 298 K.

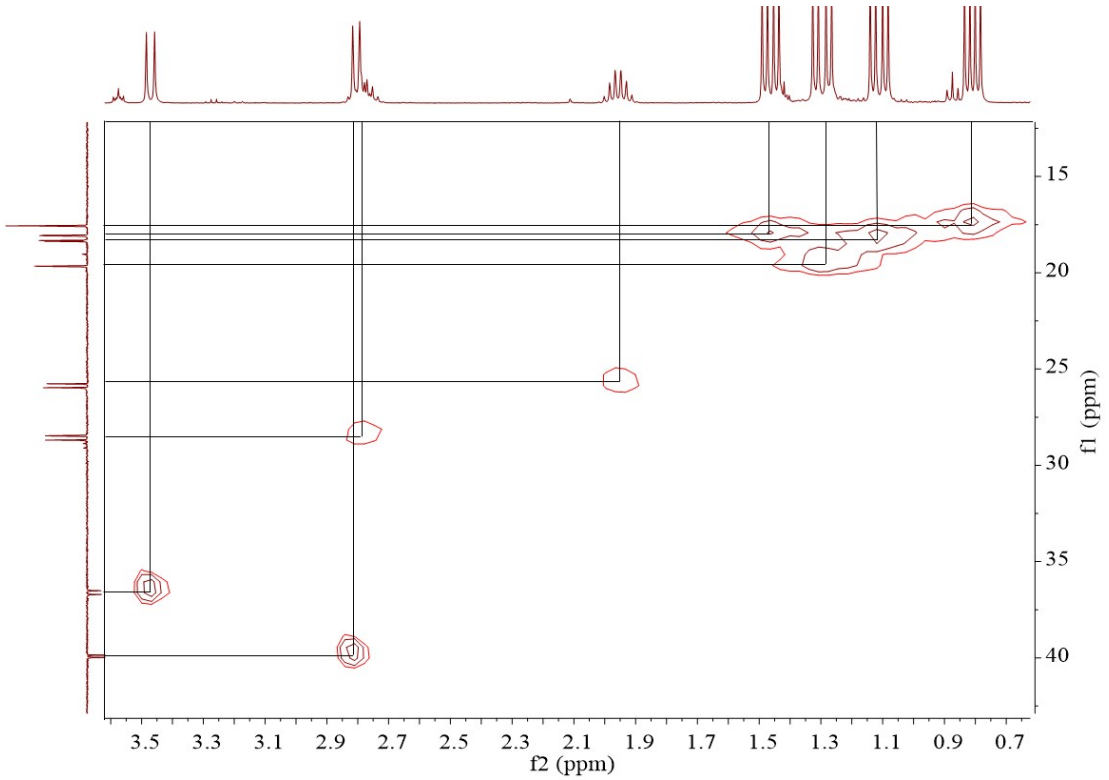

Figure S12: The zoom in of the aliphatic region of the ^{1}H-^{13}C HMQC NMR spectrum of **1** in C_6D_6 at 298 K.

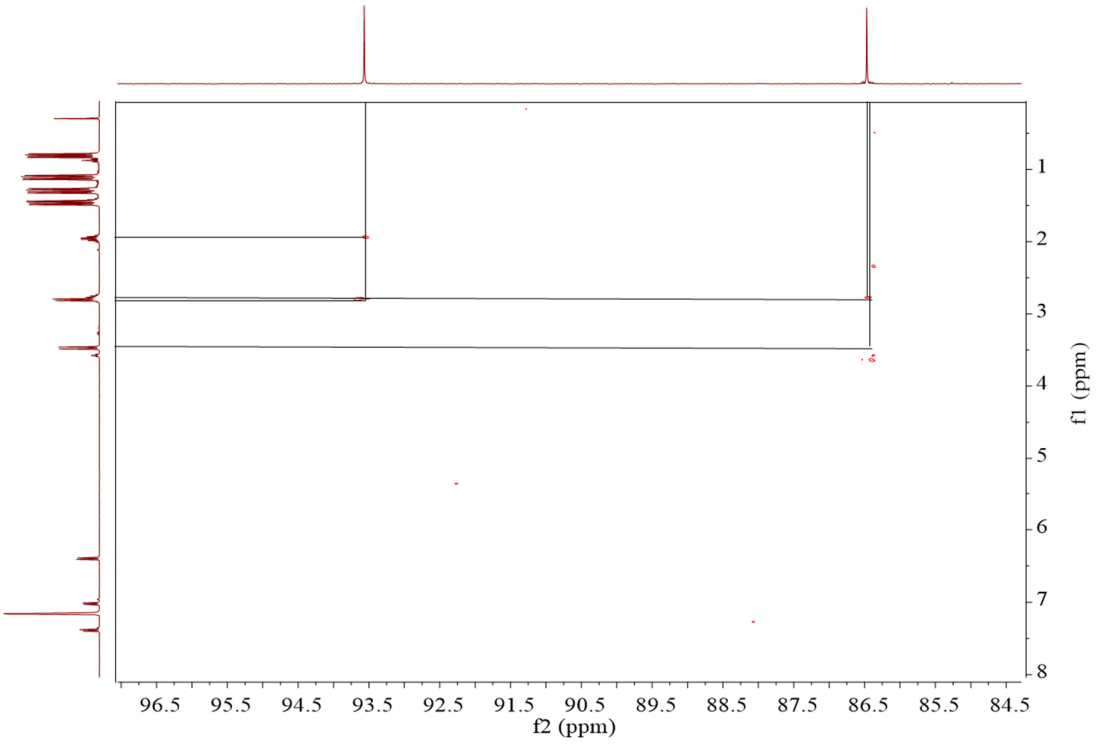

Figure S13: The ^{31}P-^{1}H HMBC NMR spectrum of **1** in C_6D_6.

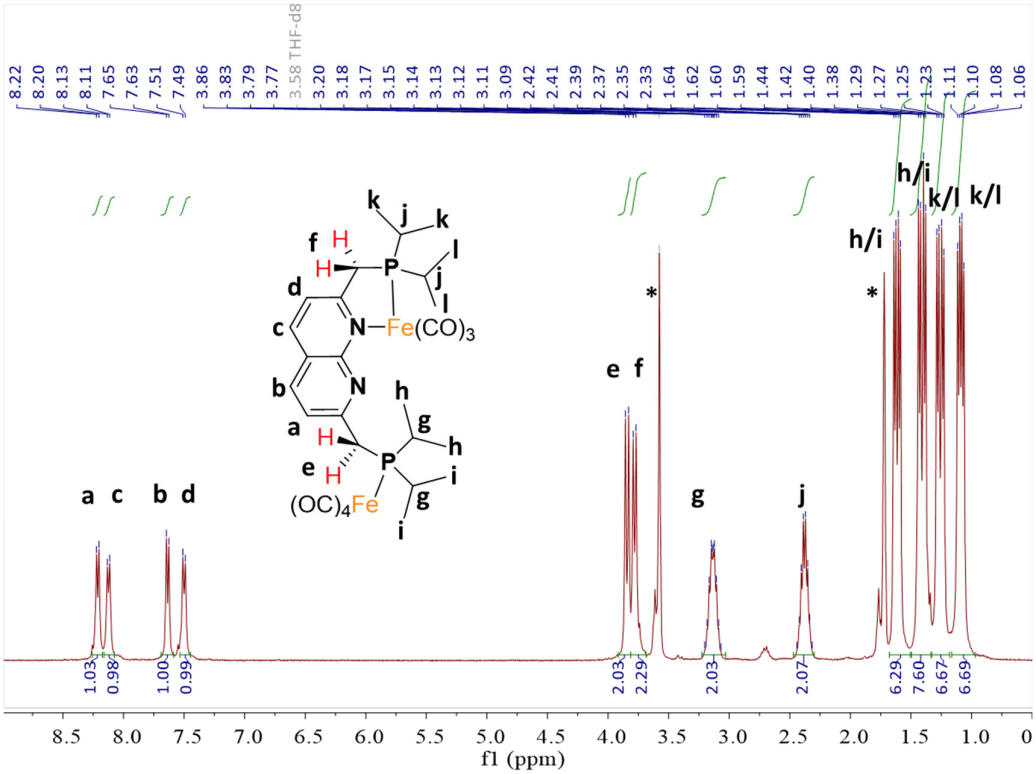

Figure S14: The ^{1}H NMR spectrum of **1** in THF-d_8 at 298 K. The resonances with the star are attributed to THF-d_7. Other bumps in the baseline are attributed to the impurity complex **2**.

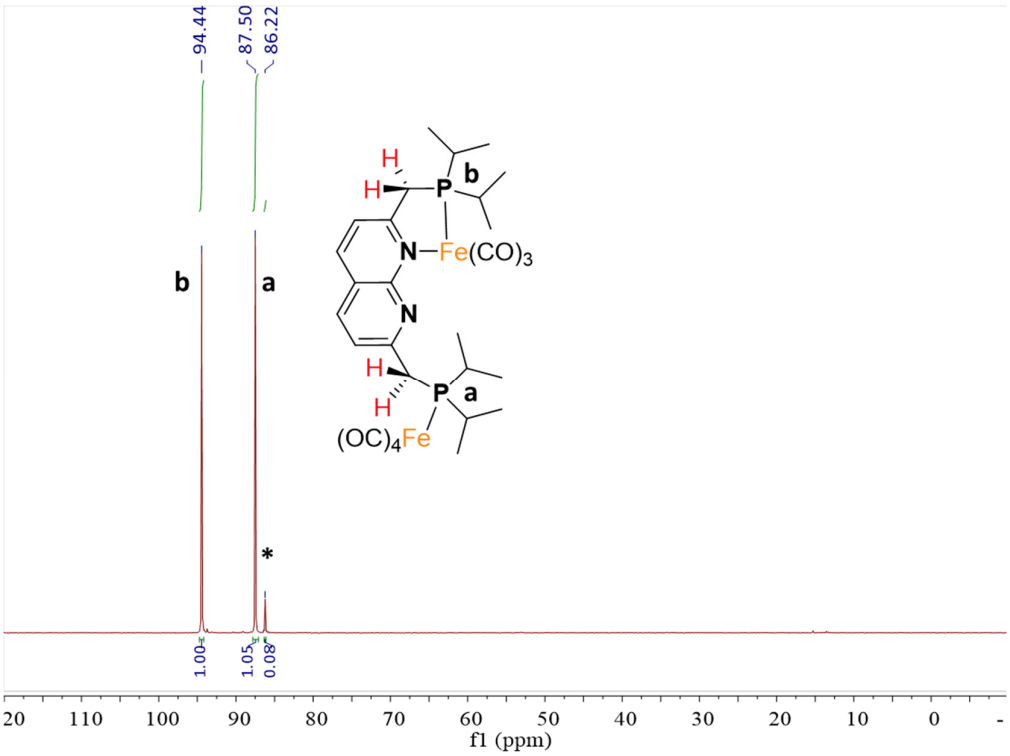

Figure S15: The $^{31}P\{^{1}H\}$ NMR spectrum of **1** in THF-d_8 at 298 K. The resonance with the star is attributed to complex **2**.

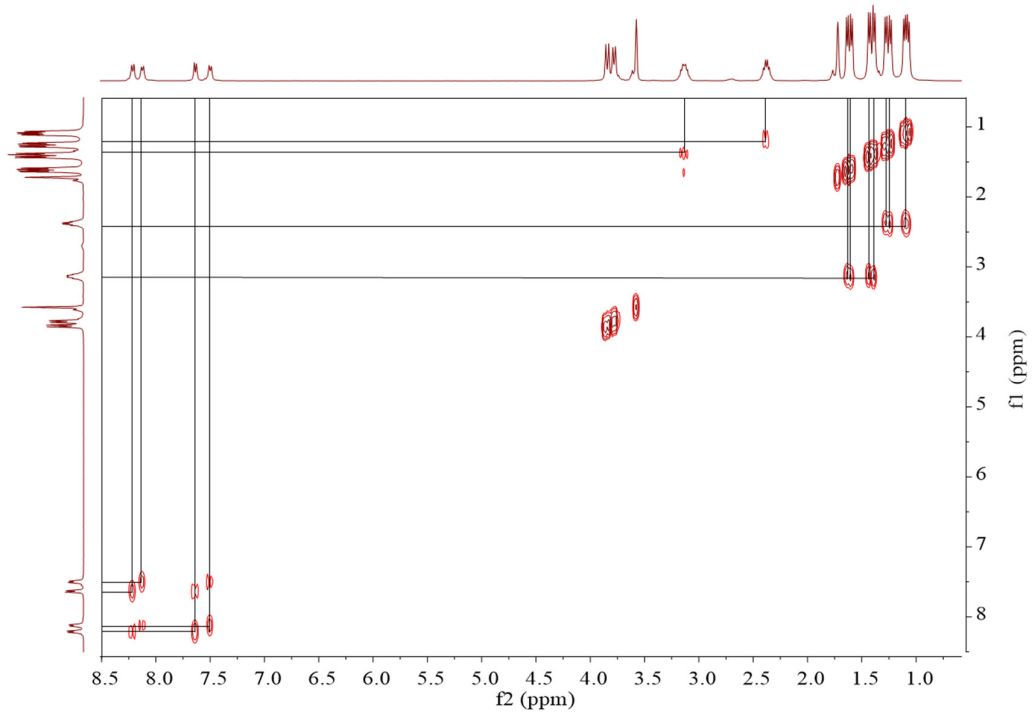

Figure S16: The ^{1}H-^{1}H COSY NMR spectrum of **1** in THF-d_8 at 298 K.

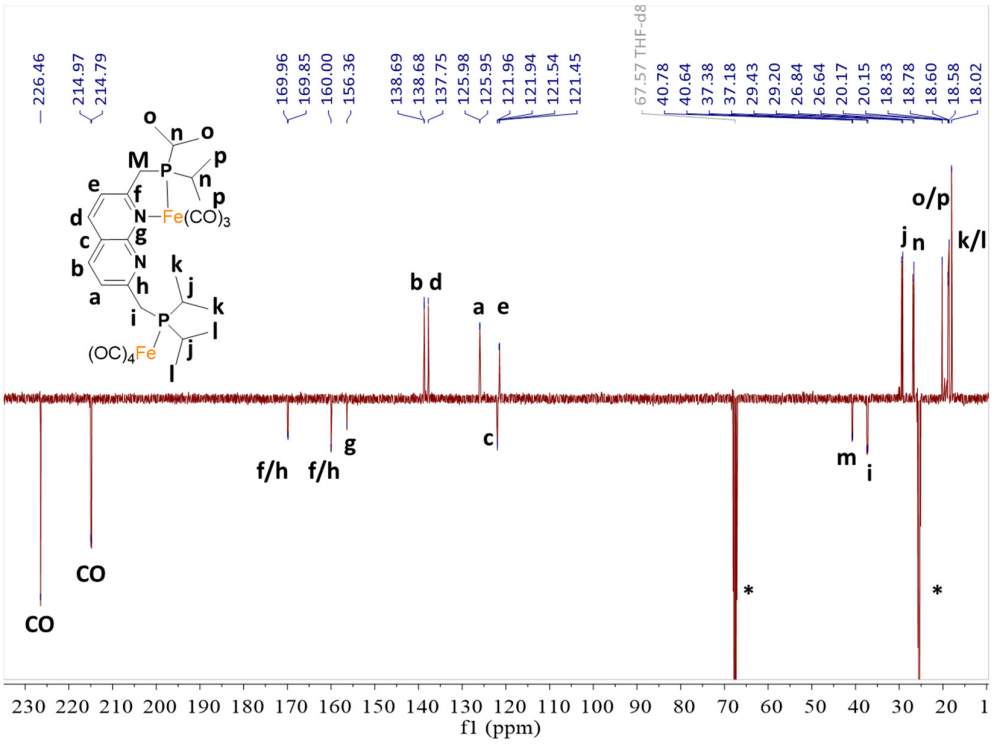

Figure S17: The ^{13}C-APT NMR spectrum of **1** in THF-d_8 at 298 K. The resonances with the star are attributed to THF-d_8.

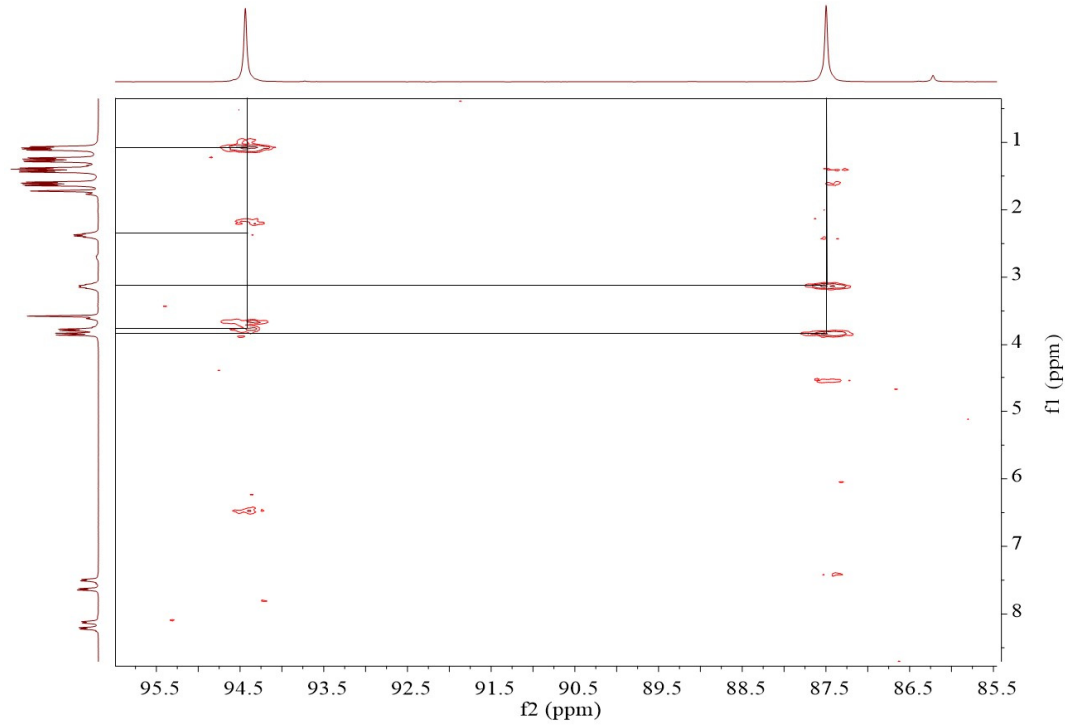

Figure S18: The ^{31}P-^{1}H HMBC NMR spectrum of **1** in THF-d_8 at 298 K.

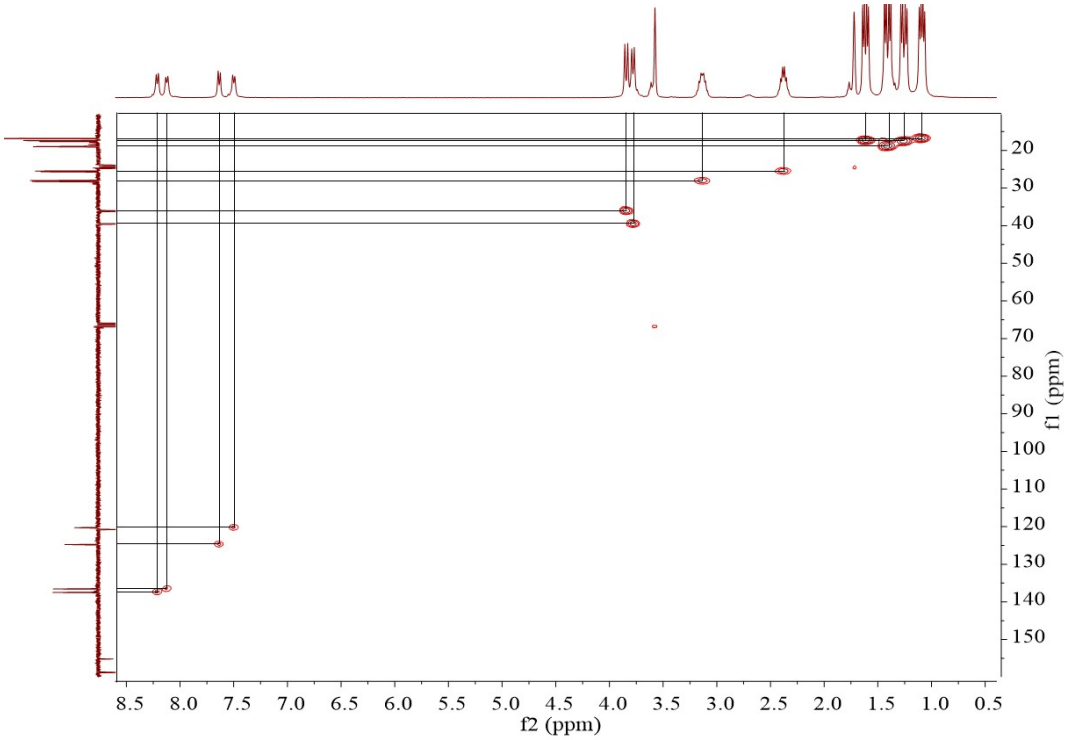

Figure S19: The ^{1}H-^{13}C HMQC NMR spectrum of **1** in THF-d_8 at 298 K.

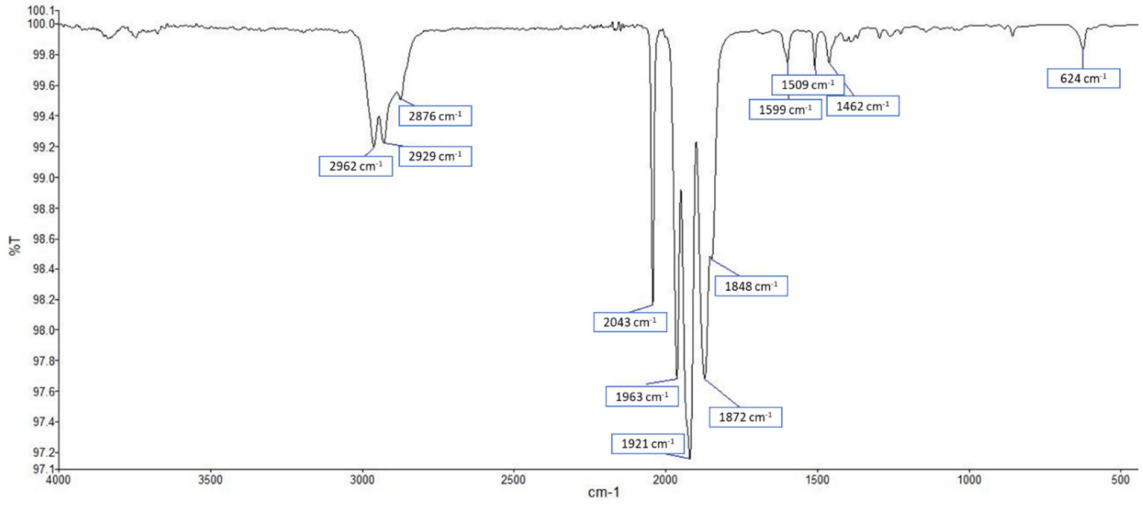

Figure S20: The ATR-IR spectrum of complex **1** (film).

Synthesis of $[Fe_2(^{iPr}PNNP)(CO)_7]$ (1) and $[Fe_2(^{iPr}PNNP)(CO)_8]$ (2):

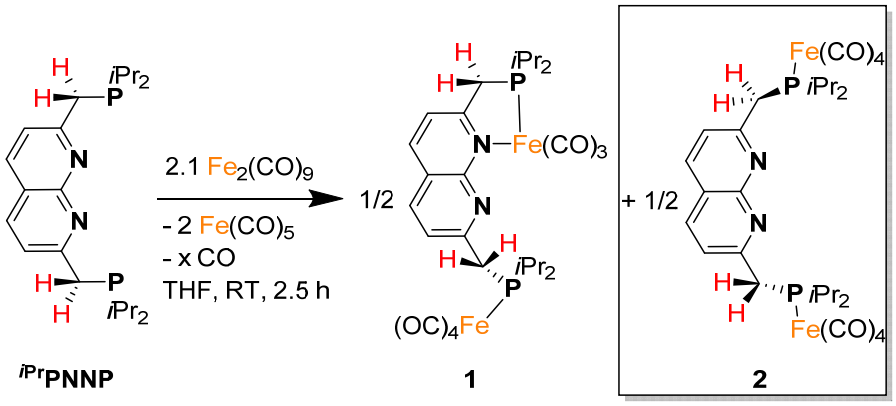

A solution of **^{iPr}PNNP** (195.2 mg, 0.50 mmol) in THF (7.0 mL) was added dropwise to a stirred suspension of $Fe_2(CO)_9$ (390 mg, 1.05 mmol, 2.1 equiv) in THF (8.0 mL) over the course of four minutes in a Schlenk flask. The resulting dark-green mixture in the Schlenk flask was transferred from the glovebox to a Schlenk line, opened to dynamic N_2(g) flow***** and was stirred for 17 h at ambient temperature, after which it was concentrated under a dynamic vacuum to give a dark solid. The residue was washed with pentane (2 x 10 mL) and Et_2O (2 x 18 mL) and then extracted with THF (15 mL). The dark green extract was concentrated under a dynamic vacuum to give **1** as a dark green solid (104 mg, 0.15 mmol, 30%). The remaining Et_2O fraction contains both compounds **1** and **2** which after evaporation gives a yellow to green powder (240 mg, containing about 15% **1** according to ^{31}P NMR spectroscopy). The purity of **2** can be improved by storing a concentrated Et_2O solution of a mixture of **1** and **2** in the freezer overnight at -40 °C to yield large yellow crystals of **2** (covered by small green crystals of **1**) which can be handpicked from the mixture.

***** Performing the reaction in a closed vessel results in an unsuccessful reaction.

^{1}H NMR (400 MHz, Benzene-d_6, 298 K): δ 7.40 (d, $^3J_{H,H}$ = 8.2 Hz, 2H), 7.22 (d, $^3J_{H,H}$ = 8.4 Hz, 2H), 3.19 (d, $^2J_{H,P}$ = 10.2 Hz, 4H), 2.38 – 2.10 (m, *two overlapping heptd*, 4H), 1.15 (dd, $^3J_{H,P}$ = 15.2 Hz, $^3J_{H,H}$ = 7.0 Hz, 12H), 1.05 (dd, $^3J_{H,P}$ = 16.3 Hz, $^3J_{H,H}$ = 7.2 Hz, 12H).

^{13}C NMR (101 MHz, Benzene-d_6, 298 K): δ 214.3 (d, $^2J_{C,P}$ = 18.0 Hz), 159.6 (d, $^2J_{C,P}$ = 4.5 Hz), 155.5 (t, $^{4/5}J_{C,P}$ = 1.8 Hz), 137.2, 124.2 (d, $^3J_{C,P}$ = 2.5 Hz), 120.1 (t, $^{4/5}J_{C,P}$ = 1.7 Hz), 37.0 (d, $^1J_{C,P}$ = 19.1 Hz), 29.0 (d, $^1J_{C,P}$ = 23.0 Hz), 18.7 (d, $^2J_{C,P}$ = 69.9 Hz).

^{31}P NMR (162 MHz, Benzene-d_6, 298 K): δ 85.3 (s).

ATR-IR (film, N_2 flow): ν = 2966 (w), 2935 (w), 2877 (w), 2043 (s), 1964 (s), 1916 (s), 1876 (m), 1858 (m) 1605 (m), 1505 (w), 1463 (w), 1261 (w), 856 (w), 624 (w) cm^{-1}.

ESI-MS: Complex **2** $Fe_2(^{iPr}PNNP)(CO)_8$: Mass calculated for $C_{30}H_{36}O_8Fe_2N_2P_2$: 726.1. Found: $[M]^+$ at 726.0 *m/z*.

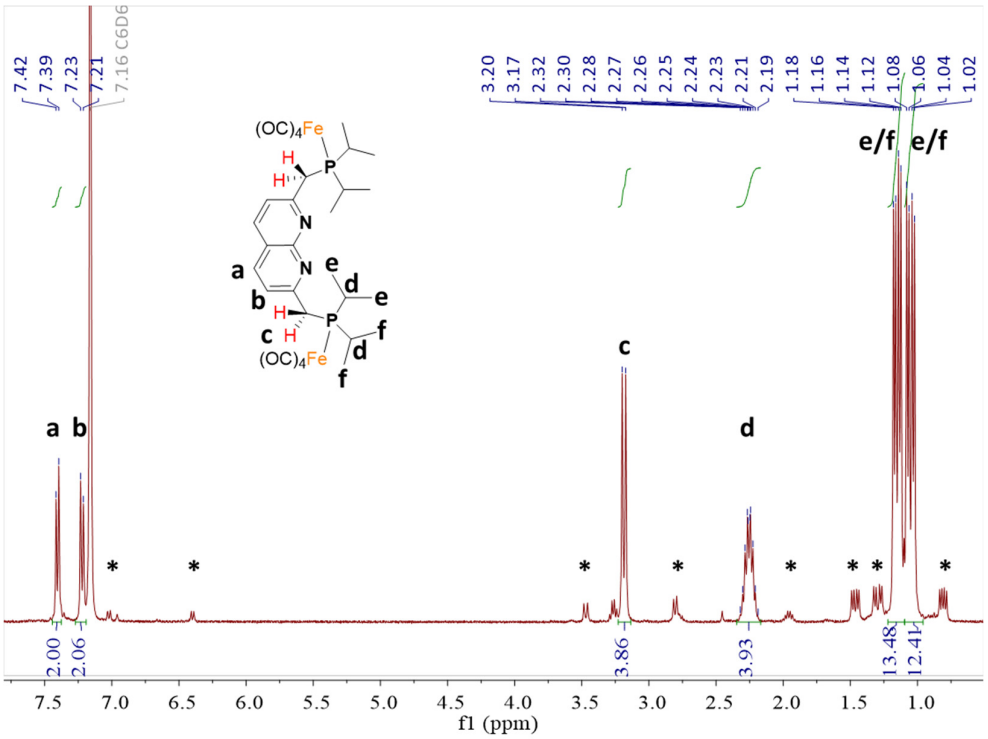

Figure S21: The ^{1}H NMR spectrum of **2** in C_6D_6 at 298 K. The resonances with the star are attributed to the impurity complex **1**.

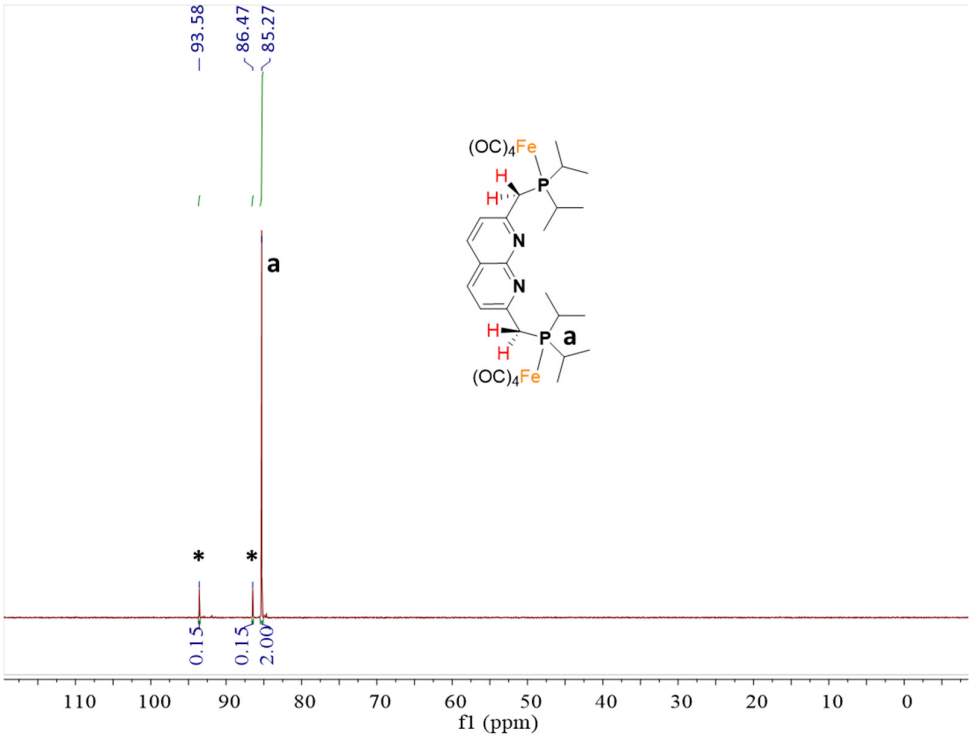

Figure S22: The $^{31}P\{^{1}H\}$ NMR spectrum of **2** in C_6D_6 at 298 K. The resonances with the star are attributed to the impurity complex **1**.

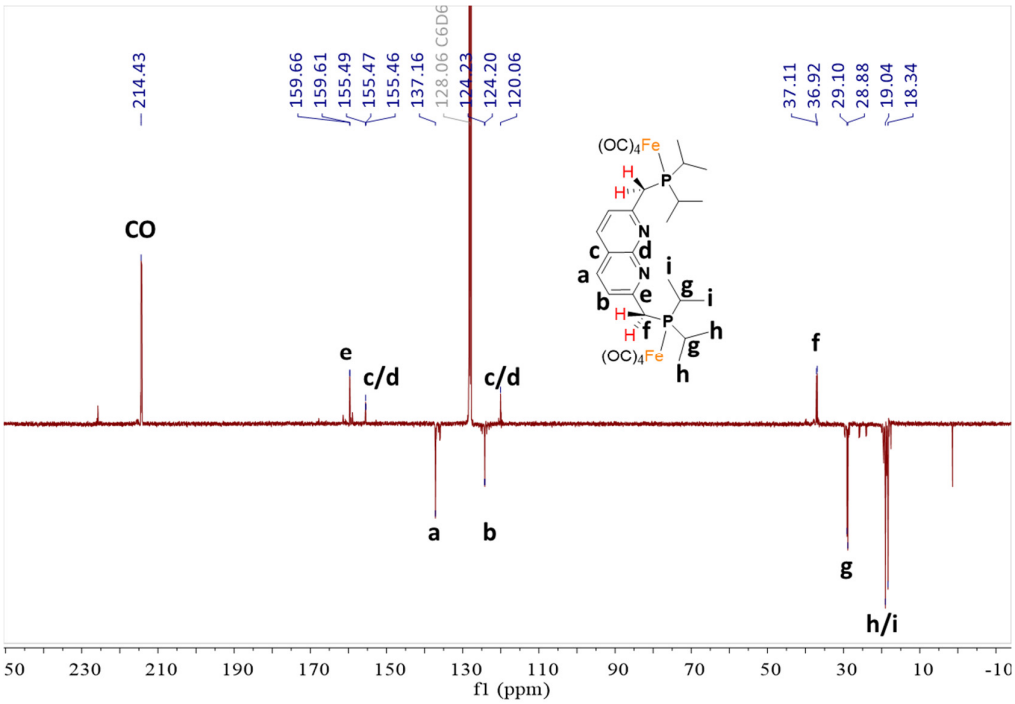

Figure S23: The $^{13}C\{^{1}H\}$ NMR spectrum of **2** in C_6D_6 at 298 K. The resonance with the star is attributed to C_6D_6. Other peaks are assigned to the impurity complex **1**.

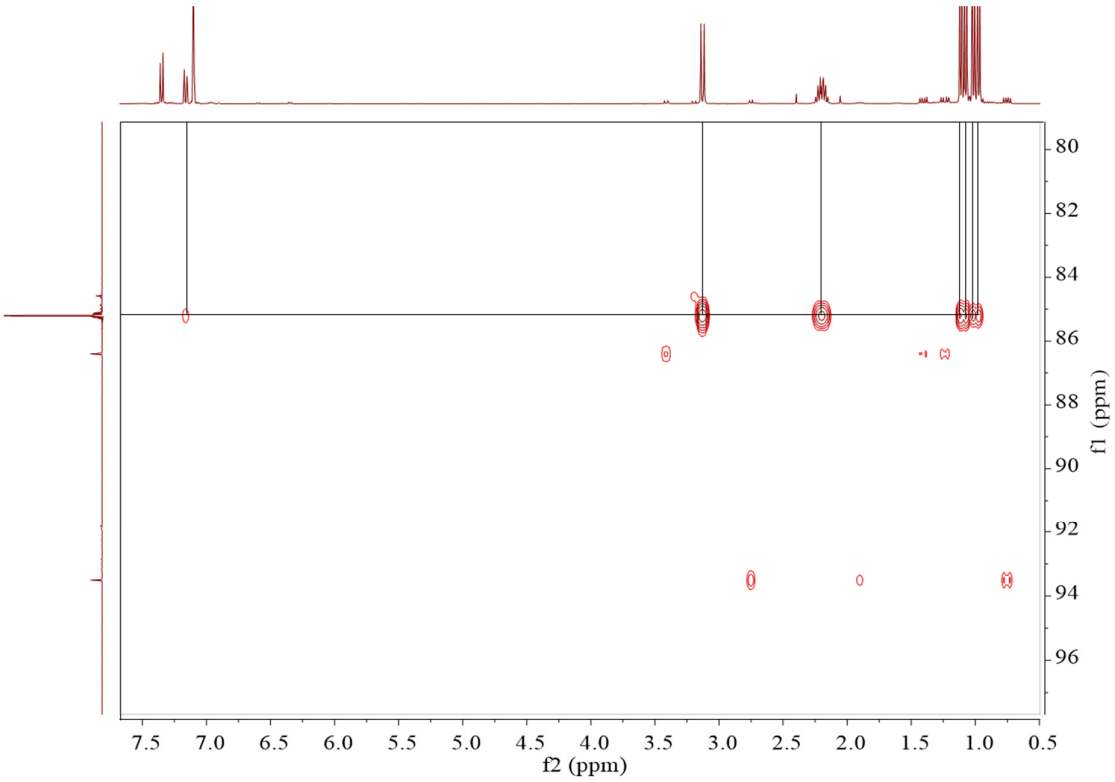

Figure S24: The ^{1}H-^{31}P HMBC NMR spectrum of **2** in C_6D_6 at 298 K. The resonances above 86 ppm in the $^{31}P\{^{1}H\}$ NMR spectrum are attributed to complex **1**.

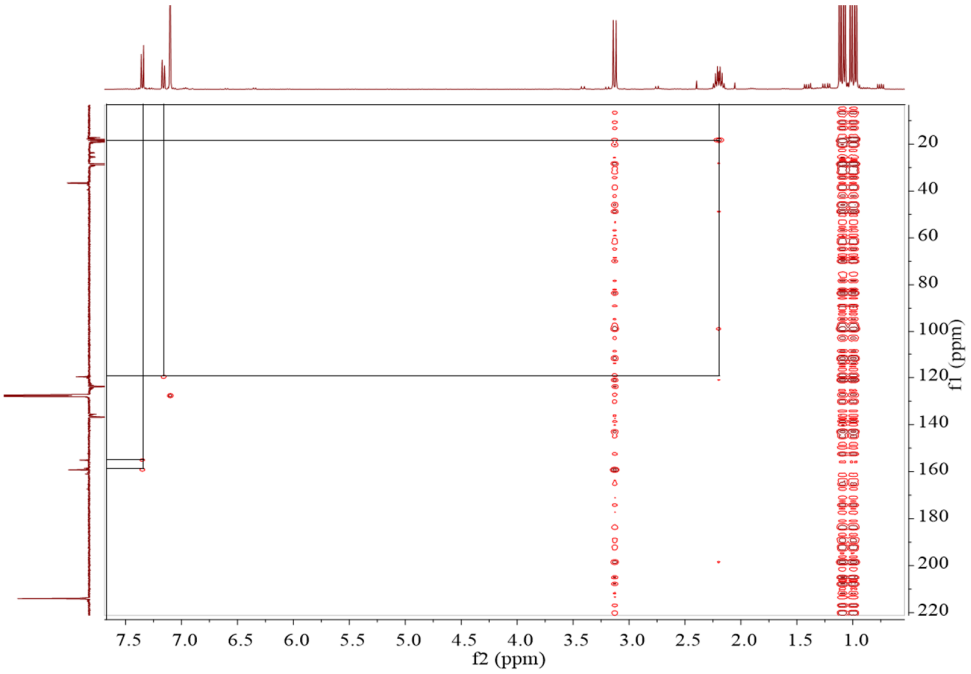

Figure S25: The ^{1}H-^{13}C HMBC NMR spectrum of **2** in C_6D_6 at 298 K.

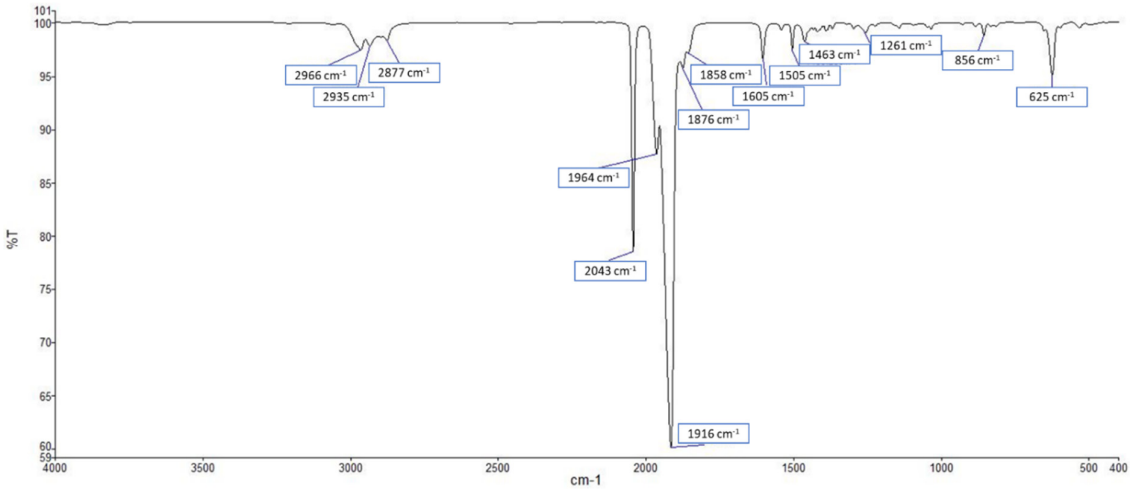

Figure S26: The ATR-IR spectrum of complex **2** (film).

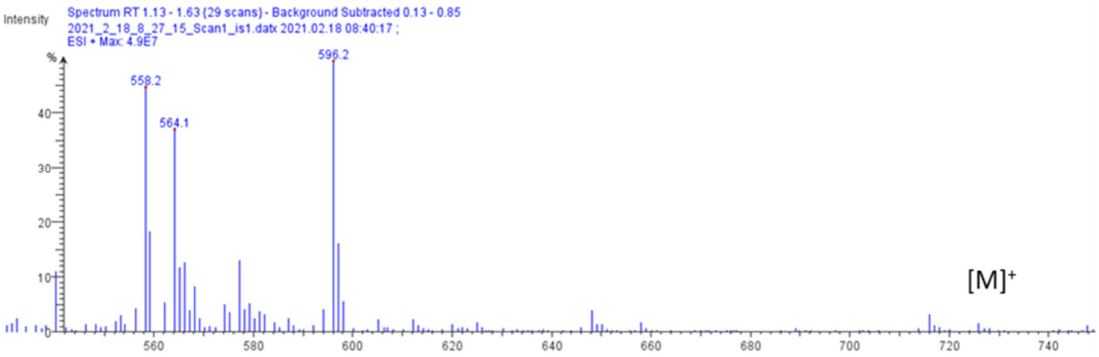

Figure S27: The ESI-MS spectrum of complex **2.** $[M]^+$ is placed above the signals corresponding to $[M]^+$.

Synthesis of K(THF)[^{iPr}PNNP*Fe(CO)$_3$Fe(CO)$_4$] (3):

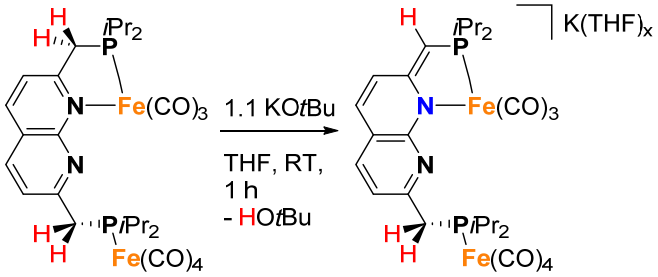

1 **3**

A solution of KO*t*Bu (17.9 mg, 156 µmol, 1.1 equiv) in THF (2 mL) was added dropwise to a stirred dark green solution of complex **1** (101.3 mg, 145 µmol) in THF (3 mL). The resulting red solution was stirred for 1 h, after which it was concentrated under a dynamic vacuum to give a dark red film, which upon scratching with a metal spatula yielded a fine powder. The solids were stirred up with benzene (3 mL) for 16 hours and then filtered off. The residue was washed with benzene (1 mL) and subsequently extracted with THF (4 mL). The extract was concentrated under a dynamic vacuum to give a dark red film, which was scratched into a powder and further dried under a dynamic vacuum, yielding **3** as a dark red-brown powder (85.7 mg, 97.4 µmol, 67%).

^{1}H NMR (400 MHz, THF-d_8, 298 K): δ 6.83 (d, $^3J_{H,H}$ = 7.2 Hz, 1H), 6.38 (dd, $^3J_{H,H}$ = 8.9 Hz, $^3J_{H,P}$ = 2.3 Hz, 1H), 6.31 (d, $^3J_{H,H}$ = 8.9 Hz, 1H), 6.25 (dd, $^3J_{H,H}$ = 7.3, $^3J_{H,P}$ = 1.5 Hz, 1H), 4.01 (d, $^2J_{H,P}$ = 3.2 Hz, 1H), 3.50 (heptd, $^2J_{H,P}$ = 13.9 Hz, $^3J_{H,H}$ = 7.0 Hz, 2H), 3.40 (d, $^2J_{H,P}$ = 8.9 Hz, 2H), 2.04 (heptd, $^2J_{H,P}$ = 13.9 Hz, $^3J_{H,H}$ = 6.9 Hz, 2H), 1.39 (dd, $^3J_{H,P}$ = 10.0 Hz, $^3J_{H,H}$ = 6.9 Hz, 6H), 1.35 (dd, $^3J_{H,P}$ = 10.2 Hz, $^3J_{H,H}$ = 4.9 Hz, 6H), 1.15 (dd, $^3J_{H,P}$ = 15.2 Hz, $^3J_{H,H}$ = 6.9 Hz, 6H), 1.09 (dd, $^3J_{H,P}$ = 13.1 Hz, $^3J_{H,H}$ = 6.9 Hz, 6H).

^{31}P{^{1}H} NMR (162 MHz, THF-d_8, 298 K): δ 82.6 (s), 82.4 (s).

^{13}C{^{1}H} NMR (101 MHz, THF-d_8, 298 K): δ 231.6 (d, $^2J_{C,P}$ = 1.8 Hz), 216.1 (d, $^2J_{C,P}$ = 17.7 Hz), 170.1 (d, $^2J_{C,P}$ = 27.7 Hz), 162.0 (t, $^2J_{C,P}$ = 2.0 Hz), 154.0 (d, $^4J_{C,P}$ = 9.0 Hz), 133.2 (d, $^4J_{C,P}$ = 1.7 Hz), 128.1 (t, $^3J_{C,P}$ = 1.6 Hz), 122.1 (dd, $^4J_{C,P}$ = 17.9 Hz, $^6J_{C,P}$ = 1.1 Hz), 118.0 (d, $^5J_{C,P}$ = 2.5 Hz), 112.3 (d, $^3J_{C,P}$ = 5.0 Hz), 80.9 (d, $^1J_{C,P}$ = 34.3 Hz), 40.0 (d, $^1J_{C,P}$ = 21.7 Hz), 29.4 (d, $^1J_{C,P}$ = 24.0 Hz), 27.7 (d, $^1J_{C,P}$ = 23.5 Hz), 20.8, 20.4 (d, $^2J_{C,P}$ = 7.3 Hz), 19.2 (d, $^2J_{C,P}$ = 25.9 Hz).

* Despite several attempts, we were unable to obtain satisfactory elemental analysis of a spectroscopically clean sample of complex **3**.

ATR-IR (film, N_2 flow): ν = 2957 (m), 2930 (w), 2870 (w), 2041 (s), 1930 (s), 1855 (s), 1815 (s), 1773 (s), 1618 (m), 1585 (m), 1533 (m), 1511 (m), 1459 (w), 1395 (m), 1381 (m), 1317 (m), 1262 (w), 1139 (m), 632 (s) cm^{-1}.

ESI-MS: Despite several attempts, no signals corresponding to complex **3** were found, possibly due to the sensitive nature or poor ionization of the sample.

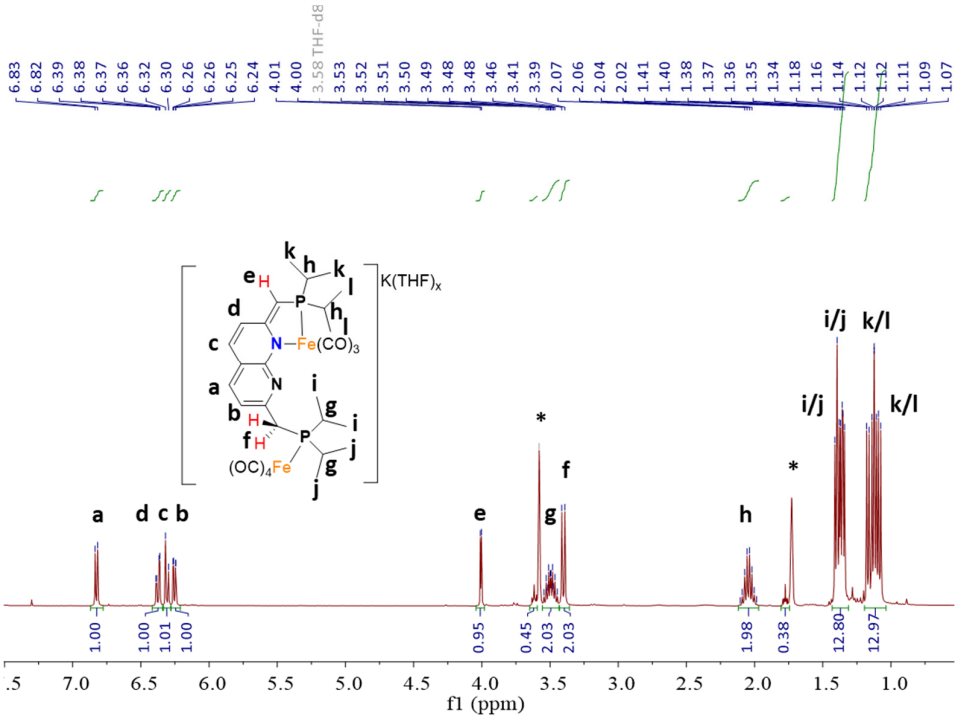

Figure S28: The ^{1}H NMR spectrum of **3** in THF-d_8 at 298 K. The resonances with the star are assigned to THF-d_7, and the bumps in the baseline are attributed to complex **1** and **2**, respectively.

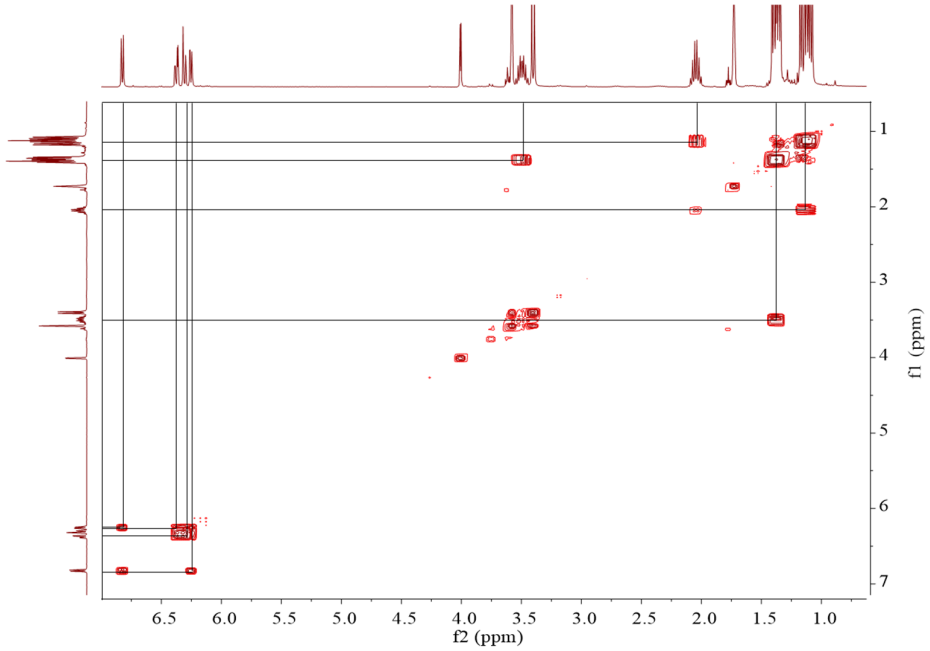

Figure S29: The ^{1}H-^{1}H COSY NMR spectrum of **3** in THF-d_8 at 298 K.

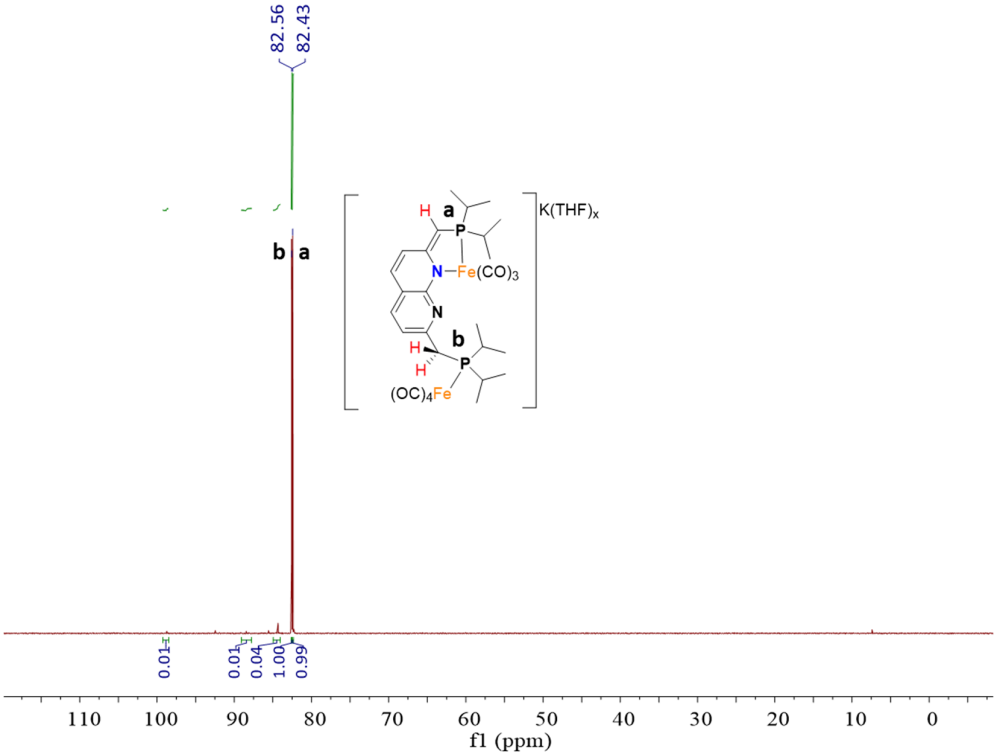

Figure S30: The $^{31}P\{^{1}H\}$ NMR spectrum of **3** in THF-d_8 at 298 K. The minor impurities are attributed to **1** and **2**, respectively.

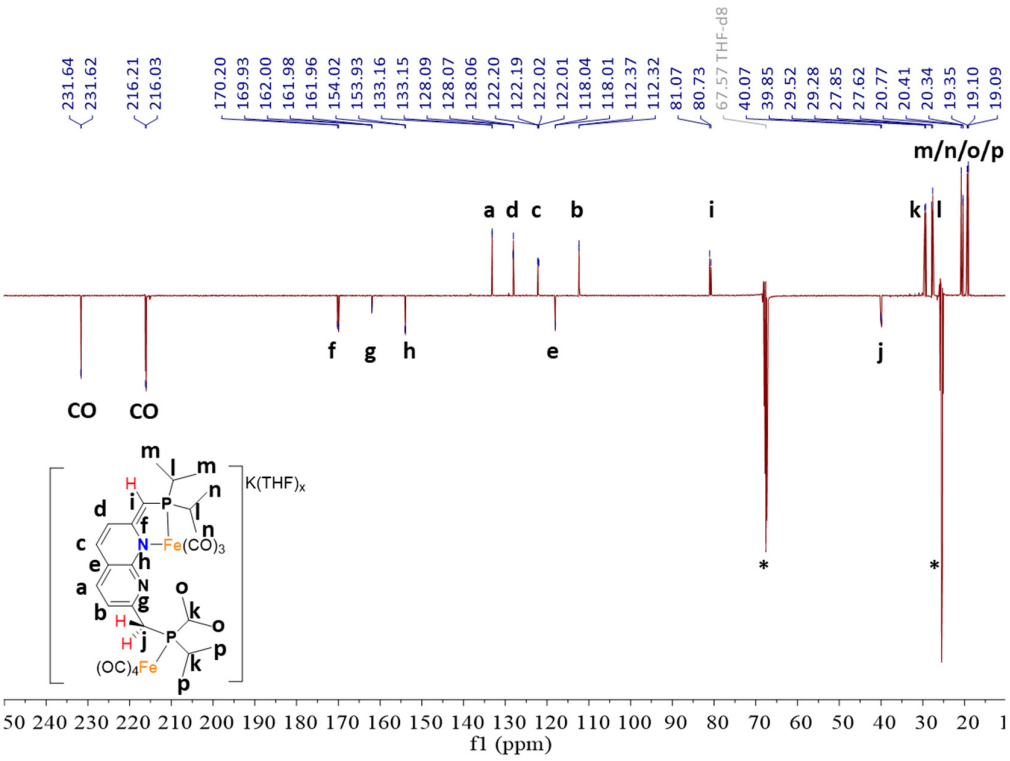

Figure S31: The ^{13}C-APT NMR spectrum of **3** in THF-d_8 at 298 K. The resonances with the star are assigned to THF-d_8.

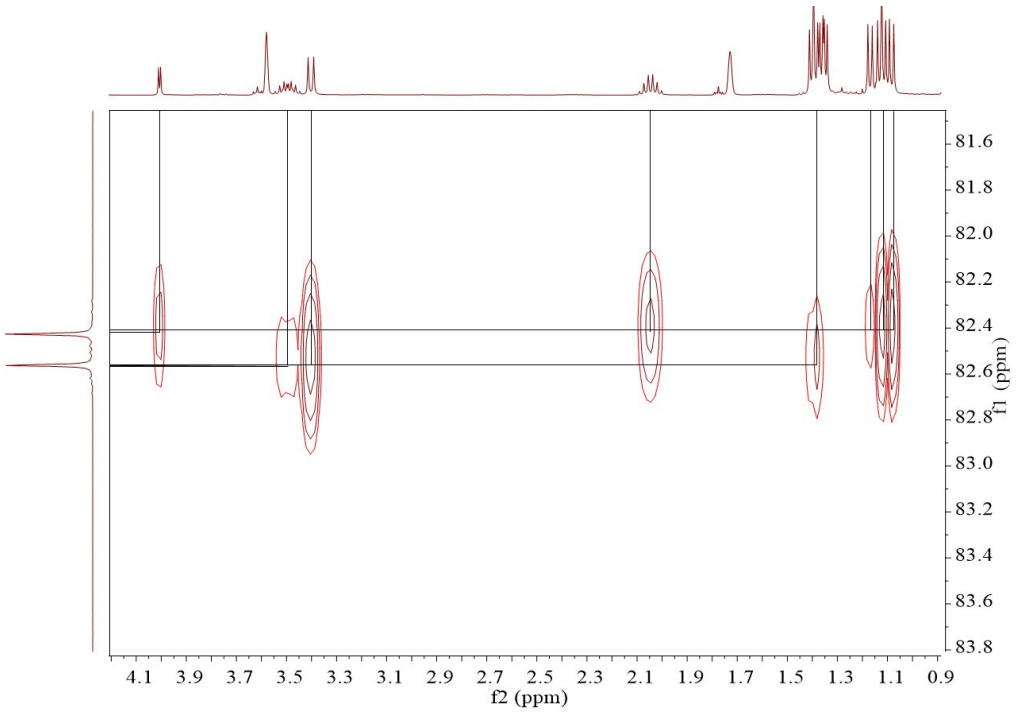

Figure S32: The ^{1}H-^{31}P HMBC NMR spectrum of **3** in THF-d_8 at 298 K.

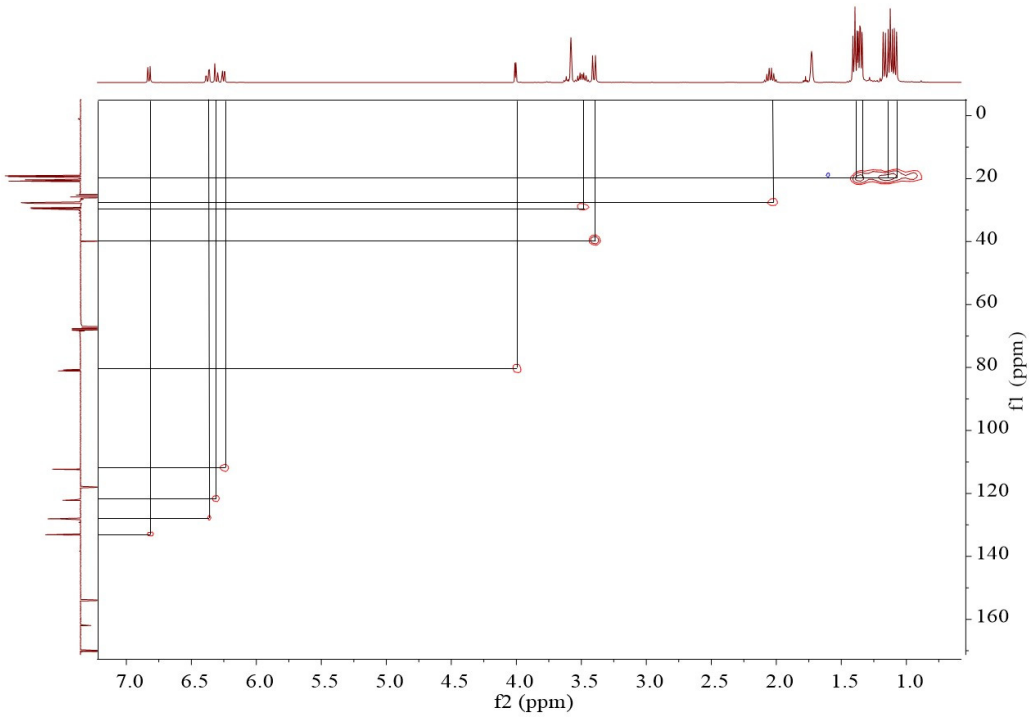

Figure S33: The ^{1}H-^{13}C HMQC NMR spectrum of **3** in THF-d_8 at 298 K.

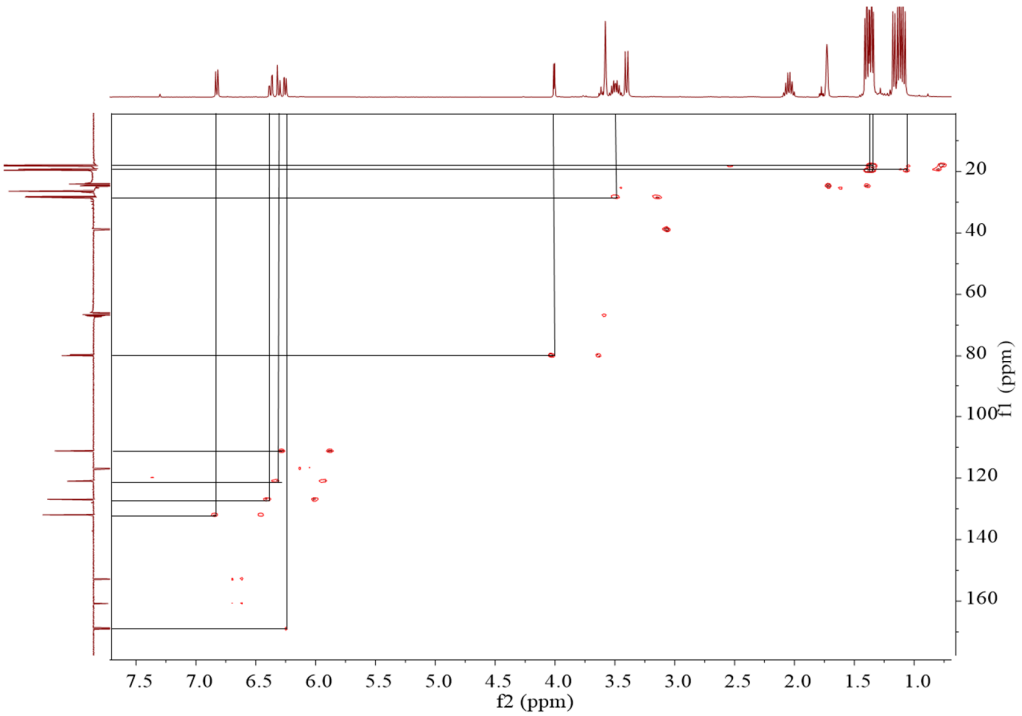

Figure S34: The ^{1}H-^{13}C HMBC NMR spectrum of **3** in THF-d_8.

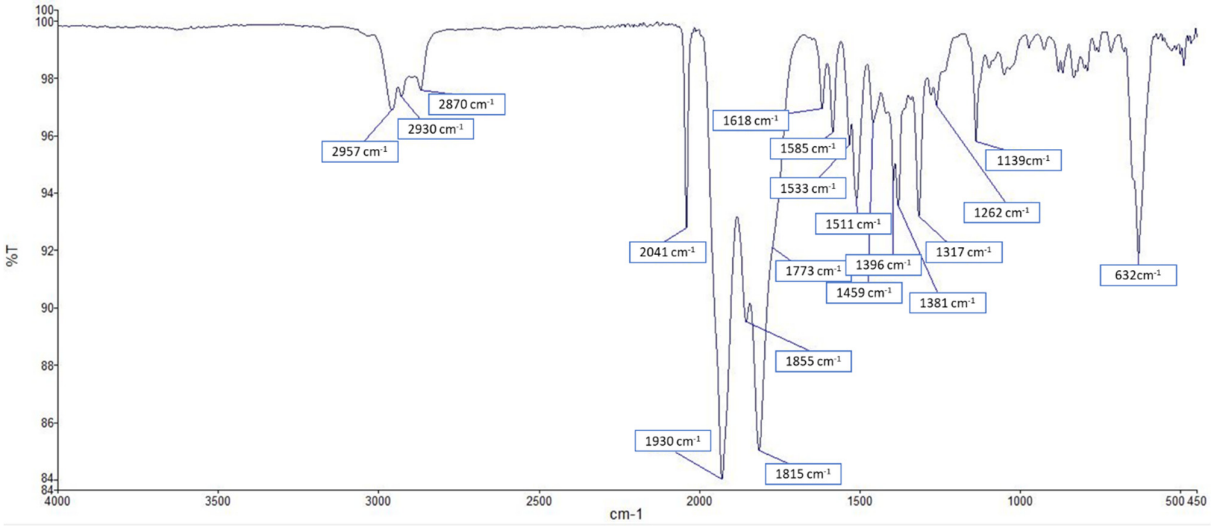

Figure S35: The ATR-IR spectrum of complex **3** (film).

Synthesis of (^{iPr}PNNP*)Fe^{I}Fe^{0}(CO)$_4$(μ-CO) (4):

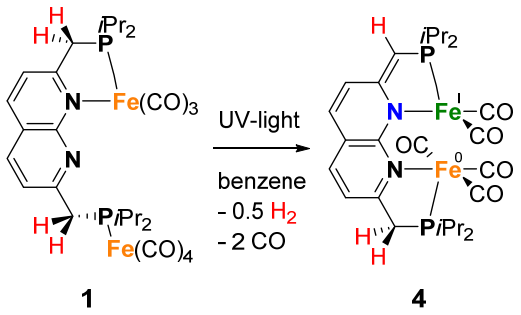

Method 1: Photolysis on small scale.

A solution of predominantly complex **2** (50.2 mg, approx. 69 μmol, containing ~15% complex **1**) in benzene (6.0 mL) was divided over six J-Young valved NMR tubes. These were placed around a double walled quartz flask, in which a high-pressure Hg-arc lamp (125 W) was placed (See Figure S60 A&B). The yellow-green solutions were irradiated for 30 min, which also resulted in boiling of the reaction mixtures.***** After cooling of the resulting brown solutions to ambient temperature, the NMR tubes were briefly opened to release the pressure that was build up in the headspace. Subsequently, the brown solutions were again irradiated for 30 min, resulting in dark brown solutions. Once more, after cooling to ambient temperature, the NMR tubes were briefly opened to release the pressure that was build up in the headspace. The resulting dark amber solutions were irradiated for an additional 60 min, after which the samples were combined and concentrated under a dynamic vacuum. The residue was washed with pentane (2 mL) and then extracted with Et_2O (2 x 2 mL). The extracts were combined and all volatiles were evaporated under a dynamic vacuum yielding **4** as a brown solid (39 mg, 61 μmol, 86%). **Note**: **4** prepared through this method contains a small unidentified impurity that is diamagnetic upon one-electron reduction (see Figure S61 and S62 and discussion down below).

*** Note:** Although the double walled quartz flask containing the light source was actively cooled – thereby preventing direct heat transfer from the light source to the reaction mixtures – the reaction mixtures boiled during the irradiation as the result of light absorption. In control experiments we found that both UV-light and heat are vital for the conversion of **1** to **4**. Bulk photolysis by irradiation of a benzene solution of **1** that is actively cooled results in only minor conversion of **1** to **4** after 12 h. Additionally, heating benzene solutions of **1** to 110 °C in a closed J. Young valved NMR tube for multiple days leads only partly to the formation of **4** and also complex **2**.

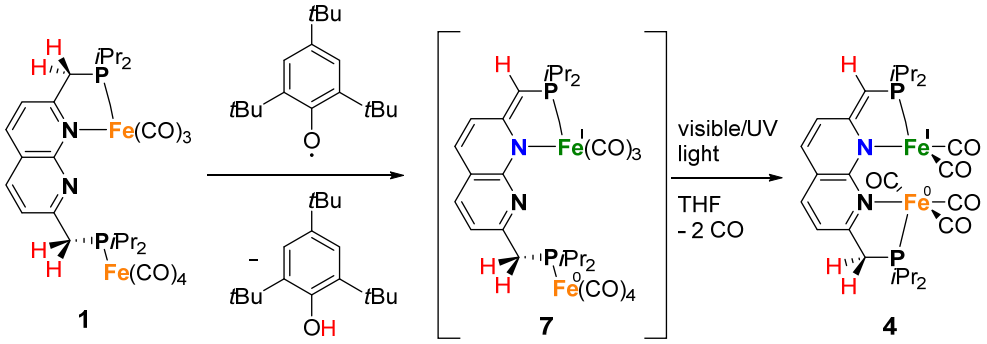

Method 2: H-atom abstraction followed by UV-promoted carbonyl dissociation.

A blue solution of 2,4,6-tri-*tert*-butylphenoxyl radical (TBP) (18.7 mg, 71.6 μmol) in THF (2.0 mL) was dropwise added to a green solution of complex **1** (50.0 mg, 71.6 μmol) in THF (2.0 mL), resulting in a brown solution containing **7** and 2,4,6-tri-*tert*-butylphenol (TBP–H) within one minute. After stirring

for 30 min, the solution was divided over two quartz EPR tubes, which were illuminated by a mild UV source for 16 h (see Figure 60-C). The resulting dark amber colored solutions were combined and concentrated under a dynamic vacuum. The residual solid was washed with pentane (2 x 2 mL) and then extracted with Et_2O (2 x 2 mL). The extracts were combined and all volatiles were evaporated under a dynamic vacuum, yielding **4** as a brown solid (35 mg, 53 µmol) that contains approx. 5 mol% TBP-H, based on ^1H NMR analysis with an external standard.

ATR-IR (film, N_2 flow): product of photolysis of 1 (method 1): ν = 2958, 2925, 2870, 2854, 1990, 1929, 1893, 1871, 1736, 1634, 1553, 1518, 1460, 1411, 1383, 1319, 1137, 836, 630 cm^{-1}.

ATR-IR (film, N_2 flow): product of H-atom abstraction from 1 (method 2): ν = 2960, 2929, 2901, 2871, 1991, 1930, 1895, 1874, 1634, 1553, 1517, 1461, 1412, 1318, 1137 cm^{-1}.

An ESI-MS measurement for complex **4** gave no signals corresponding to complex **4** possibly due to poor ionization of the sample.

* Despite several attempts, we were unable to obtain satisfactory elemental analysis of complex **4**.

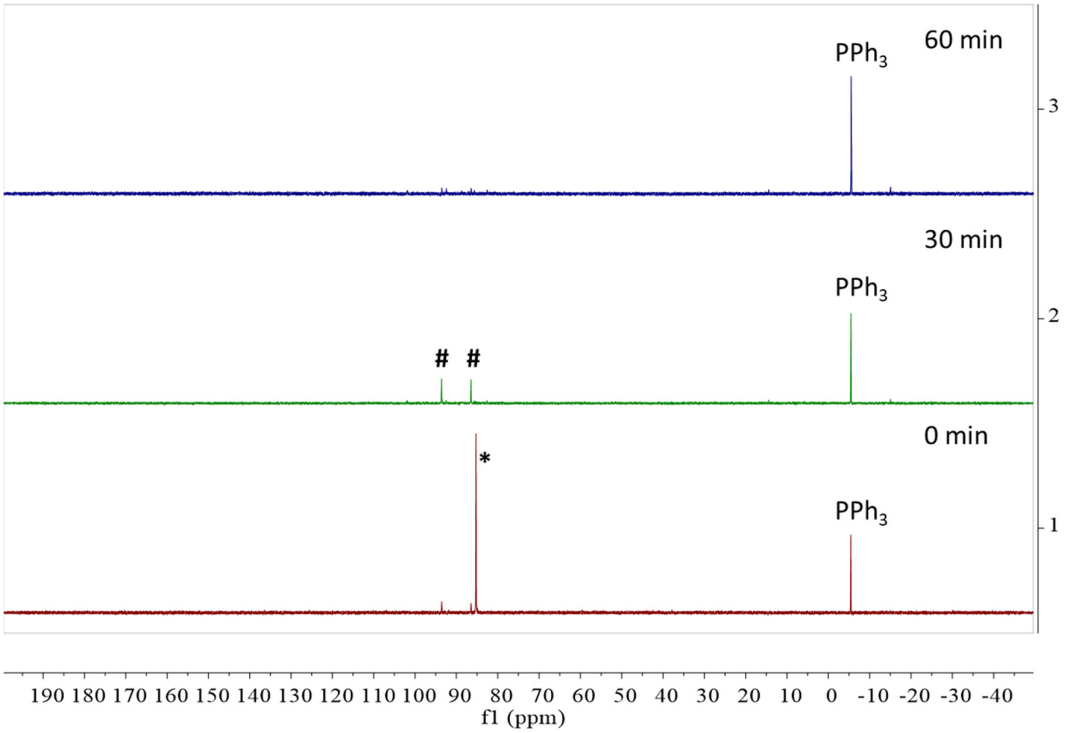

Figure S36: Stacked $^{31}P\{^1H\}$ NMR spectra of the photolysis of complex **2** (*) at different times in C_6H_6 with external reference of PPh_3 at 298 K. (bottom) yellow-green starting material prior to irradiation containing some complex **1** (#). (middle) green to brown solution obtained after irradiation of **2** for 30 min showing only the presence of complex **1**. (top) brown solution of **4** obtained after irradiation for 60 min having lost the diamagnetic resonances of complexes **1** and **2**.

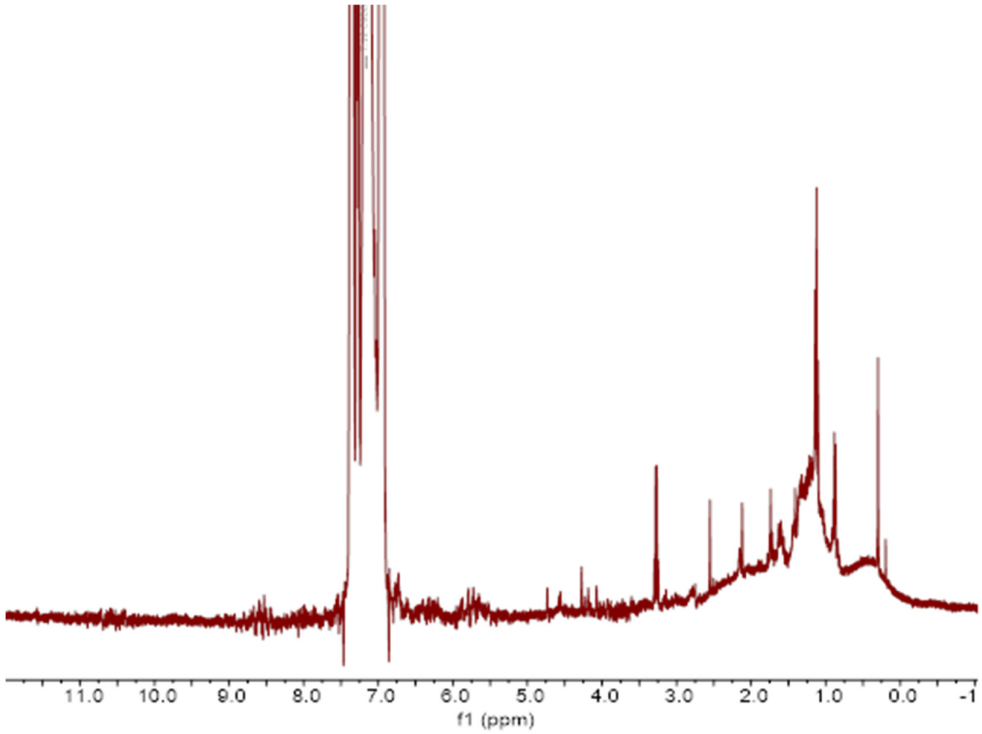

Figure S37: ^{1}H NMR spectrum of the photolysis of complex **2** after 120 min in C_6H_6 with external reference of PPh_3 at 298 K. The spectrum of paramagnetic complex **4** displays a few broad bumps around 2, 1 and 0.5 ppm.

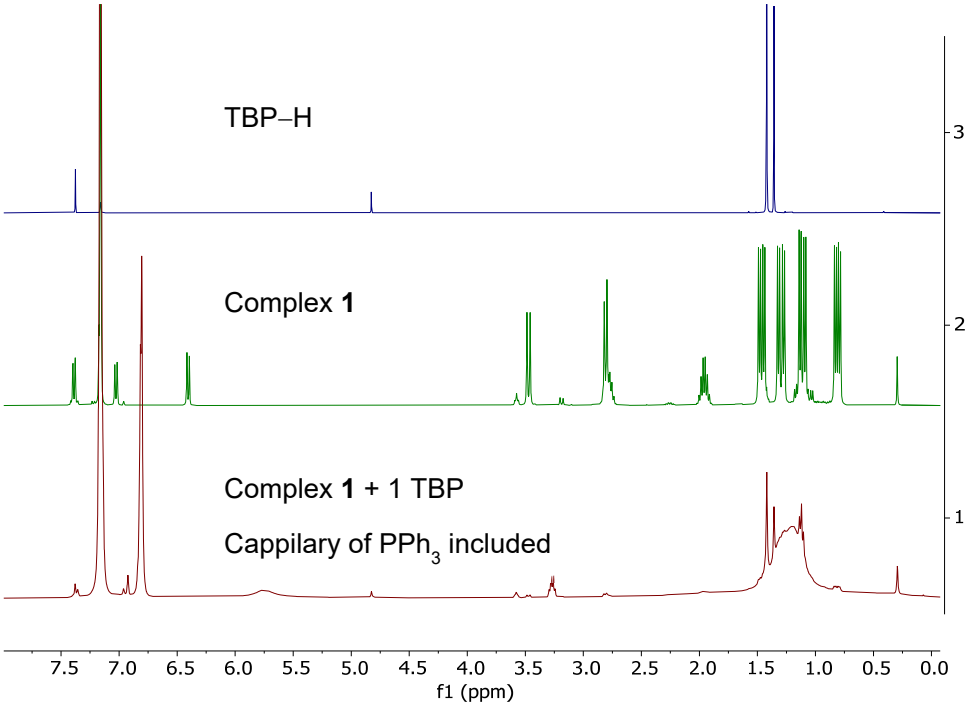

Figure S38: Stacked ^{1}H NMR spectra of the product obtained after treating complex **1** with 1 equiv of TBP with external reference of PPh_3 (bottom) and the reference spectra of complex **1** (middle) and TBP–H (top) in C_6D_6 at 298 K. The spectrum of paramagnetic complex **7** displays a few broad bumps around 5.7 and 1.3 ppm.

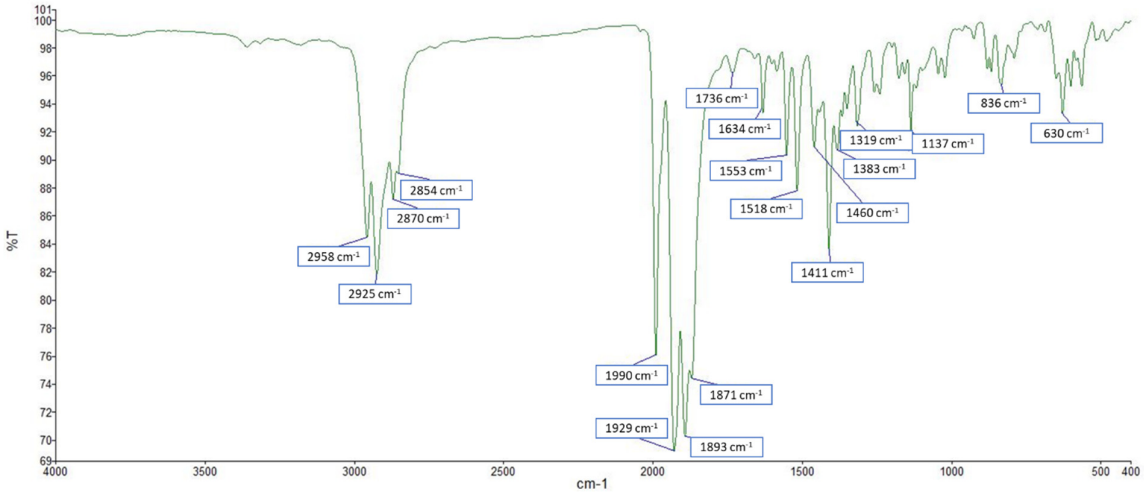

Figure S39: The ATR-IR spectrum of complex **4** prepared through method 1 (film).

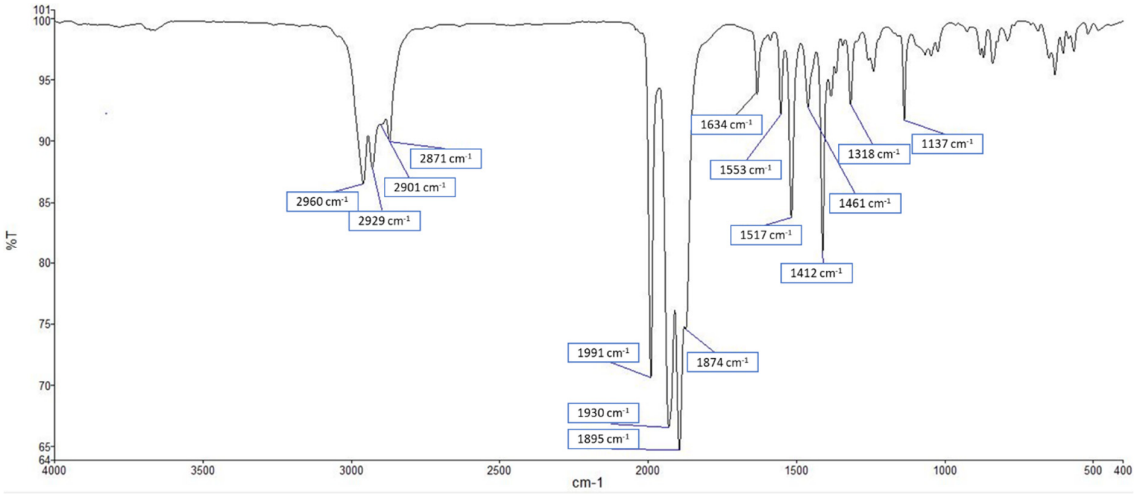

Figure S40: The ATR-IR spectrum of complex **4** prepared through method 2 (film).

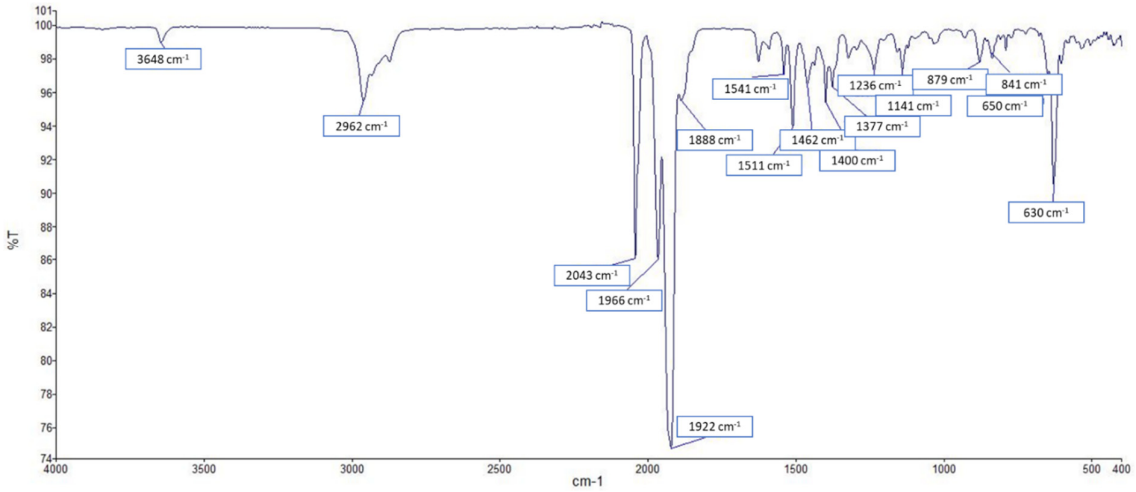

Figure S41: The ATR-IR spectrum of complex **7** and TBP-H, 30 min after the addition of TBP to **1** (film).

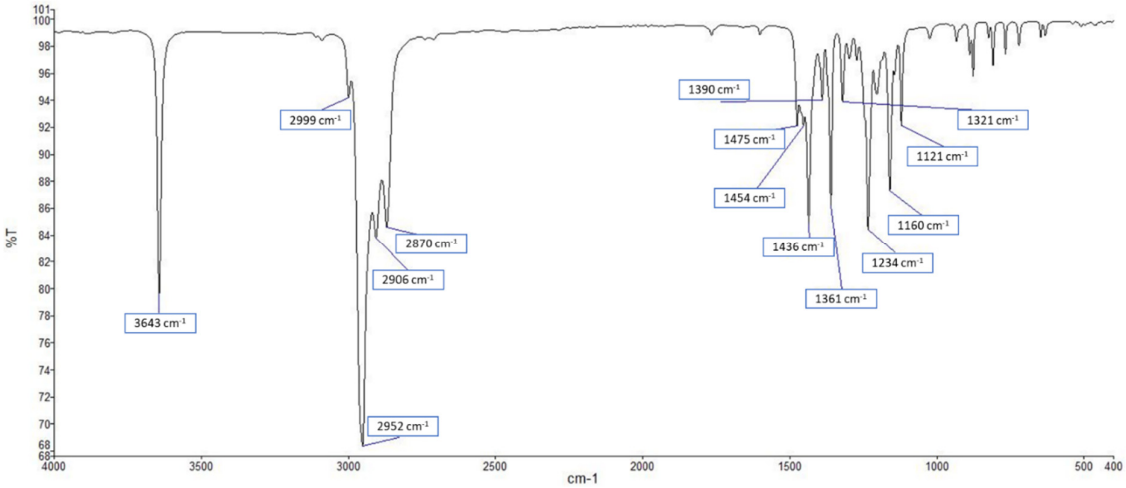

Figure S42: The ATR-IR spectrum of 2,4,6-tri-*tert*-butylphenol (TBP-H) (film).

Synthesis of K(THF)[Fe$_2$(*i*^{Pr}PNNP*)(CO)$_4$(μ-CO)] (5):

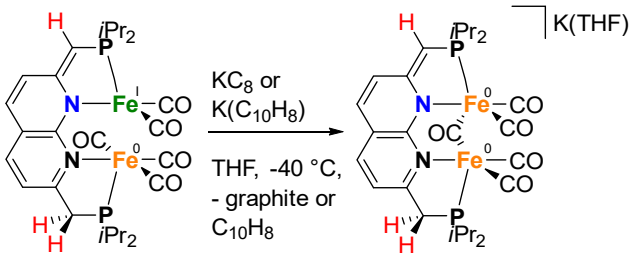

4 **5**

A freshly prepared solution of potassium naphthalenide (K($C_{10}H_8$)) (4.2 mg, 32.7 μmol) in THF (1.4 mL) was added dropwise to an amber-colored solution of complex **4** (22.1 mg, 34.4 μmol) in THF (2.0 mL) at -40 °C. The resulting yellow-brown solution was allowed to warm to ambient temperature and was stirred for 30 min, after which it was concentrated under a dynamic vacuum. The brown film was washed with Et_2O (2 mL) and benzene (2 x 2 mL) and then extracted with THF (2 x 1 mL). The extracts were combined and all volatiles were evaporated under a dynamic vacuum yielding **5** as a brown film (15.8 mg, 21.0 μmol, 64%).

*This reaction can additionally be performed with KC_8 as reductant. Since the amount of reductant can be more accurately weighed using K($C_{10}H_8$), this is the reductant of choice for this reaction.

^{1}H NMR (400 MHz, THF-*d*$_8$, 298 K): δ 6.48 (d, $^3J_{H,H}$ = 7.1 Hz, 1H), 6.17 (d, *J* = 9.0 Hz, 1H), 6.11 (d, $^3J_{H,H}$ = 9.5 Hz, 1H), 6.08 (d, $^3J_{H,H}$ = 7.2 Hz, 1H), 4.26 (d, $^2J_{H,P}$ = 2.8 Hz, 1H), 3.18 (d, $^2J_{H,P}$ = 8.6 Hz, 2H), 2.32 (*two overlapping heptd resonances of -C**H**(CH$_3$)$_2$ with* $^2J_{H,P}$ and $^3J_{H,H}$ *couplings of 7-8 Hz*, m, *J* = 7.7 Hz, 4H), 1.38 (*overlaps with dd at 1.34 ppm*, dd, $^3J_{H,P}$ = 12.9 Hz, $^3J_{H,H}$ = 7.1 Hz, 6H), 1.34 (*overlaps with dd at 1.38 ppm*, dd, $^3J_{H,P}$ = 12.6 Hz, $^3J_{H,H}$ = 7.1 Hz, 6H), 1.27 (dd, $^3J_{H,P}$ = 13.5 Hz, $^3J_{H,H}$ = 7.1 Hz, 6H), 1.13 (dd, $^3J_{H,P}$ = 12.5 Hz, $^3J_{H,H}$ = 7.1 Hz, 6H).

^{31}P NMR (162 MHz, THF-*d*$_8$, 298 K): δ 100.4 (d, $^4J_{P,P}$ = 5.2 Hz), 90.3 (d, $^4J_{P,P}$ = 5.2 Hz).

^{13}C NMR (101 MHz, THF-d_8, 298 K): δ 166.0 (d, $^{2}J_{C,P}$ = 23.9 Hz), 163.8 (t, $^{4}J_{C,P}$ = 3.3 Hz), 159.7 (d, $^{2}J_{C,P}$ = 9.5 Hz), 131.2, 126.8, 121.3 (d, $^{3}J_{C,P}$ = 17.1 Hz), 118.1, 108.6 (d, $^{4}J_{C,P}$ = 9.0 Hz), 87.5 (d, $^{1}J_{C,P}$ = 35.2 Hz), 39.6 (d, $^{1}J_{C,P}$ = 14.0 Hz), 30.1 (d, $^{1}J_{C,P}$ = 24.2 Hz), 27.4 (d, $^{1}J_{C,P}$ = 16.2 Hz), 20.4 (d, $^{2}J_{C,P}$ = 3.7 Hz), 20.0, 19.2 (d, $^{2}J_{C,P}$ = 4.4 Hz), 18.5.

One electron reduction using K($C_{10}H_8$): Anal. Calcd. For $C_{31}H_{43}O_6N_2P_2Fe_2K \cdot 0.5$ THF (C_4H_8O): C, 50.27; H, 6.01; N, 3.55. Found C, 50.23; H, 5.79; N, 3.33.

Inclusion of 0.5 equiv of THF for the elemental analysis of complex **5** leads to a satisfactory elemental analysis. The THF is included here, since it was observed in the ^{1}H NMR spectrum of complex **5**.

ATR-IR (film, N_2 flow): ν = 2957 (m), 2928 (m), 2870 (m), 1993 (s), 1930 (s), 1899 (s), 1850 (s), 1635 (m), 1545 (w), 1514 (m), 1461 (w), 1411 (m), 1382 (w), 1317 (w), 1136 (w) cm^{-1}.

ESI-MS: Despite several attempts, no signals corresponding to complex **5** were found, possibly due to the sensitive nature or poor ionization of the sample.

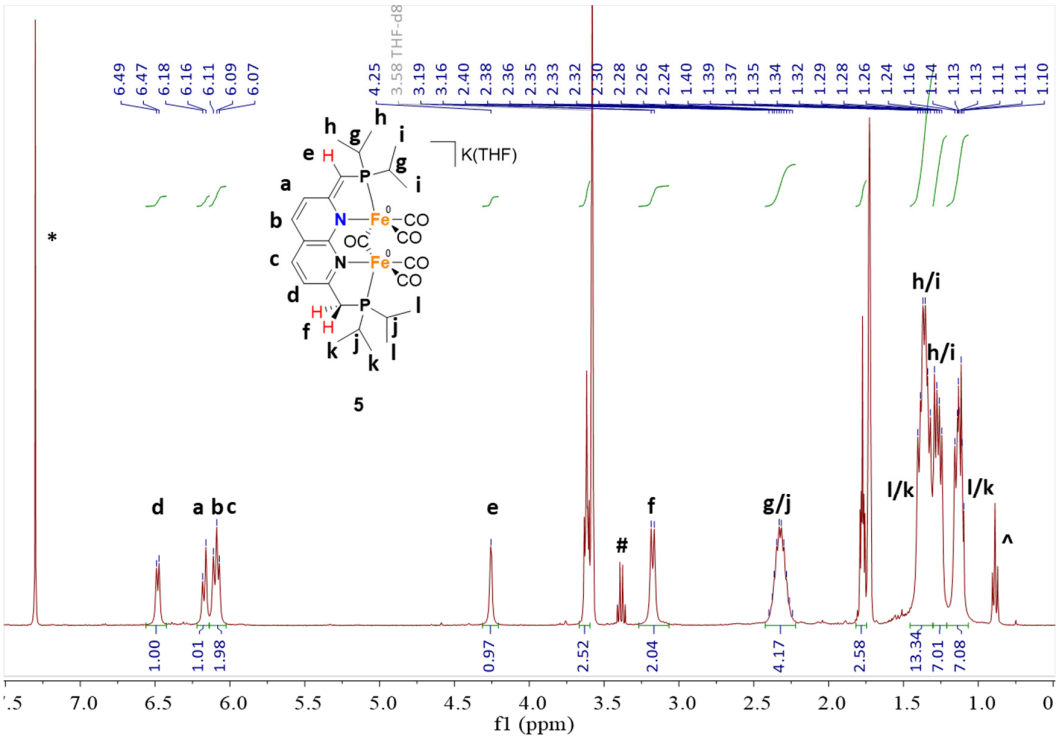

Figure S43: The ^{1}H NMR spectrum of **5** in THF-d_8 at 298 K. * denotes residual benzene, # denotes residual Et_2O and ^ denotes residual pentane.

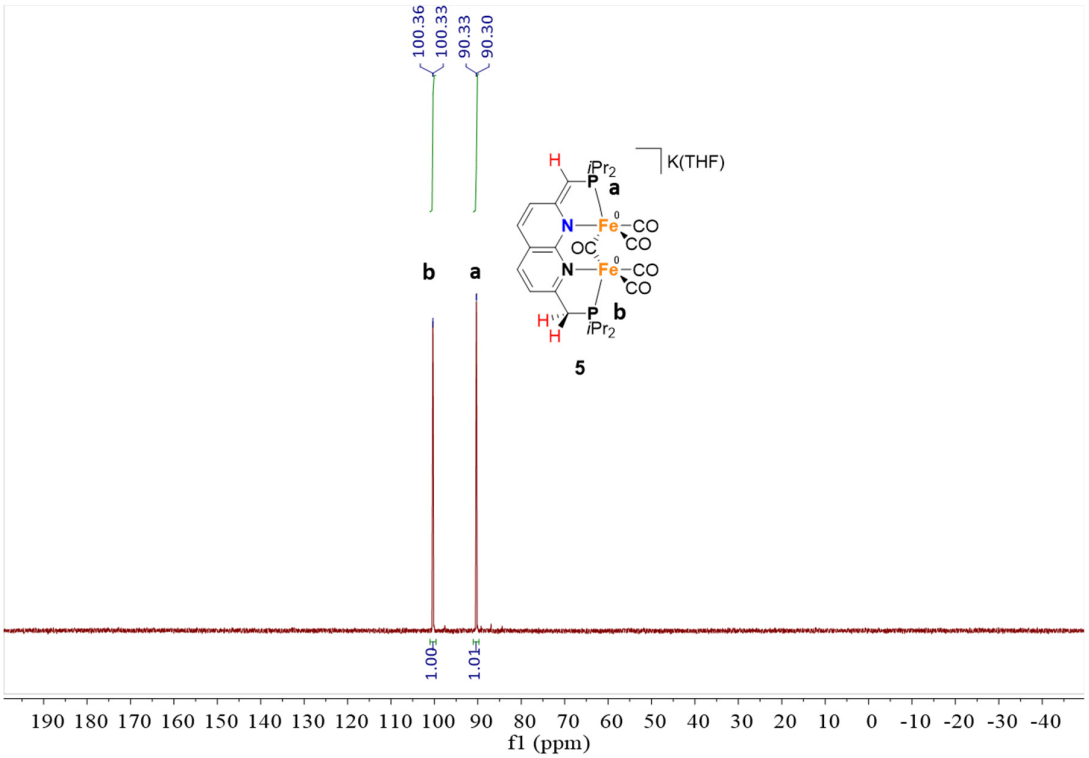

Figure S44: The $^{31}P\{^{1}H\}$ NMR spectrum of **5** in THF-d_8 at 298 K.

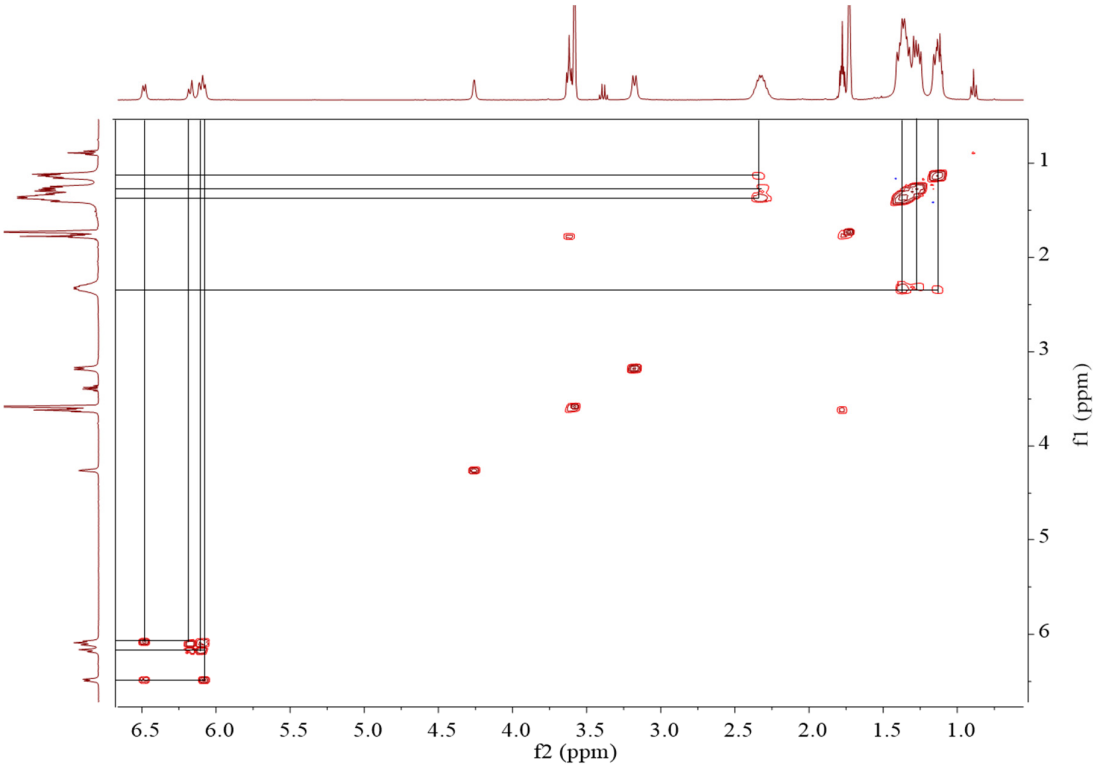

Figure S45: The ^{1}H-^{1}H COSY NMR spectrum of **5** in THF-d_8 at 298 K.

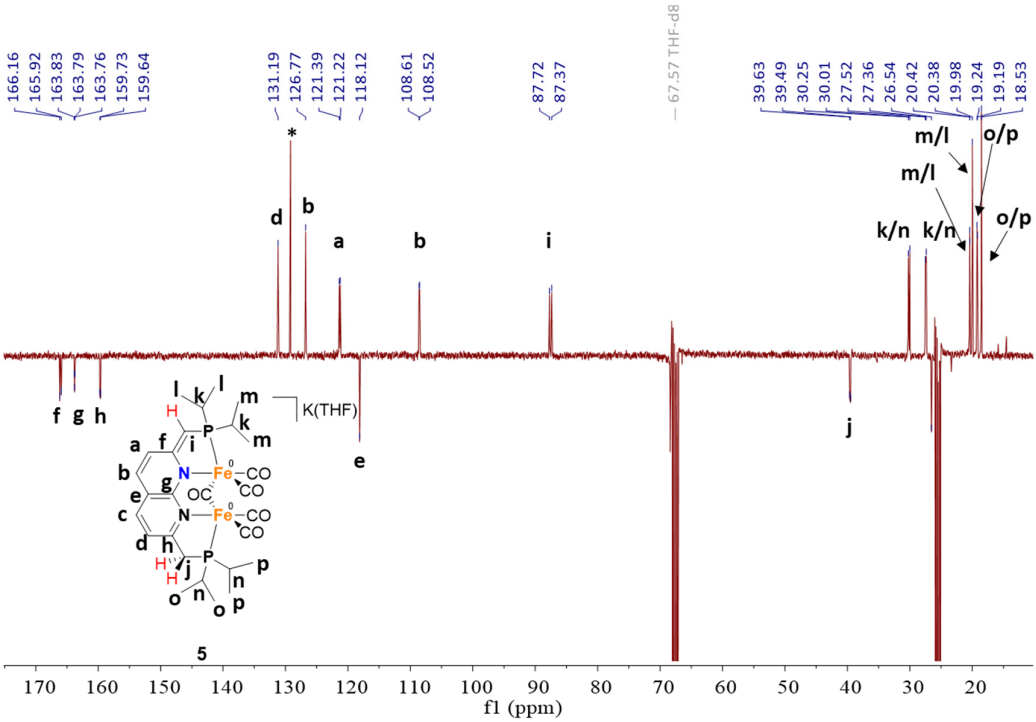

Figure S46: The $^{13}C\{^{1}H\}$-APT NMR spectrum of **5** in THF-d_8 at 298 K. The resonance marked with * is assigned to residual C_6H_6.

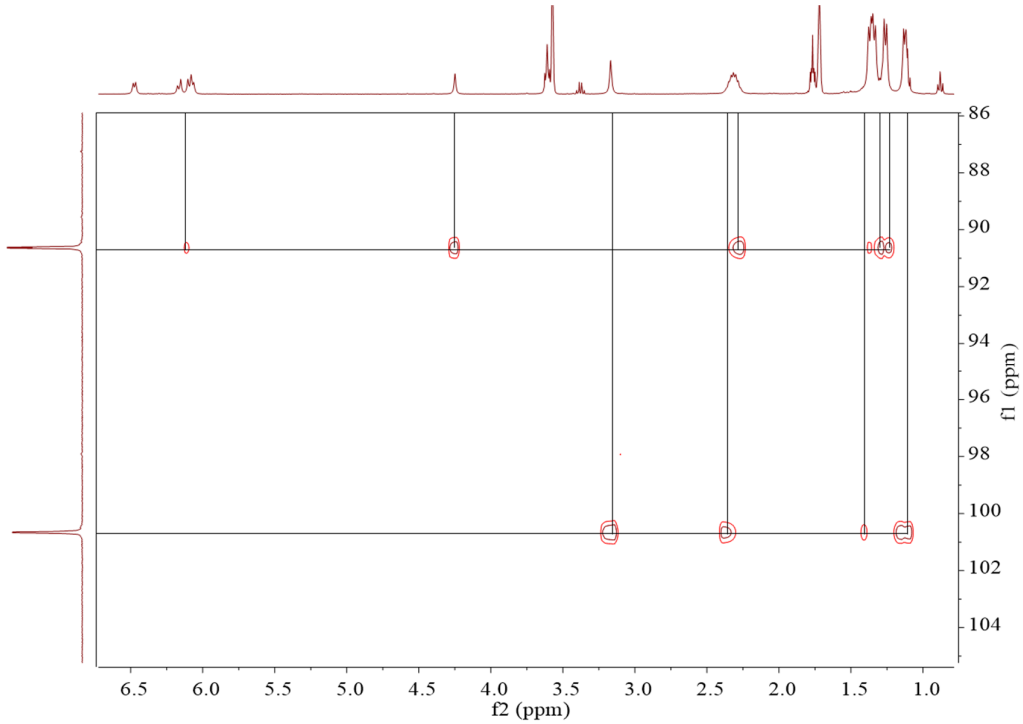

Figure S47: The ^{1}H-^{31}P HMBC NMR spectrum of **5** in THF-d_8 at 298 K.

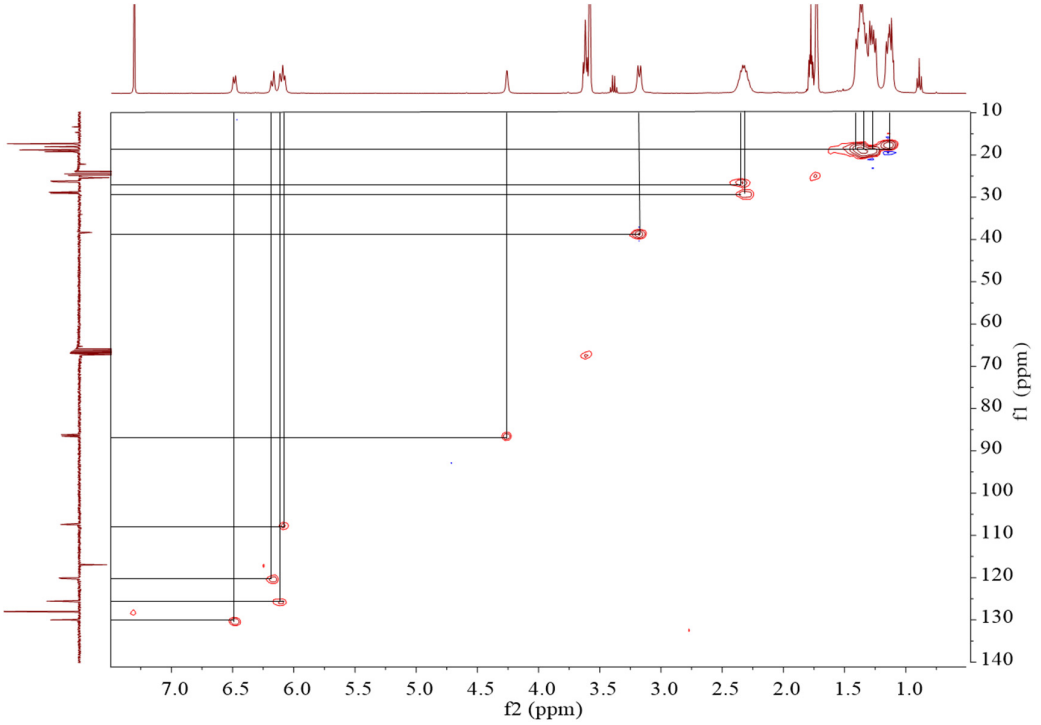

Figure S48: The ^{1}H-^{13}C HMQC NMR spectrum of **5** in THF-d_8 at 298 K.

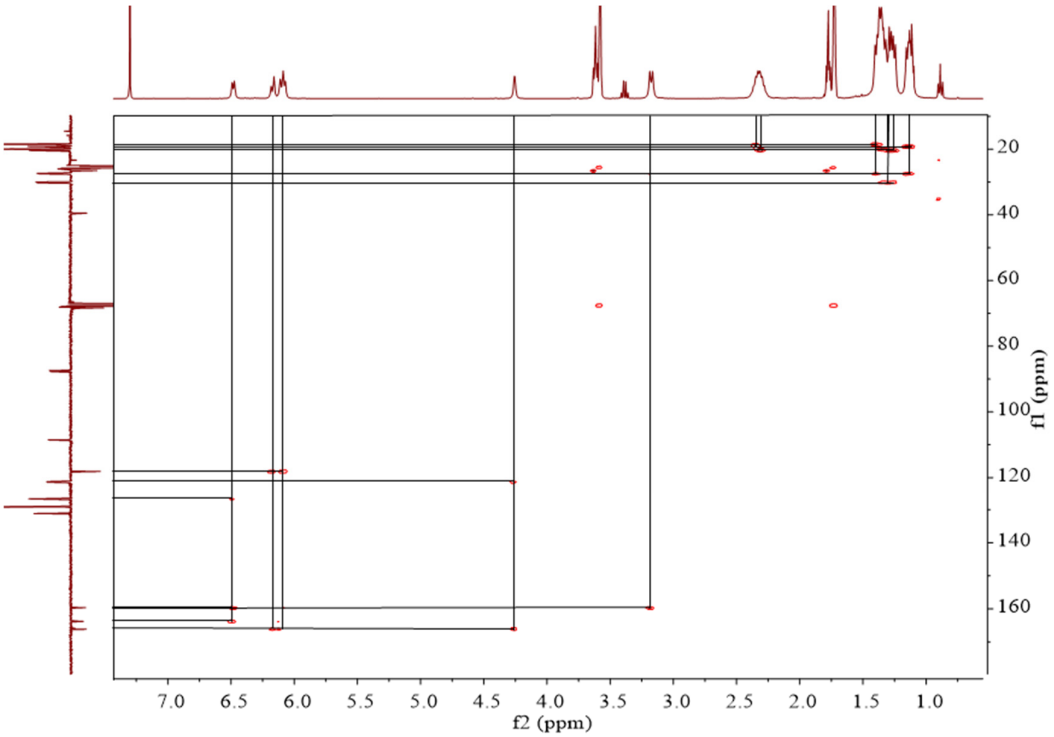

Figure S49: The ^{1}H-^{13}C HMBC NMR spectrum of **5** in THF-d_8 at 298 K.

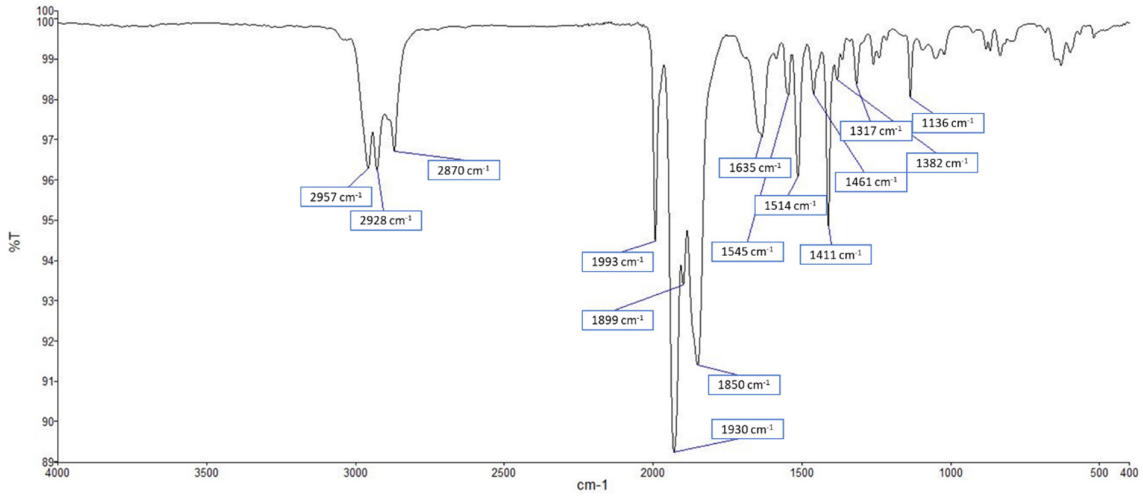

Figure S50: The ATR-IR spectrum of complex **5** (film).

Synthesis of $Fe_2(^{iPr}PNNP)(CO)_4(\mu\text{-}CO)$ (6):

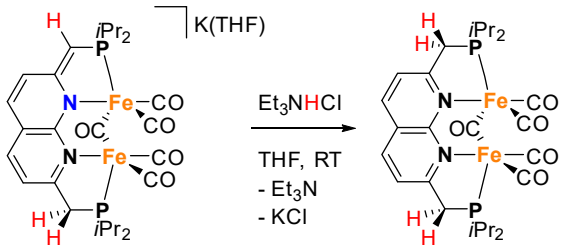

A suspension of Et_3NHCl (3.1 mg, 22.5 µmol, 1.02 equiv) in THF (2 mL) was added to a stirred solution of complex **5** (16.7 mg, 22.2 µmol) in THF (2 mL), causing a gradual color change from yellow-brown to red-brown. After 30 min, all volatiles were removed under a dynamic vacuum, the residue was washed with Et_2O (2 x 2 mL) and then extracted with benzene (4 x 2 mL). The extracts were combined and all volatiles were removed under a dynamic vacuum to give a brown film, which was scratched into a powder using a metal spatula. Further drying under a dynamic vacuum provided **6** as a light brown solid (13.4 mg, 20.9 µmol) in 94% yield.

^{1}H NMR (400 MHz, THF-d_8, 298 K): δ 7.60 (d, $^3J_{H,H}$ = 8.1 Hz, 2H), 7.19 (d, $^3J_{H,H}$ = 8.1 Hz, 2H), 3.43 (d, $^2J_{H,P}$ = 9.3 Hz, 4H), 2.46 (heptd, $^2J_{H,P}$ = 7.1 Hz, $^3J_{H,H}$ = 7.1 Hz, 4H), 1.44 (dd, $^3J_{H,P}$ = 15.7 Hz, $^3J_{H,H}$ = 7.1 Hz, 12H), 1.15 (dd, $^3J_{H,P}$ = 12.9 Hz, $^3J_{H,H}$ = 7.1 Hz, 12H).

^{31}P NMR (162 MHz, THF-d_8, 298 K): δ 100.9 (s).

^{13}C NMR (101 MHz, THF-d_8, 298 K): δ 164.9 (dt, $^2J_{C,P}$ = 9.2 Hz, $^6J_{C,P}$ = 2.7 Hz), 161.9 (t, $^5J_{C,P}$ = 3.3 Hz), 134.6, 125.5, 121.4 – 121.1 (m), 40.1 (dt, $^1J_{C,P}$ = 13.7 Hz, $^6J_{C,P}$ = 3.0 Hz), 28.5 – 26.1 (m), 19.2 (m), 18.6.

ATR-IR (film, N_2 flow): ν = 2956 (m), 2929 (m), 2891 (m), 2871 (m), 1992 (m), 1945 (s), 1886 (s), 1695 (m), 1517 (m), 1461 (w), 1413 (w), 1384 (w), 1260 (s), 1315 (w), 600 (w), 585 (w) cm^{-1}.

* Despite several attempts, we were unable to obtain satisfactory elemental analysis of a spectroscopically clean sample of complex **6**.

ESI-MS: Complex **6** $Fe_2(^{iPr}PNNP)(CO)_4(\mu\text{-}CO)$. Exact mass calculated for $C_{27}H_{36}O_5Fe_2N_2P_2$: 642.1. Found: $[M]^+$ at 642.0 *m/z*.

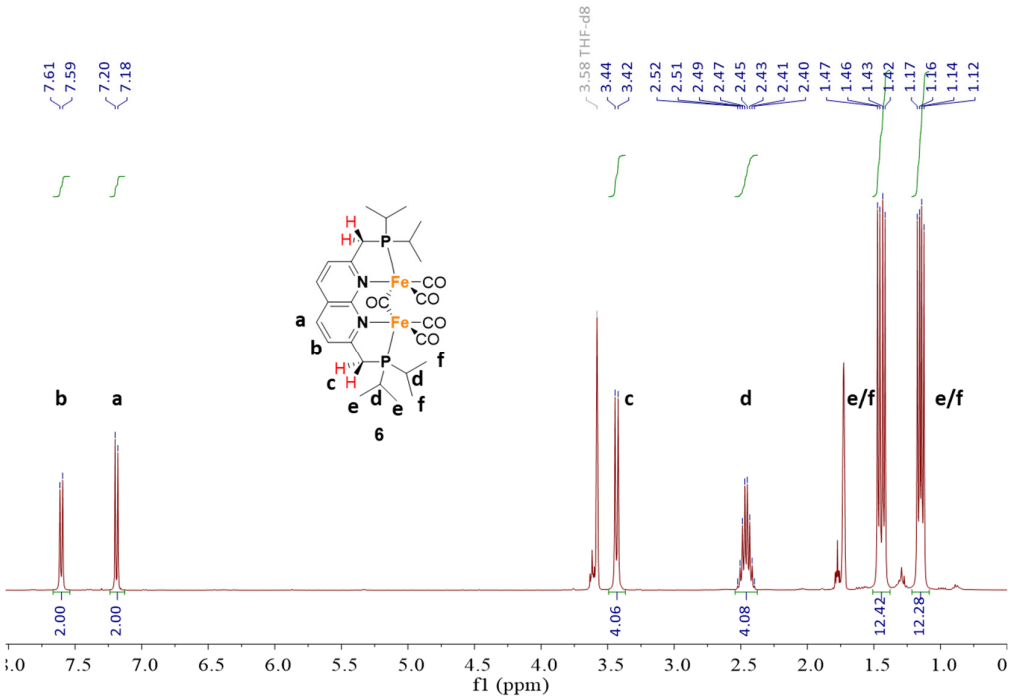

Figure S51: The ^{1}H NMR spectrum of **6** in THF-d_8 at 298 K.

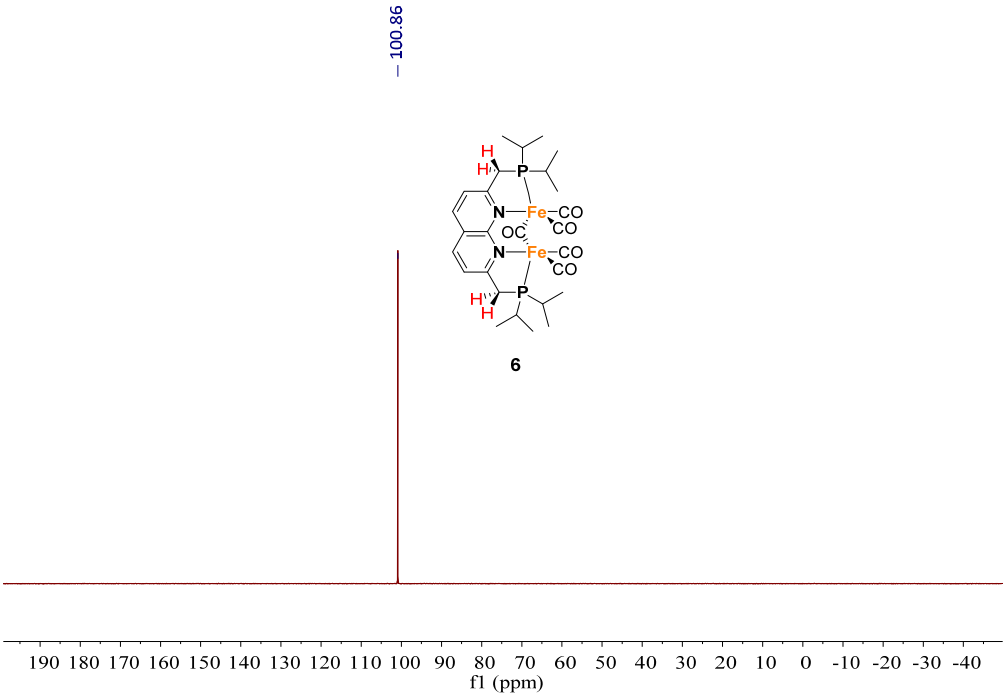

Figure S52: The $^{31}P\{^{1}H\}$ NMR spectrum of **6** in THF-d_8 at 298 K.

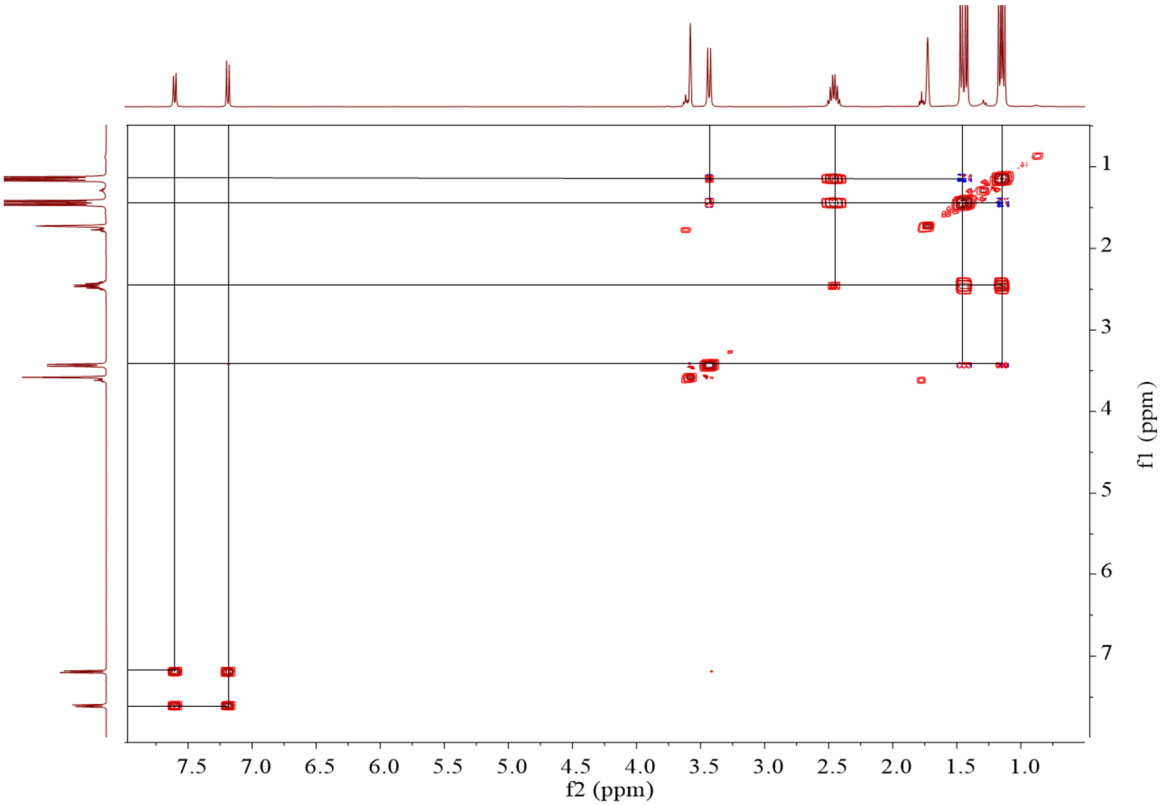

Figure S53: The ^{1}H-^{1}H COSY NMR spectrum of **6** in THF-d_8 at 298 K.

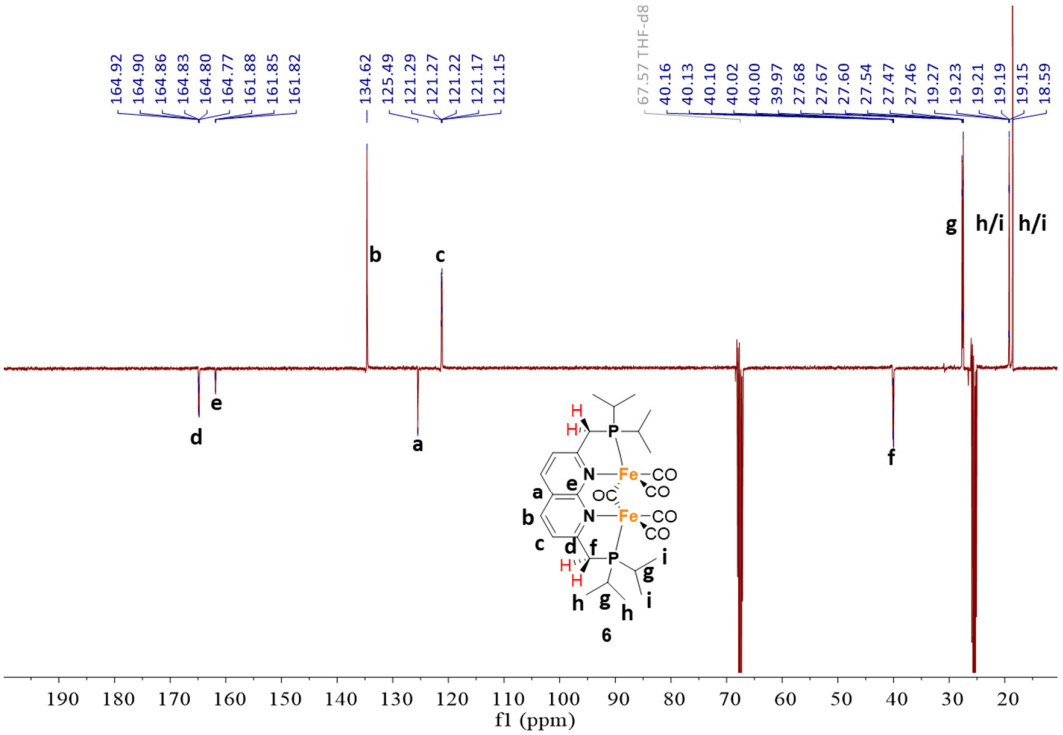

Figure S54: The ^{13}C{^{1}H}-APT NMR spectrum of **6** in THF-d_8 at 298 K.

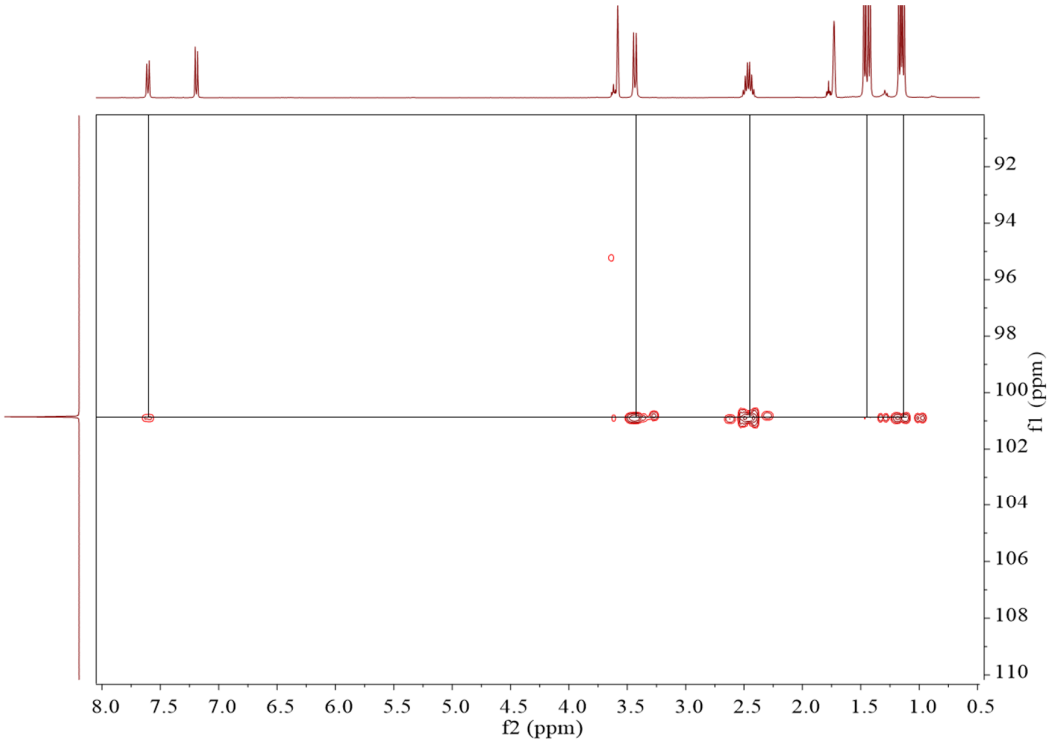

Figure S55: The ^{1}H-^{31}P HMBC NMR spectrum of **6** in THF-d_8 at 298 K.

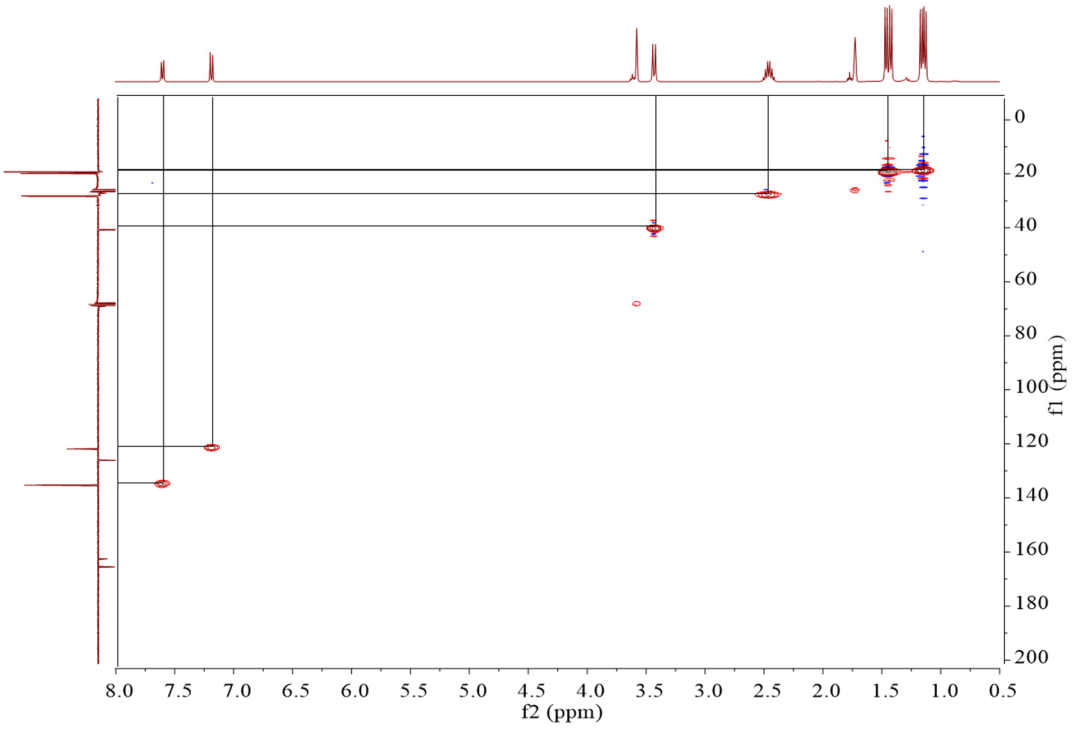

Figure S56: The ^{1}H-^{13}C HMQC NMR spectrum of **6** in THF-d_8 at 298 K.

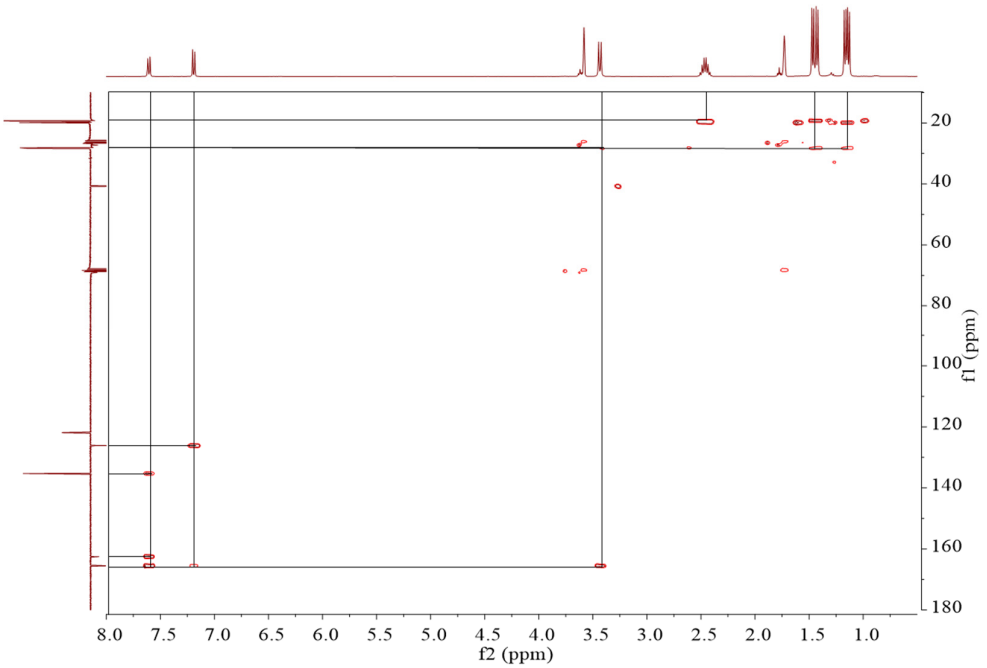

Figure S57: The ^{1}H-^{13}C HMBC NMR spectrum of **6** in THF-d_8 at 298 K.

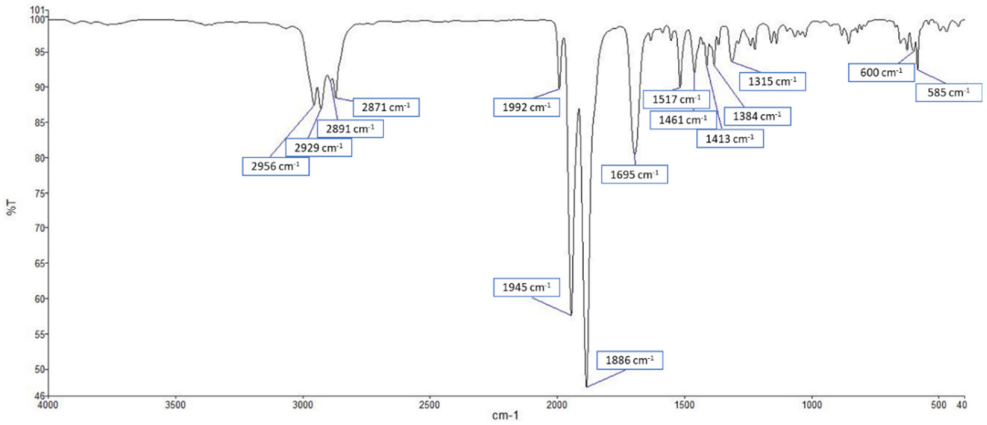

Figure S58: The ATR-IR spectrum of complex **6** (film).

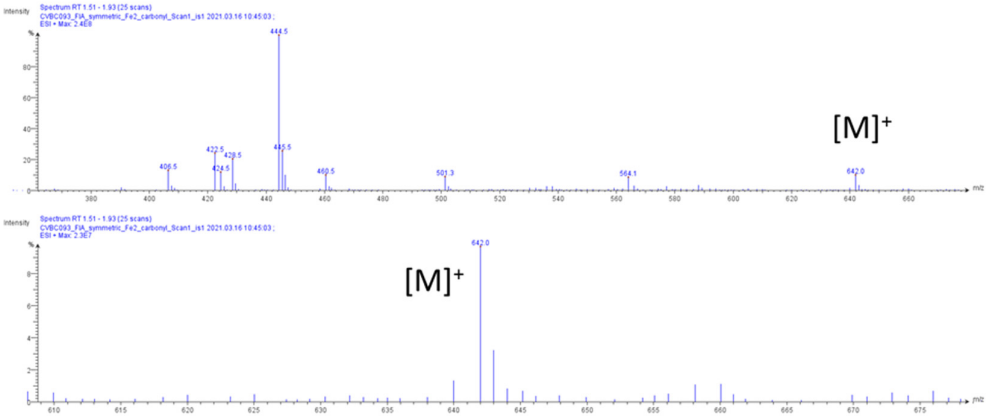

Figure S59: The ESI-MS spectrum of complex **6** in positive mode displaying the signal corresponding to $[M]^+$ and its isotope pattern.

UV-irradiation experiments

For the photolysis/irradiation experiments, a set-up was built that consists of a double walled quartz tube and a UV light source. The UV light source consists of an electrical ballast (ELT 5112400 VMI 12/23-2 vsa HPLN designed for lamps with a power of 125 W), igniter (Vossloh Schwabe 508667 condensator 10µF) and a high-pressure mercury vapor lamp (Osram HQL 125W E27) with a power of 125 W. This type of lamp has multiple emission lines between 250 and 400 nm and emits blue and green light in the visible spectrum. This lamp is placed inside the double-walled quartz tube, which is actively cooled with water during photolysis experiments, see figure S60A. J-Young valved NMR tubes containing benzene solutions of complexes **1**/**2** are then placed around the mercury vapor lamp.

Photolysis of complex **7** takes place under milder conditions than for complex **1**, and CO loss is even observed from exposure to fluorescent lighting in the laboratory. Utilization of a TLC lamp as weak UV source (365 nm) results in quantitative conversion of **7** to **4** within 16 h. (figure S60C).

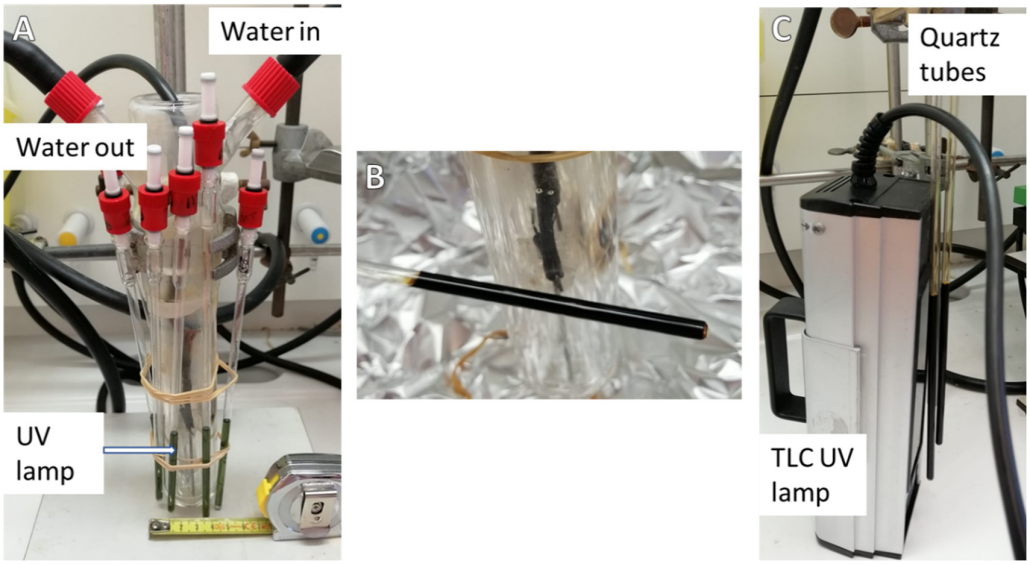

Figure S60: Photolysis experimental set-up. **(A)** A typical set-up for the photolysis of complexes **1** or **2**. **(B)** Resulting product after photolysis of complex **1**. **(C)** Set-up used for photolysis of complex **7**.

One-electron reduction of 4 obtained through method 1:

As described in the main text, the synthesis of complex **4** through method 1 (photolysis) is poorly scalable. Additionally, an unidentified byproduct is often observed after one-electron reduction of complex **4**. Comparison on the IR spectra of complex **4** (figures S39 and S40) obtained by the two different methods show that the product obtained via method 1 displays additional weak CO bands. This indicates that a second species is present that is observed by NMR spectroscopy after one-electron reduction of the paramagnetic photolysis product. Between various batches, the unidentified diamagnetic byproduct was present between 10% and 50% compared to complex **5** based on ^{31}P NMR spectroscopy. The two species could not be separated. Although the structure of this byproduct was not elucidated, it is characterized by ^{31}P and ^{1}H NMR spectroscopy in THF-d_8 at 298 K as shown in figure S61 and S62. The ^{31}P{^{1}H} NMR spectrum displays two doublets ($J_{P,P}$ = 5.5 Hz) for the unidentified product. The ^{1}H NMR spectrum of the unidentified product shows characteristic singlet at 4.40 ppm and doublet at 3.10 ppm with an integral ratio of 1 : 2, corresponding to a methine and methylene linker, respectively. Based on these results it is evident that the unidentified product contains an **^{iPr}PNNP*** fragment. Due to the coupling observed in its ^{31}P{^{1}H} NMR spectrum, we hypothesize that this product contains a diiron carbonyl core that allows long-range communication of the phosphorous

atoms. Notably, protonation of a mixture of complex **5** and the unidentified product with Et_3NHCl in THF leads to the conversion of both species to complex **6** according to ^{31}P and ^{1}H NMR spectroscopy. This indicates that **5** and the byproduct are closely related and can be isomers. The synthesis and characterization of complex **5** and **6** are presented in the next section.

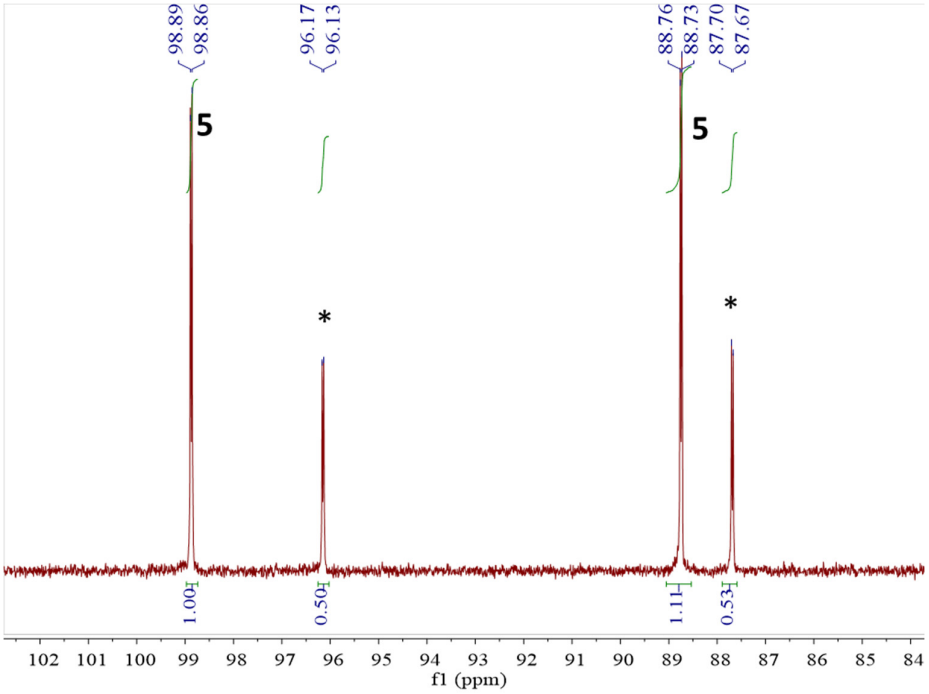

Figure S61: The $^{31}P\{^{1}H\}$ NMR spectrum of **5** and the unidentified byproduct in THF-d_8 at 298 K. The resonances marked with a * are assigned to the unidentified byproduct.

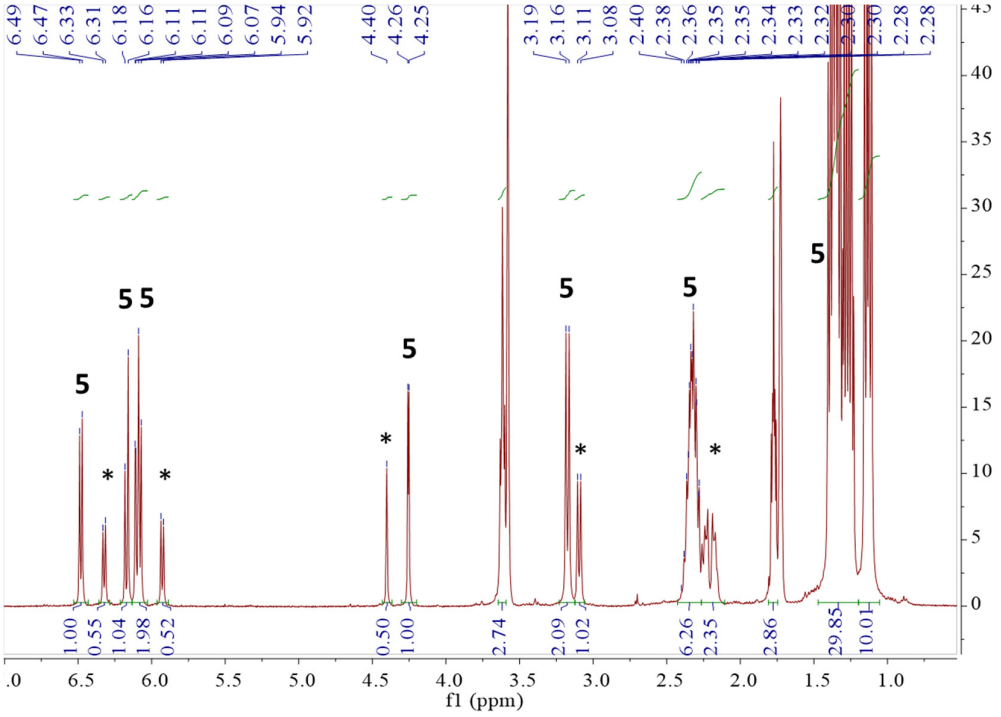

Figure S62: The ^{1}H NMR spectrum of **5** and the unidentified byproduct in THF-d_8 at 298 K. The resonances marked with a * are assigned to the unidentified byproduct.

HAT immediately followed by one-electron reduction

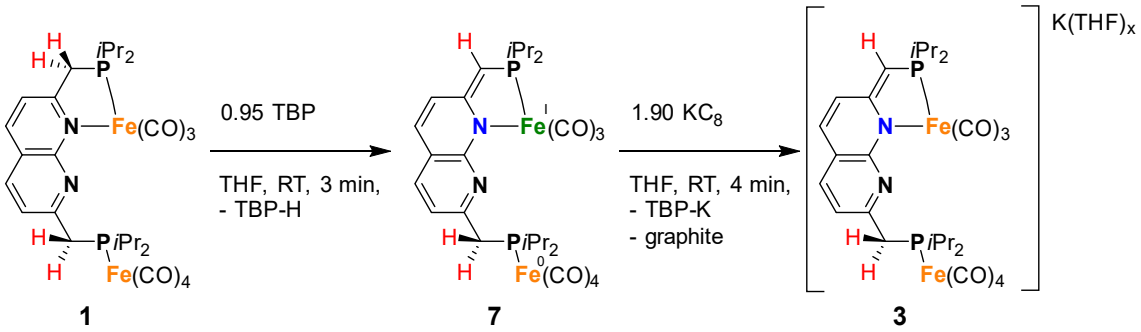

In the process of converting **1** to **4** through complex **7** via a hydrogen atom transfer (HAT) pathway using a phenoxyl radical, complex **1** loses a hydrogen atom and two CO ligands. Since we were unsuccessful in growing crystals of **7**, we proposed that rapid one-electron reduction of a mixture of **7** and TBP-H, formed after treating **1** with TBP, could give more structural information about complex **7**. Hence, we performed a reaction of **1** with TBP – thereby generating a mixture of **7** and TBP-H – and added a THF suspension of 1.9 equiv of KC_8 (excess to react with the TBP-H) within 10 minutes, resulting in the formation of a red brown solution. After filtration of the suspension, the reaction mixture was analyzed by ^{31}P NMR spectroscopy, which revealed that the main component is complex **3** (shown in figure S62), together with small amounts of starting material (complex **1** and **2**) present. As such, the hydrogen atom abstraction followed by one-electron reduction results in net proton loss from complex **1**. This result indicates that hydrogen atom abstraction from **1** yields a species with the same number of CO ligands as in the starting material, i.e. **7**, and that subsequent irradiation of **7** by UV-light causes the dissociation of two CO ligands to give **4.**

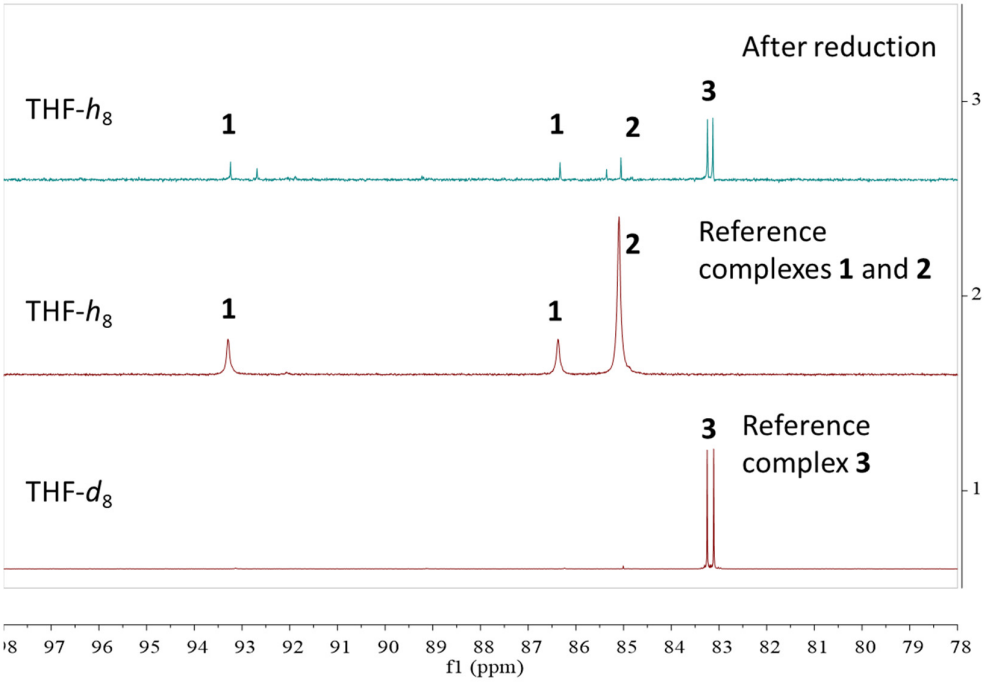

Figure S63: The stacked $^{31}P\{^{1}H\}$ NMR spectra of the reaction between **1** and TBP immediately followed by addition of KC_8 after filtration (top) and reference spectra of complexes **1**, **2** and **3** (middle and bottom) in THF-d_8 or THF-h_8 at 298 K.

Solvent screening and thermal CO dissociation

Reaction between ^{iPr}**PNNP** and 2 equiv $Fe_2(CO)_9$ in THF gives a dark green mixture containing an approximately 1 : 1 ratio between complexes **1** and **2** after 3 h, see Figure S64. Heating this reaction mixture to reflux under a flow of N_2 (g) does not change the integral ratio between **1** and **2** and thus does not lead to productive CO dissociation. Different solvents were chosen to react the ^{iPr}**PNNP** ligand with 2 equiv $Fe_2(CO)_9$ to study the selectivity of this reaction in different solvents.

Heating a mixture of ^{iPr}**PNNP** with 2 equiv $Fe_2(CO)_9$ in refluxing benzene leads to formation of iron carbonyl complexes **1** and **2** based on the $^{31}P\{^1H\}$ NMR spectra measured at different time intervals as shown in Figure S65, albeit slower than in THF. Multiple species and resonances attributed to free ligand are observed after refluxing the mixture overnight and after four days, which result in formation of a brown mixture. The main singlet observed after four days is assigned to complex **2**. The results indicate that the reaction in refluxing benzene does not lead to a higher selectivity for the synthesis of complex **1** or **2**.

Similar results are obtained when the reaction is performed in refluxing toluene, albeit faster than in refluxing benzene.

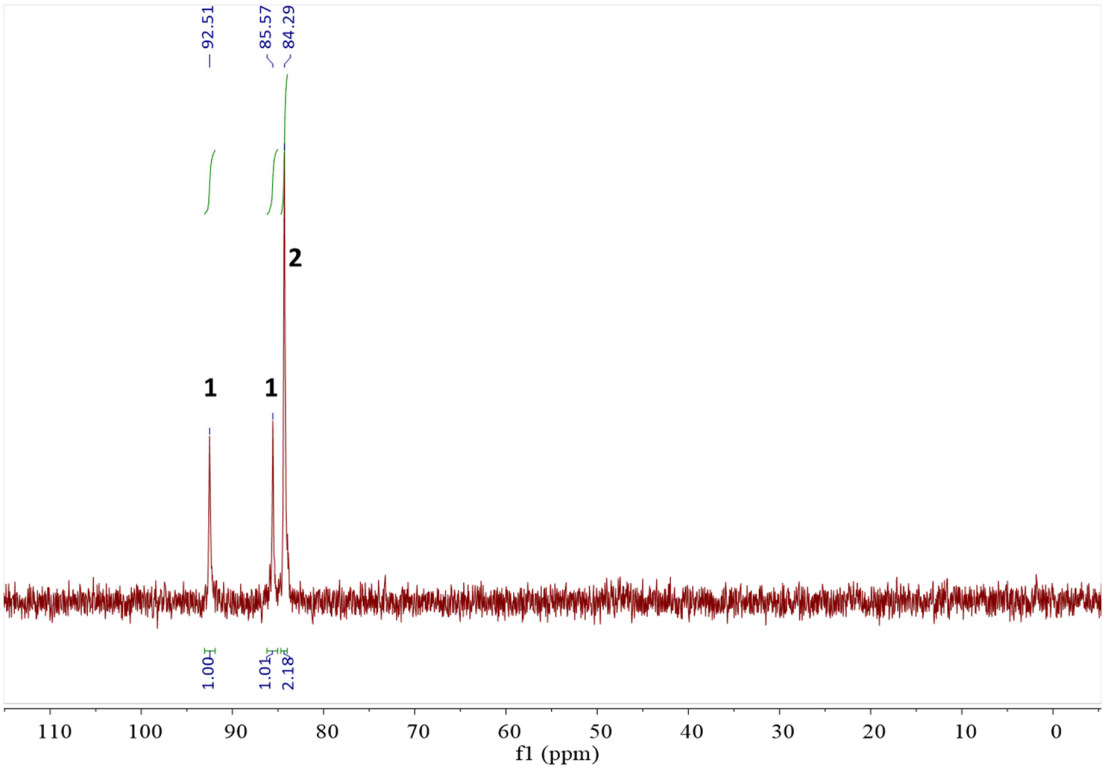

Figure S64: The $^{31}P\{^1H\}$ NMR spectrum of the reaction mixture between ^{iPr}**PNNP** and 2 equiv $Fe_2(CO)_9$ after 3 h in THF-h_8 at 298 K. The resonances are assigned to complexes **1** and **2**.

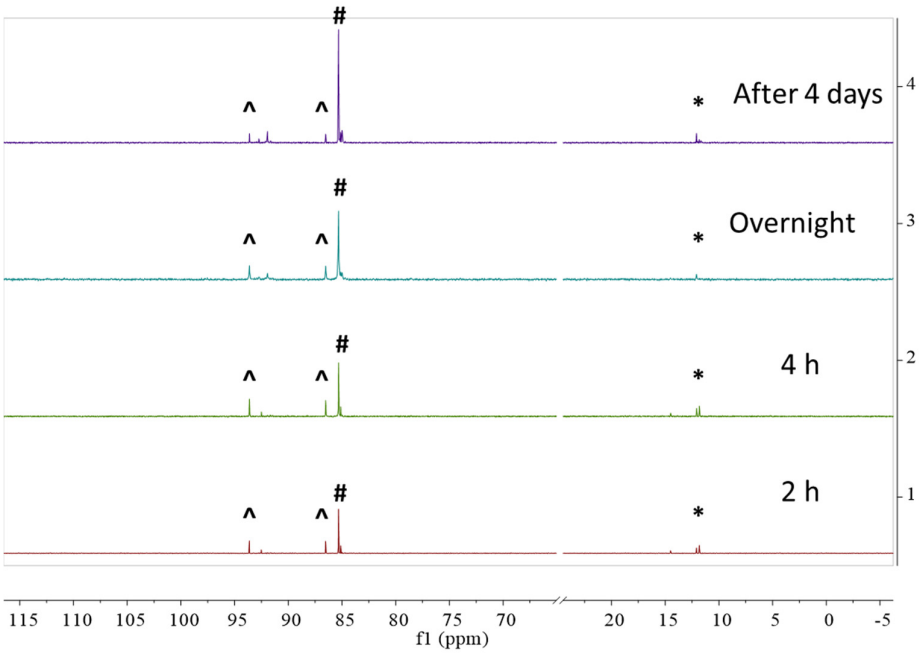

Figure S65: The stacked $^{31}P\{^{1}H\}$ NMR spectra of the reaction mixture between **^{iPr}PNNP** and 2 equiv $Fe_2(CO)_9$ in refluxing benzene measured at 298 K. The resonances with a * are assigned to free phosphine groups, with a ^ to complex **1** and with a # to complex **2**.

Additionally, we were interested if heating a solution of complex **1** in a solvent with a high boiling point would lead to thermal CO dissociation enabling synthesis of complexes with a diiron carbonyl core. To this end, a solution of **1** in anisole was heated to reflux. Broadened resonances in the $^{31}P\{^{1}H\}$ NMR spectrum (see Figure S66) were observed after 1.5 h and resonances assigned to free ligand were observed after refluxing overnight. The resulting reaction mixture is a suspension that contains insoluble precipitate, indicating that complex **1** and the iron carbonyl fragments are not stable under these reaction conditions.

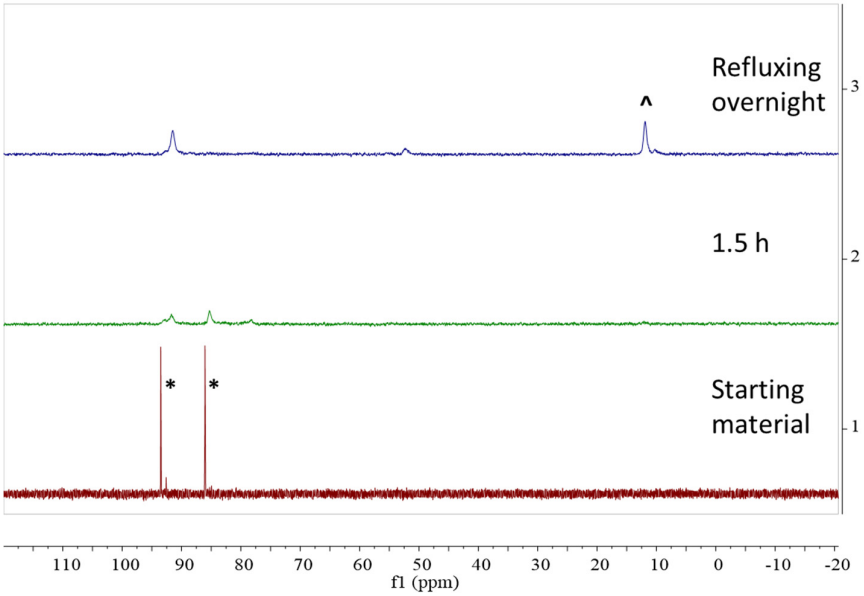

Figure S66: The stacked $^{31}P\{^{1}H\}$ NMR spectra of the refluxing reaction mixture of complex **1** in refluxing anisole measured at 298 K. The resonances with a * are assigned to complex **1** and with a ^ to **^{iPr}PNNP**.

Proposed mechanism of CO dissociation towards **4**

In contrast to **7**, complexes **1** and **2** are stable for prolonged times in both their solid- and solution-states at room temperature, and do not need to be stored with exclusion of light. As EPR and NMR analysis of the photolysis of **1** showed gradual conversion to paramagnetic **4** without any observable diamagnetic or paramagnetic intermediate, we are unable to conclude whether homolytic C–H bond cleavage precedes or follows CO loss. However, through the isolation and observed reactivity of complex **7**, it is clear that after H-atom abstraction CO dissociation is facile and occurs under significantly milder conditions than those required for the photochemical conversion of **1** to **4**. A plausible mechanism for the conversion of **7** to **4** could involve the interaction of the 17 VE Fe(I) center with a carbonyl ligand from the iron tetracarbonyl fragment under photochemical conditions through an associative mechanism. This would lead to a kinetically labile 19 VE Fe(I) species,[9] enabling facile dissociation of a carbonyl ligand. A second iteration of this process results in substitution of a carbonyl ligand for the naphthyridine nitrogen to give **4**.

Electrochemical characterization and HER

Complex **4**:

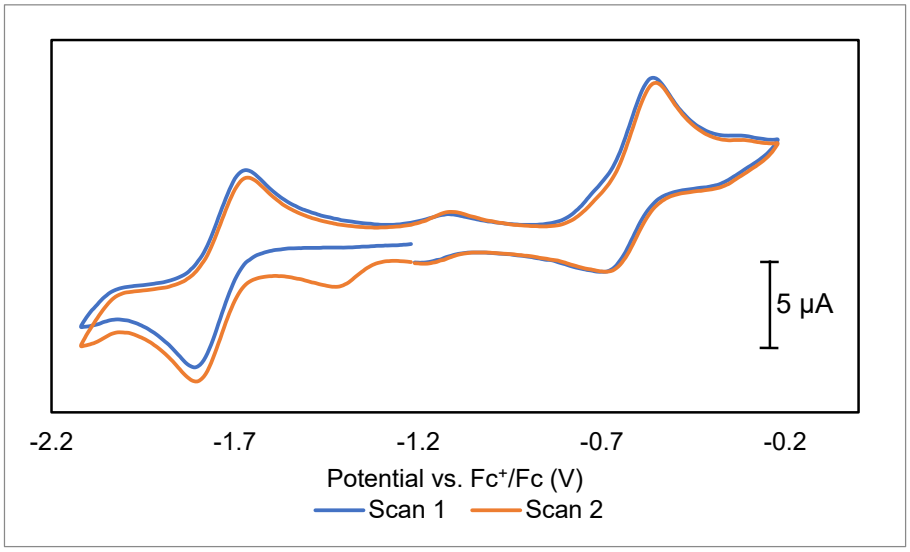

Figure S67: Cyclic voltammogram of 1 mM complex **4** in THF with 0.2 M [*n*-Bu_4N]PF_6 electrolyte using a glassy carbon working electrode, platinum wire counter electrode and silver wire pseudoreference electrode scanned in the negative direction (scan rate = 0.1 $V \cdot s^{-1}$). The voltammogram is internally referenced to the Fc^+/Fc couple. The reversible reduction is observed with $E_{1/2}$ = -1.74 V vs. Fc^+/Fc with a ΔE of 140 mV (quasi-reversible). The reversible oxidation is observed with $E_{1/2}$ = -0.68 V vs. Fc^+/Fc with a ΔE of 130 mV (quasi-reversible). The small redox couple observed at ca. -1.15 V vs Fc^+/Fc and irreversible reduction with a peak potential at ca. -1.4 V are attributed to small impurities or impurities formed during the CV scan.

Complex **3**:

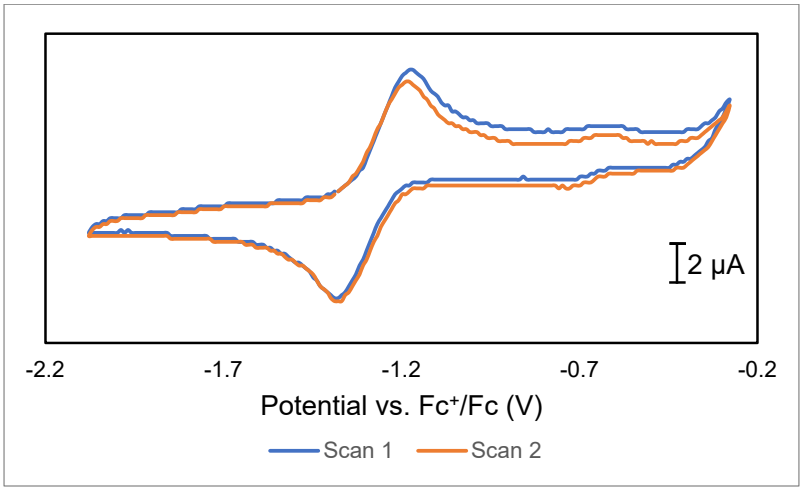

Figure S68: Cyclic voltammogram of 1 mM complex **3** in THF with 0.2 M [*n*-Bu_4N]PF_6 electrolyte using a glassy carbon working electrode, platinum wire counter electrode and silver wire pseudoreference electrode scanned in the positive direction (scan rate = 0.1 $V \cdot s^{-1}$). The voltammogram is internally referenced to the Fc^+/Fc couple. The voltammogram displays a quasi-reversible redox couple at $E_{1/2}$ = -1.28 V vs. Fc^+/Fc with a peak separation of ΔE = 200 mV.

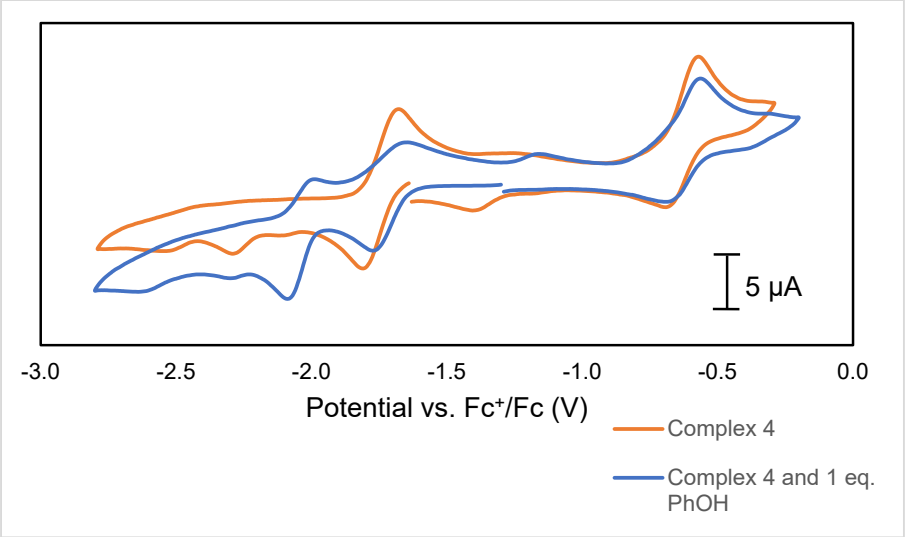

Figure S69: Cyclic voltammograms of 1 mM complex **4** with and without 1 equiv phenol in THF with 0.2 M [*n*-Bu_4N]PF_6 electrolyte using a glassy carbon working electrode, platinum wire counter electrode and silver wire pseudoreference electrode scanned in the negative direction (scan rate = 0.1 $V \cdot s^{-1}$). The voltammograms are internally referenced to the Fc^+/Fc couple. In the presence of phenol an additional irreversible reduction at -2.09 V vs. Fc^+/Fc is observed.

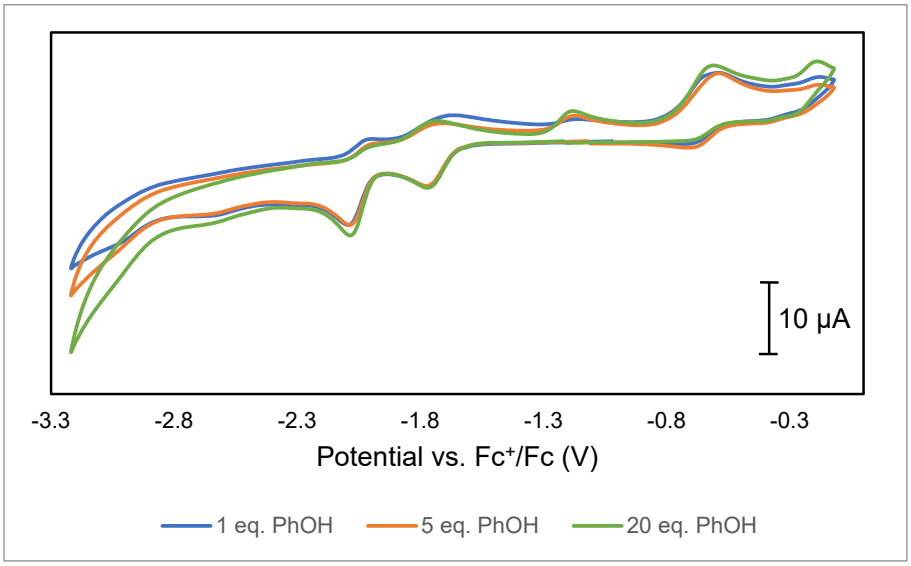

Figure S70: Cyclic voltammograms of 1 mM complex **4** with 1, 5 or 20 equiv of phenol in THF with 0.2 M [*n*-Bu_4N]PF_6 electrolyte using a glassy carbon working electrode, platinum wire counter electrode and silver wire pseudoreference electrode scanned in the negative direction (scan rate = 0.1 $V \cdot s^{-1}$). The voltammograms are internally referenced to the Fc^+/Fc couple. In the presence of phenol an additional irreversible reduction at -2.09 V vs. Fc^+/Fc is observed, but a cathodic current increase is not observed with the increasing equiv of phenol.

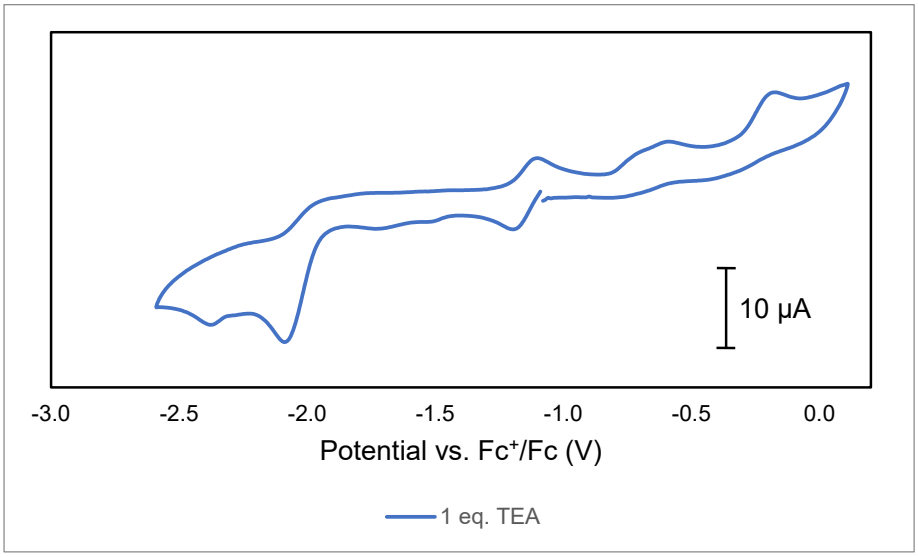

Figure S71: Cyclic voltammogram of 1 mM complex **4** and 1 equiv of TEA in THF with 0.2 M [*n*-Bu_4N]PF_6 electrolyte using a glassy carbon working electrode, platinum wire counter electrode and silver wire pseudoreference electrode scanned in the negative direction (scan rate = 0.1 $V \cdot s^{-1}$). The voltammogram is internally referenced to the Fc^+/Fc couple. The voltammogram displays a quasi-reversible redox couple at $E_{1/2}$ = -1.16 V vs. Fc^+/Fc with a peak separation of ΔE = 100 mV and irreversible reductions with potentials of -2.10 V and -2.38 V vs. Fc^+/Fc. Two irreversible oxidations with peak potentials of -0.61 V and -0.19 V vs. Fc^+/Fc are observed in the reverse scan.

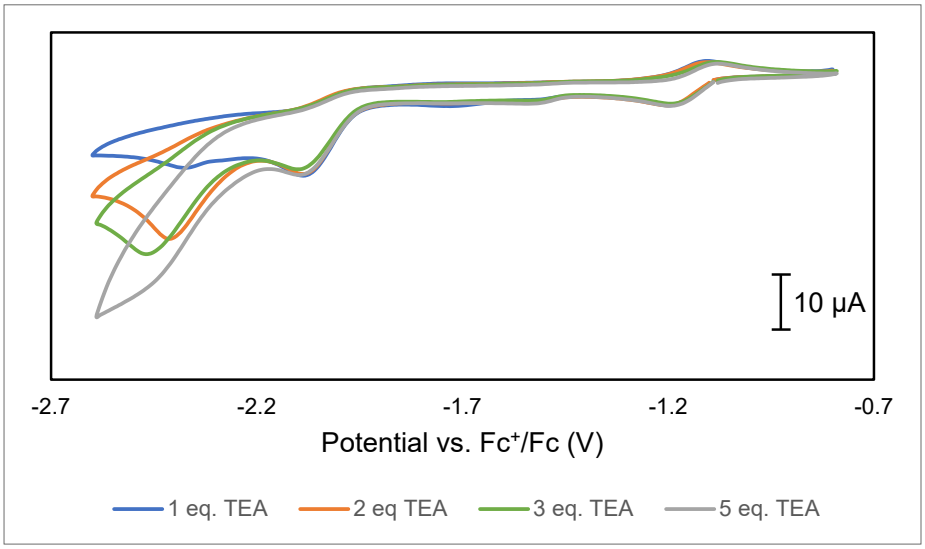

Figure S72: Cyclic voltammograms of 1 mM complex **4** with 1, 2, 3 or 5 equiv of TEA in THF with 0.2 M [*n*-Bu_4N]PF_6 electrolyte using a glassy carbon working electrode, platinum wire counter electrode and silver wire pseudoreference electrode scanned in the negative direction (scan rate = 0.1 $V \cdot s^{-1}$). The voltammograms are internally referenced to the Fc^+/Fc couple.

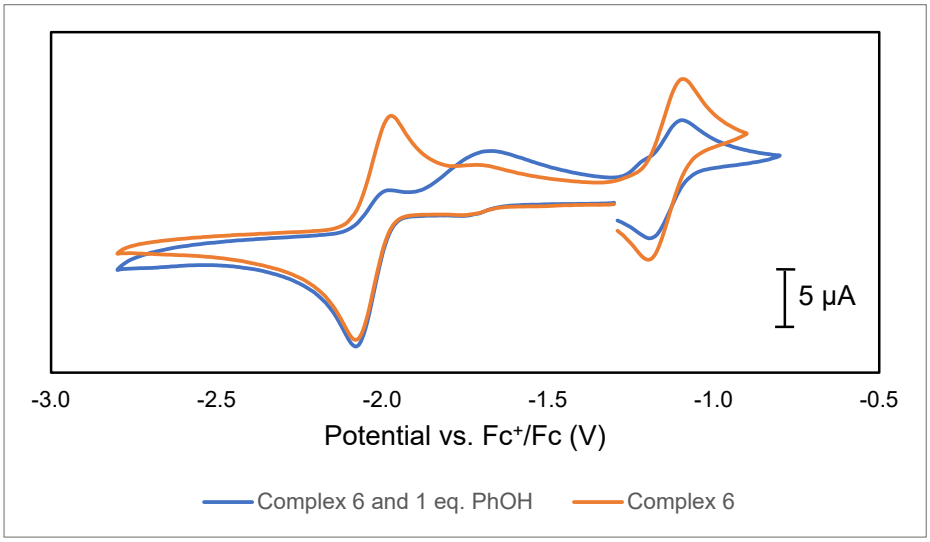

Figure S73: Cyclic voltammograms of 1 mM complex **6** with and without 1 equiv phenol in THF with 0.2 M [*n*-Bu_4N]PF_6 electrolyte using a glassy carbon working electrode, platinum wire counter electrode and silver wire pseudoreference electrode scanned in the negative direction. The voltammograms are internally referenced to the Fc^+/Fc couple.

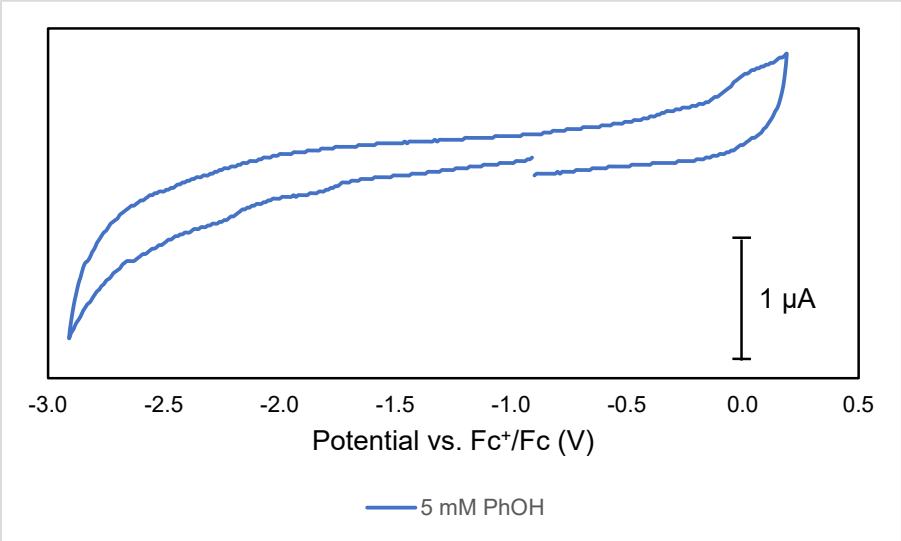

Figure S74: Cyclic voltammogram of 5 mM phenol (5 equiv) in THF with 0.2 M [*n*-Bu_4N]PF_6 electrolyte using a glassy carbon working electrode, platinum wire counter electrode and silver wire pseudoreference electrode scanned in the negative direction. The voltammogram is internally referenced to the Fc^+/Fc couple.

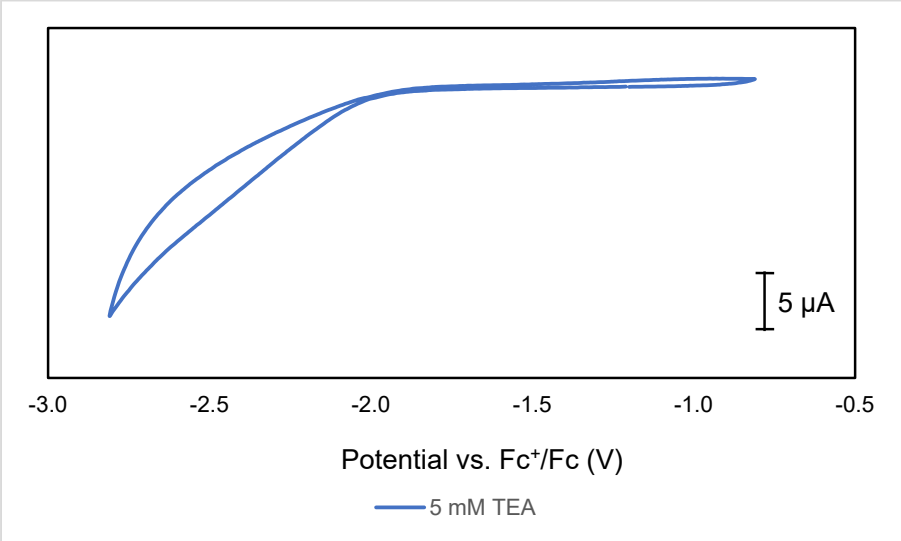

Figure S75: Cyclic voltammogram of 5 mM TEA (5 equiv) in THF with 0.2 M [*n*-Bu_4N]PF_6 electrolyte using a glassy carbon working electrode, platinum wire counter electrode and silver wire pseudoreference electrode scanned in the negative direction. The voltammogram is internally referenced to the Fc^+/Fc couple.

pK_a determination

Initial examination of the pK_a of complex **1** was conducted by reacting 1 equiv of deprotonated complex **3** with 1 equiv of 9-substituted fluorenes as C-H acid. NMR analysis of the reaction mixtures after an equilibrium has been established allows for a pK_a bracketing. A suitable acid/base can then be chosen to allow thermodynamic equilibrium, followed by pK_a determination. Addition of 9-phenyl-9*H*-fluorene (9-phenyl fluorene) (pK_a^{DMSO} = 17.9)[10] to complex **3** in THF did not give a reaction. However, the more acidic 9-(perfluorophenyl)-9*H*-fluorene (pK_a^{DMSO} = 14.7) [3] to complex **3** in THF resulted in a color change from dark red to brown. Analysis of the reaction mixture by ^{31}P NMR spectroscopy showed a near 1 : 1 mixture of both complex **1** and **3**. This ratio did not change over time showing that equilibrium had been achieved and that **1** and 9-(perfluorophenyl)-9*H*-fluorene have a similar pK_a^{THF}. Given that some acid/base reactions can take days or weeks to equilibrate, even with strong bases,[11] we also investigated the reaction of **1** with the potassium salt of the 9-(perfluorophenyl)-9*H*-fluorenide anion. This reaction also provided a similar near 1 : 1 mixture of **1** and **3** showing that thermodynamic equilibrium was established and that **1** and 9-(perfluorophenyl)-9*H*-fluorenene have a near equal pK_a in THF.

Since the pK_a^{THF} of this 9-(perfluorophenyl)-9*H*-fluorene has not been reported, we used the relative acidity scale, pK_α^{THF},[12] established by Morris to estimate a pK_a^{THF} for complex **1**. Using Morris' empirical relationship:

$$pK_a^{DMSO}(HA) = 0.85\ pK_\alpha^{THF}\ (HA) - 9.6$$

a pK_α^{THF} of 28 was obtained using the known pK_a^{DMSO} of 14.7 for 9-(perfluorophenyl)-9*H*-fluorenene.

Older work by Streitwieser and coworkers on the pK_a of C–H acids shows little difference between DMSO or THF.[13] The reason for this is that they used the pK_a of fluorene as the anchor point for their pK_{fi}^{THF} scale. However, Morris and coworkers reported that the absolute pK_a^{THF} values are likely to be quite different from the pK_{fi}^{THF} and pK_a DMSO values based on potentiometric experiments by Coetzee and coworkers, which showed that the pK_a^{THF} for picric acid is 11.6,[14]. This is more than 10 pKa units shifted compared to the pK_a^{DMSO} of 0.1 for picric acid[15] and provides an anchor point that is quite different from what was reported by Streitwieser and coworkers. This indicates that the intercept between the relation of pK_{fl}^{THF} and pK_a^{DMSO} needs to be adjusted to relate the pK_a^{THF} and pK_a^{DMSO}, which is why we used Morris' pK_α^{THF} relative acidity scale.

In aprotic nonpolar solvents like THF, ion pairs are not fully solvated and an ion pair dissociation equilibrium is present. The ion pair interaction and dissociation can influence the pK_a of an acid in THF solution.[16] We have not taken this into account given the uncertainty of the extent of ion pair association in **3**, the observation that full cation association/dissociation of fluorenides only affect the pK_a^{THF} by 0.1 unit, and because in our work we only use an estimate pK_a^{THF}.[17]

Synthesis of fluorenide salt

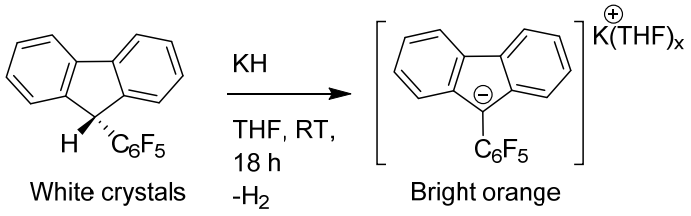

9-(perfluorophenyl)-9*H*-fluorene (35.0 mg, 105 µmol) in THF (1 mL) was treated dropwise with a suspension of KH (5.0 mg, 125 µmol) in THF (1.5 mL) under stirring. After a few minutes, the solution started becoming yellow. The mixture was stirred for 18 h, after which the resulting yellow/orange solution was filtrated and the volatiles were evaporated under a dynamic vacuum. The resulting film was scratched into a solid and washed with pentane (3 mL). The volatiles were evaporated under a dynamic vacuum yielding the potassium THF 9-(perfluorophenyl)-9*H*-fluorene salt as a yellow fluffy solid (47.8 mg, quantitative yield) with one molecule of THF, based on ^{1}H NMR analysis in THF-d_8*.

* The ^{1}H NMR spectrum was measured with a capillary of PPh_3 in C_6D_6 for the acid-base equilibrium experiments.

^{1}H NMR (400 MHz, THF-d_8, 298 K): δ 8.01 (d, $^{3}J_{H,H}$ = 7.7 Hz, 1H), 7.29 – 7.17 (m, 1H), *two other resonances are proposed to be found underneath the external PPh_3 resonances*.

^{13}C NMR (101 MHz, THF-h_8, 298 K): δ 136.0, 125.7, 121.7, 119.1, 116.3, 112.2.*

* A lower number of resonances than expected are observed. This could be due to the low intensity expected for quaternary carbon atoms, peak broadening caused by coupling of carbon with fluorine, and the use of a non-deuterated solvent.

^{19}F NMR (376 MHz, THF-d_8, 298 K): δ -138.1 – -140.2 (m), -164.7 – -167.5 (m), -170.2 – -170.5 (m).

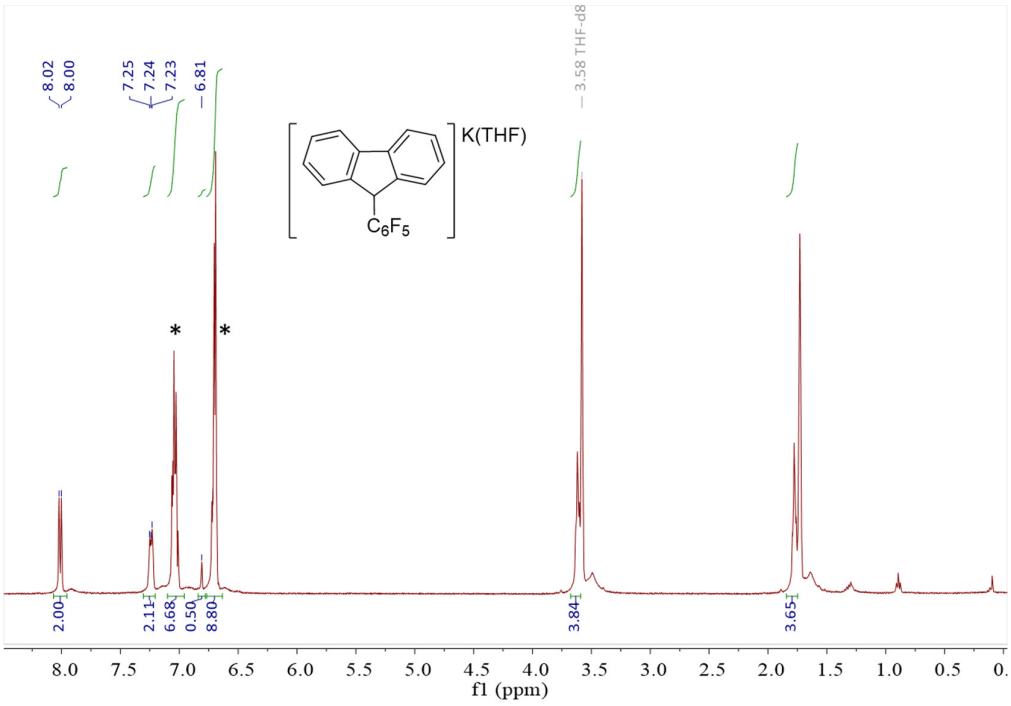

Figure S76: The ^{1}H NMR spectrum of the potassium THF 9-(perfluorophenyl)-9H-fluorenide salt in THF-d_8 at 298 K. The resonances with * are assigned to an external reference PPh_3 dissolved in C_6D_6 that was used for the acid-base equilibrium experiments.

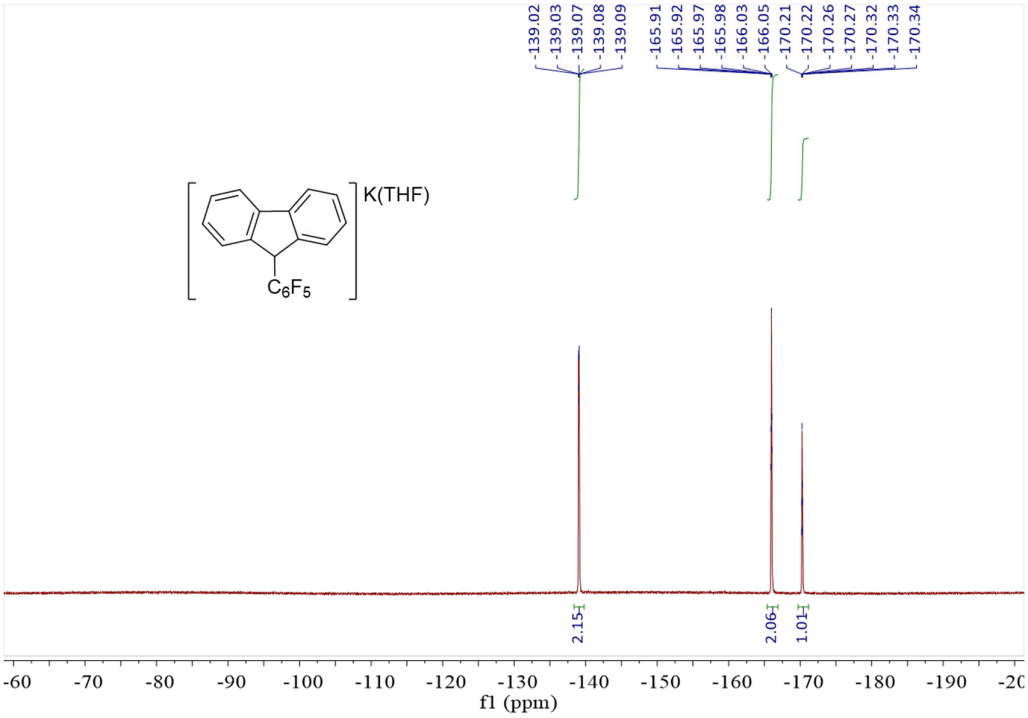

Figure S77: The ^{19}F NMR spectrum of the potassium THF 9-(perfluorophenyl)-9H-fluorenide salt in THF-d_8 at 298 K.

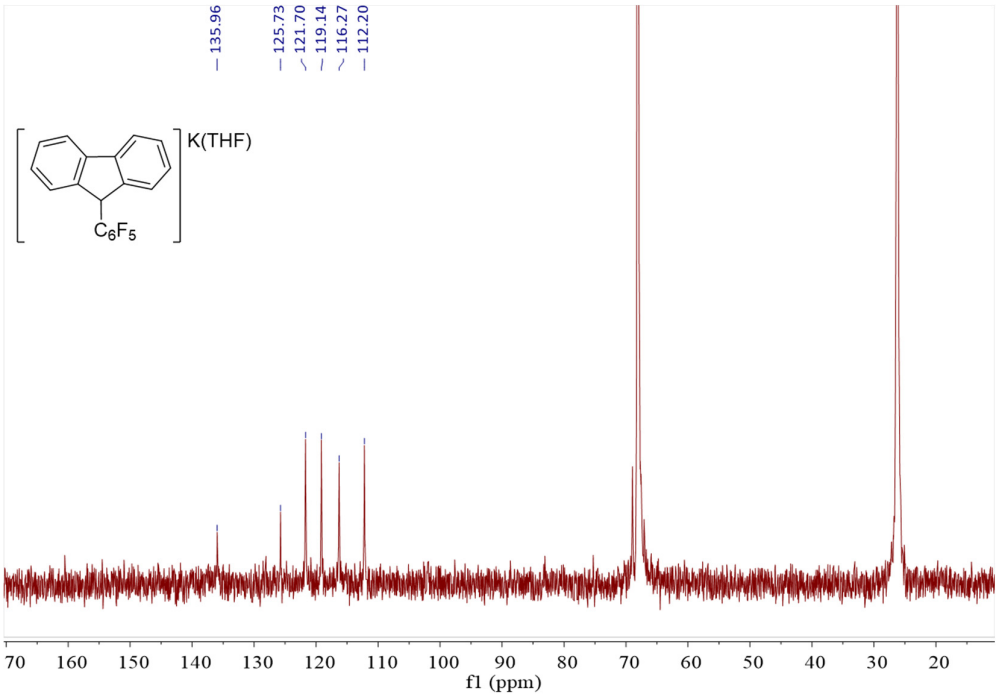

Figure S78: The ^{13}C NMR spectrum of the potassium THF 9-(perfluorophenyl)-9H-fluorenide salt in THF-h_8 at 298 K. Not all expected resonances are accounted for (see above).

NMR spectra acid-base equilibrium experiments:

Experimental details of reaction of 3 with 9-(perfluorophenyl)-9*H*-fluorene

A J. Young valved NMR tube was charged with **3** (10.6 mg, 12 µmol) and 9-(perfluorophenyl)-9*H*-fluorene (4.0 mg, 12 µmol) and THF-d_8 (0.60 mL). The mixture was monitored with ^{31}P NMR spectroscopy until no changes were observed, which was the case after 5 hours. Subsequently the mixture was analyzed by ^{1}H, ^{31}P and ^{19}F NMR spectroscopy.

Experimental details of reaction of 1 with the K salt of the 9-(perfluorophenyl)-9*H*-fluorenide anion*

A J. Young valved NMR tube was charged with **1** (6.2 mg, 12 µmol) and the potassium THF salt of 9-(perfluorophenyl)-9*H*-fluorene (8.4 mg, 12 µmol) and THF-d_8 (0.60 mL). The mixture was monitored with ^{31}P NMR spectroscopy until no changes were observed, which was the case after 5 hours. Subsequently the mixture was analyzed by ^{1}H, ^{31}P and ^{19}F NMR spectroscopy, which all showed near 1:1 mixtures; see S79-S84.

* due to minor impurities (~5%) visible in the ^{1}H NMR of the K salt of the 9-(perfluorophenyl)-9*H*-fluorenide anion we deem the ratios obtained in the experiment involving **3** and 9-(perfluorophenyl)-9*H*-fluorene more representative.

The ^{1}H, ^{19}F and ^{31}P NMR spectra were collected using a five second relaxation delay between different scans. Sharp resonances were observed for the different components in the ^{1}H and ^{19}F NMR spectra. Broad resonances were observed for complexes **1** and **3** in the ^{31}P NMR spectra due to the species being in equilibrium with each other. The resonances observed for 9-(perfluorophenyl)-9*H*-fluorene in the ^{1}H NMR spectra in the acid-base equilibrium experiments are consistent with literature.[18] Its ^{19}F NMR spectrum in THF-d_8 has not been reported yet and is shown in figure S79 as a reference for the ^{19}F NMR spectra of these experiments.

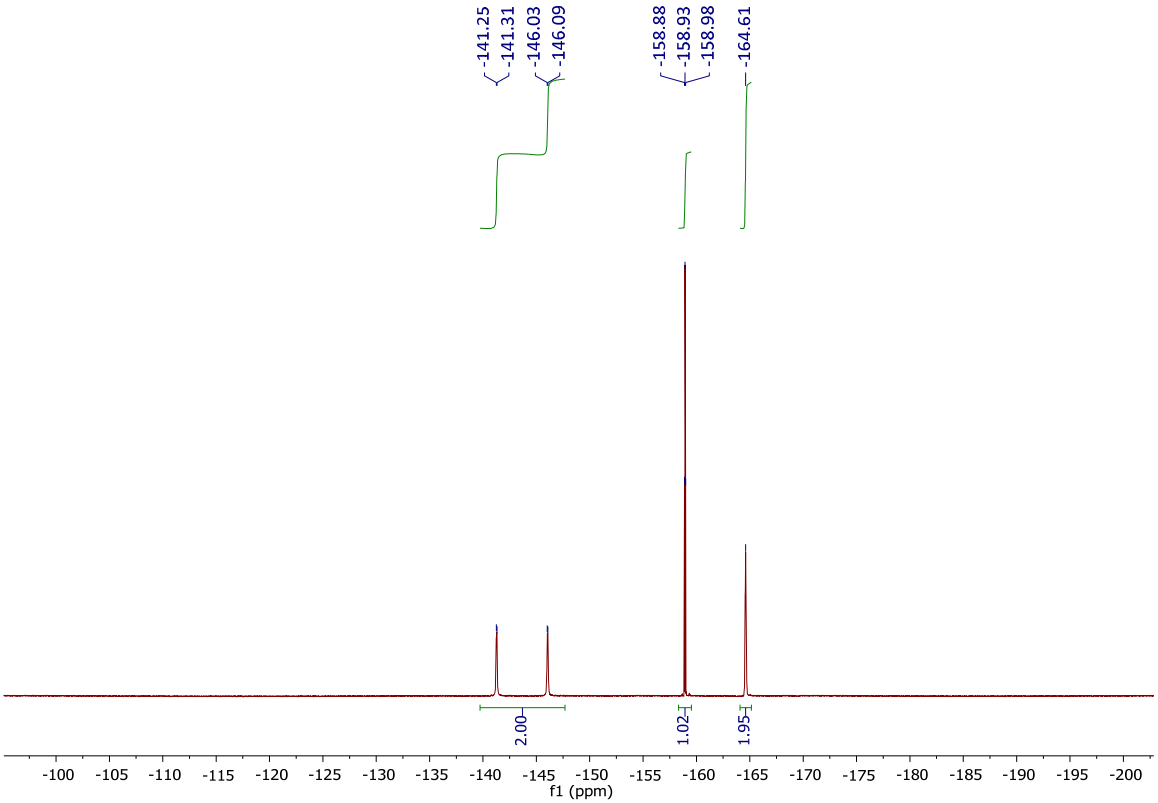

Figure S79: The ^{19}F NMR spectrum of *9-(perfluorophenyl)-9H-fluorene* in THF-d_8 at 298 K.

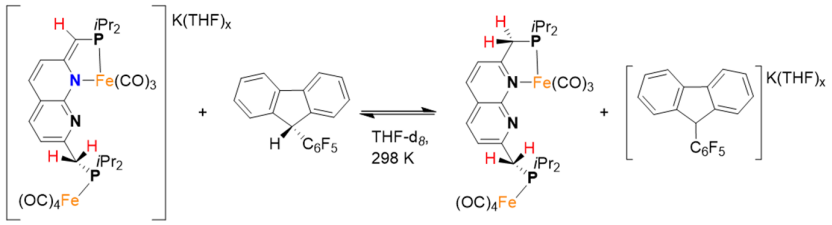

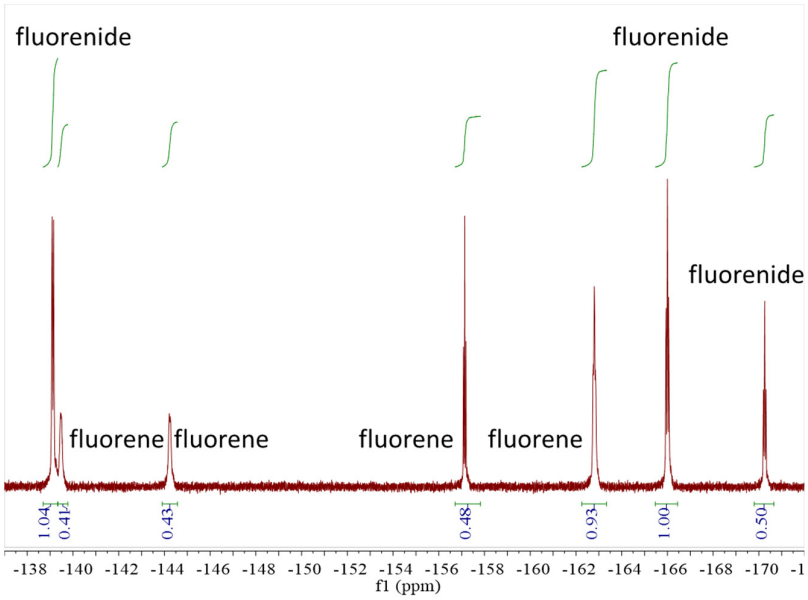

Figure S80: The ^{19}F NMR spectrum of acid-base equilibrium experiment 1 in THF-d_8 at 298 K.

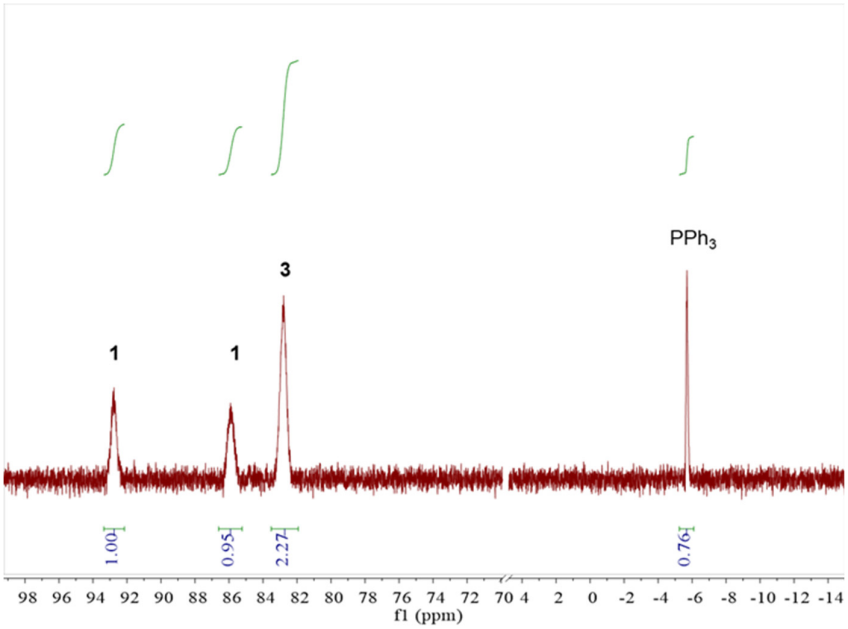

Figure S81: The $^{31}P\{^1H\}$ NMR spectrum of acid-base equilibrium experiment 1 in THF-d_8 at 298 K. PPh_3 in C_6D_6 was added as an external reference in a capillary.

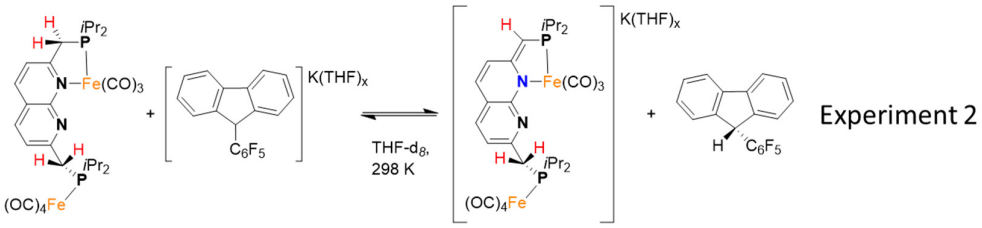

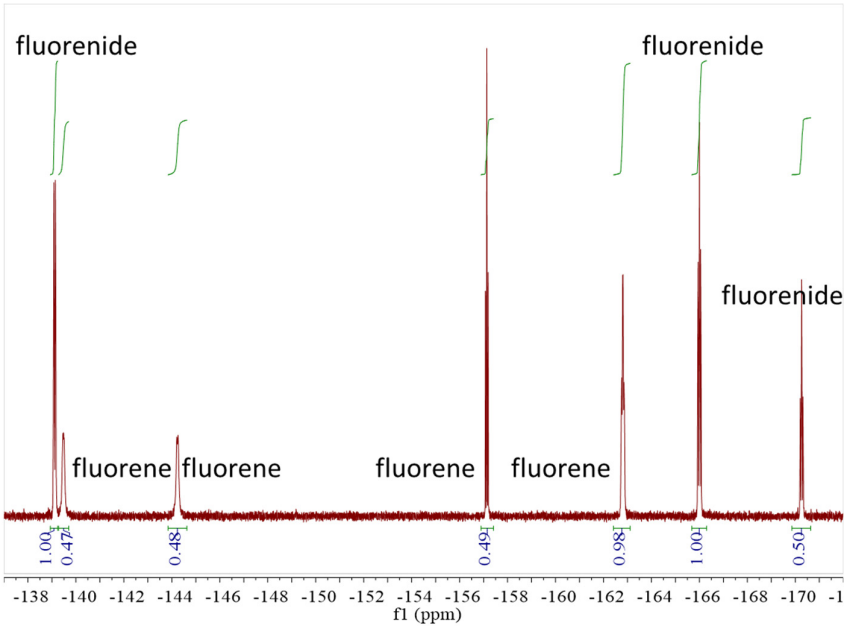

Figure S82: The ^{19}F NMR spectrum of acid-base equilibrium experiment 2 in THF-d_8 at 298 K.

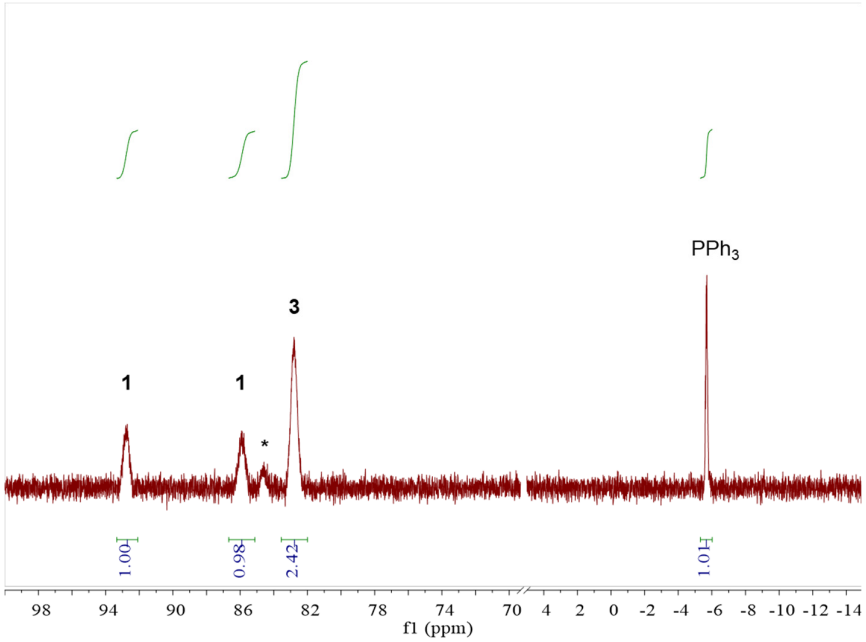

Figure S83: The $^{31}P\{^1H\}$ NMR spectrum of acid-base equilibrium experiment 2 in THF-d_8 at 298 K. PPh_3 was added as an external reference in a capillary. * is assigned to the impurity complex **2** in the starting material.

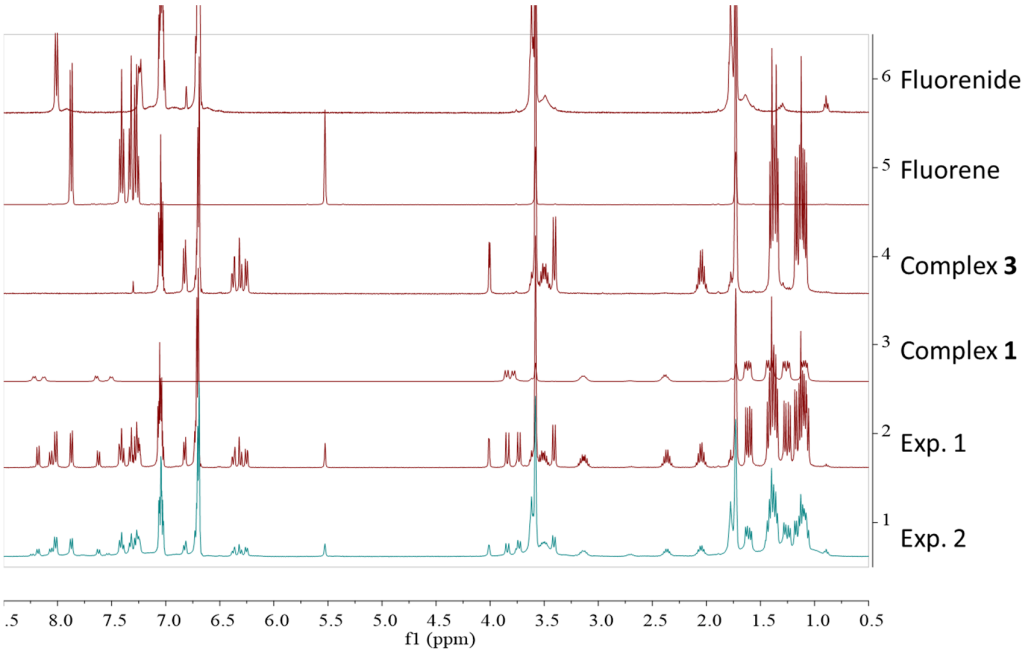

Figure S84: The stacked ^{1}H NMR spectra of acid-base equilibrium experiments 1 and 2 including the reference compounds in THF-d_8 at 298 K.

Headspace analysis by GC

Photolysis of complex **1**/**2** and paramagnetic complex **7** result in the loss of CO ligands. Additionally, based on the proposed structure of complex **4**, one H-atom (0.5 equiv of H_2) is lost during photolysis of complex **1**. The hypothesis that CO and H_2 gas are formed in these photolysis experiments was tested by headspace analysis of a J-Young valved NMR tube by gas chromatography (GC). Two different experiments were performed and analyzed by GC. In the first experiment, photolysis of complex **1** was performed in benzene solution until **1** was no longer detected by NMR spectroscopy. In the second experiment, **1** was reacted with 1 equiv TBP in THF solution and the brown reaction mixture was immediately placed in a J-Young valved NMR tube and closed. This solution was kept in light for four days. The NMR tubes were then sequentially connected to the GC set-up with an adaptor connected to the GC carrier (grade 5 nitrogen) gas inlet, see figure S85. A gas sample was injected and measured every four minutes with all carbon-based components by a FID. Hydrogen gas was detected using a TCD on four different channels resulting in a measurement every minute. Since the CO/H_2 analytes were not calibrated and the analysis is diffusion limited, only qualitative analysis of the analytes is performed.

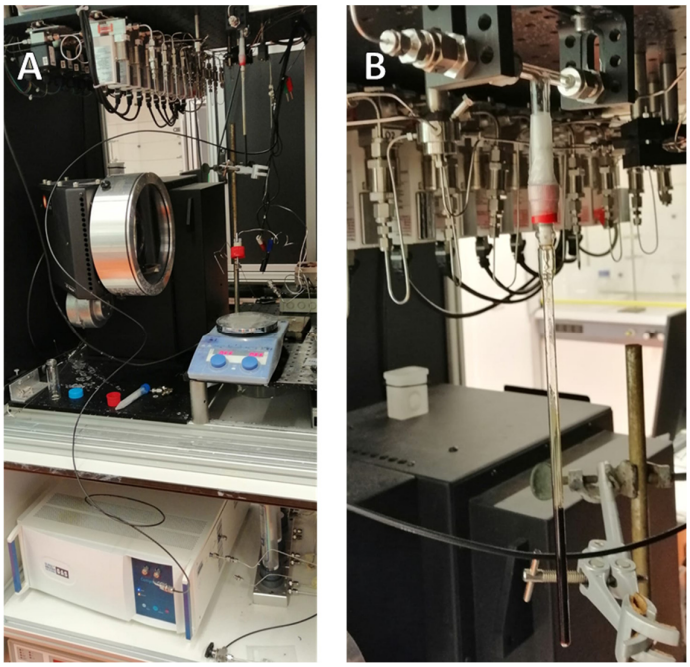

Figure S85: Headspace analysis by GC. **(A)** set-up showing both the GC (below) and the gas inlets/outlets (up). **(B)** NMR sample connected to the carrier gas inlet with an adaptor.

First experiment: Photolysis of **1**

After photolysis of **1**, the closed J-Young valved NMR tube was placed in the adaptor of the GC set-up. The set-up was flushed for approx. 30 min and the gases were analyzed every four minutes, which are displayed in Table S1. After measuring for 25 minutes, the NMR tube was opened, allowing diffusion of the headspace out of the NMR tube. Both CO (channel 3, 2nd column in the table) and H_2 (channels 1-4, 3rd column in the table) were detected after opening the NMR tube. A higher signal for CO than for H_2 was detected, which after every subsequent measurement decreased in intensity. Based on this result, it was concluded that both CO and H_2 gas were present in the headspace.

Table S1: Results headspace GC analysis after photolysis of complex **1**.			
No.	Area pA*min FID_Ch_3 CO	Area mV*min TCD_Ch_1-4 Hydrogen channel 1-4	Inject Time
1	n.a.	0.182	12:07
2	n.a.	0.092	12:11
3	0.004	0.000	12:15
4	n.a.	0.002	12:20
5	n.a.	0.001	12:24
6	n.a.	0.001	12:28
7	n.a.	0.001	12:32
8	2.329	0.005	12:36
9	27.958	0.005	12:41
10	25.586	0.004	12:45
11	23.574	0.003	12:49
12	21.361	0.002	12:53
13	19.673	0.002	12:57
14	18.476	0.001	13:01
15	16.918	0.001	13:06
16	15.826	0.000	13:10
17	14.659	0.000	13:14
18	13.676	0.000	13:18
19	12.665	0.000	13:22
20	11.592	0.000	13:27
21	10.881	0.000	13:31
22	10.147	0.000	13:35
23	9.328	0.000	13:39
24	8.700	0.000	13:43
25	8.130	0.000	13:48
26	7.464	0.000	13:52
27	6.932	0.000	13:56
28	6.520	0.000	14:00
29	5.905	0.000	14:04
30	5.504	0.000	14:09
31	4.478	0.000	14:13

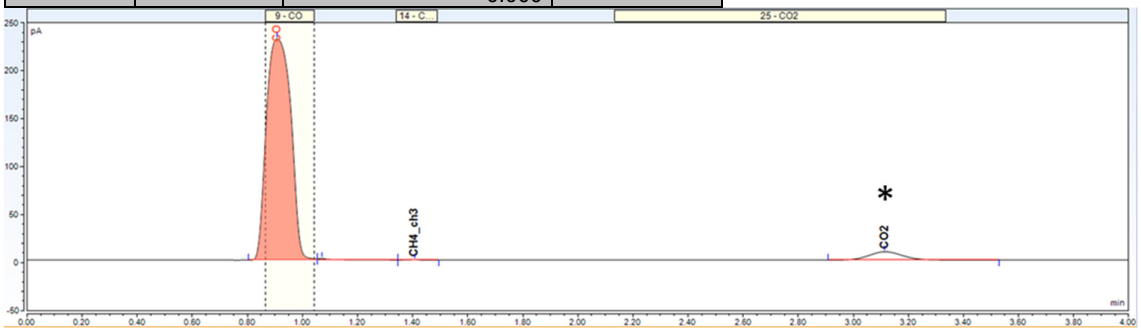

Figure S86: Chromatogram of the headspace analysis of GC experiment 1. This chromatogram was recorded after opening the NMR tube and displays a signal corresponding to CO gas in pink after 0.9 min. * Some residual CO_2 was present in the system which most likely originates from the set-up's previous measurements.

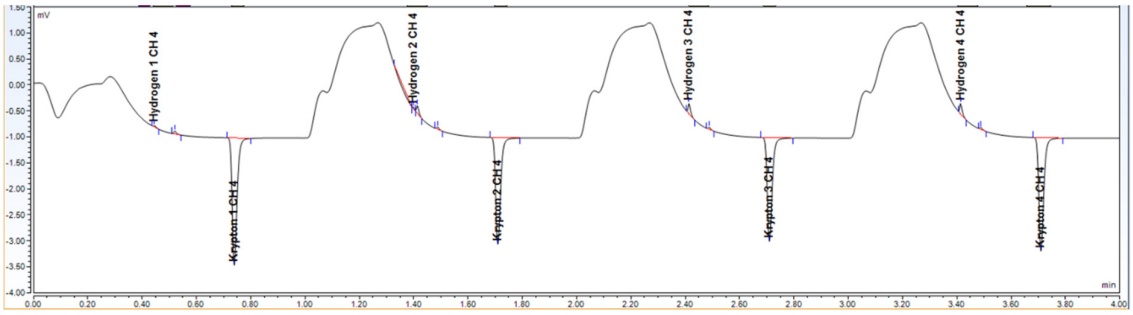

Figure S86-2: Chromatogram of the headspace analysis of GC experiment 1. This chromatogram was recorded after opening the NMR tube and displays four different chromatograms (one every minute). The signals at 0.40, 1.40, 2.40 and 3.40 min are assigned to H_2 gas.

Second experiment: Hydrogen atom transfer from **1** to TBP

After HAT from **1** to TBP, the stored NMR tube containing the reaction mixture was placed in the adaptor of the GC set-up. The set-up was flushed with nitrogen allowing removal of the products from GC experiment 1. Then, the measurements were started, and a sample was injected every four minutes. After approx. 15 min, the NMR tube was opened, allowing diffusion of the headspace out of the NMR tube. CO gas was detected after the NMR tube was opened. A signal corresponding to H_2 was not detected during the measurement for this experiment. The measurements were continued for approx. 2 h, after which most of the signal intensity corresponding to CO gas had decreased, see Table S2.

Table S2: Headspace GC results after hydrogen atom abstraction from complex **1**.

No.	Area pA*min FID_Ch_3 CO	Inject Time
1	4.808	14:18
2	n.a.	14:22
3	0.021	14:26
4	0.013	14:30
5	0.091	14:34
6	4.294	14:39
7	4.302	14:43
8	3.911	14:47
9	3.483	14:51
10	3.128	14:55
11	2.776	15:00
12	2.458	15:04
13	2.158	15:08
14	1.965	15:12
15	1.744	15:16
16	1.562	15:20
17	1.435	15:25
18	1.293	15:29
19	1.124	15:33
20	1.027	15:37
21	0.943	15:41

22	0.831	15:46
23	0.767	15:50
24	0.707	15:54
25	0.640	15:58
26	0.593	16:02
27	0.555	16:07
28	0.526	16:11
29	0.465	16:15
30	0.435	16:19
31	0.404	16:23

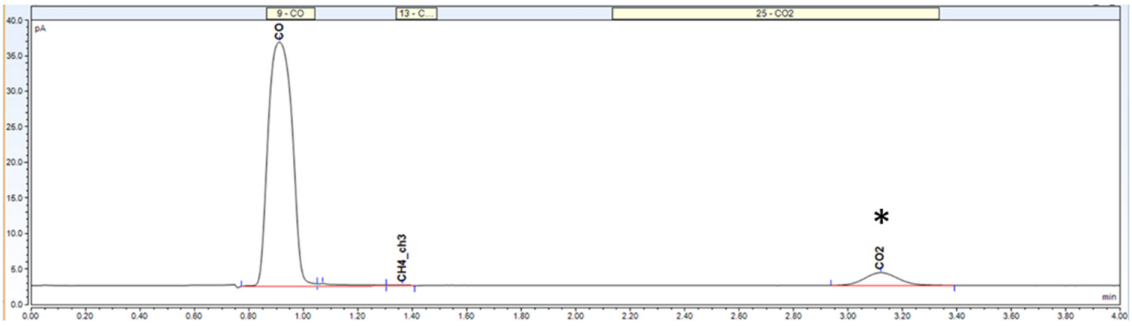

Figure S87: Chromatogram of the headspace analysis of GC experiment 1. This chromatogram was recorded after opening the NMR tube and displays a signal corresponding to CO gas after 0.9 min. * Some residual CO_2 was present in the system which most likely originates from the set-up's previous measurements.

Crystallographic details

X-ray crystal structure determination of complex 1 (l1083a)

$C_{29}H_{36}Fe_2N_2O_7P_2$, Fw = 698.24, dark red block, 0.39 × 0.18 × 0.12 mm^3, triclinic, P $\overline{1}$ (no. 2), a = 9.17932(18), b = 13.9790(3), c = 14.4063(3) Å, α = 113.213(1), β = 106.029(1), γ = 94.152(1) °, V = 1598.15(6) Å^3, Z = 2, D_x = 1.451 g/cm^3, μ = 1.05 mm^{-1}. The diffraction experiment was performed on a Bruker Kappa ApexII diffractometer with sealed tube and Triumph monochromator (λ = 0.71073 Å) at a temperature of 150(2) K up to a resolution of $(\sin\theta/\lambda)_{max}$ = 0.81 Å^{-1}. Intensity integration was performed with the Eval15 software.[19] A multi-scan absorption correction and scaling was performed with SADABS (correction range 0.65-0.75).[20] A total of 56990 reflections was measured, 14069 reflections were unique (R_{int} = 0.024), 12232 reflections were observed [I>2σ(I)]. The structure was solved with Patterson superposition methods using SHELXT.[21] Structure refinement was performed with SHELXL-2018 on F^2 of all reflections.[22] Non-hydrogen atoms were refined freely with anisotropic displacement parameters. All hydrogen atoms were located in difference Fourier maps and refined with a riding model. 387 Parameters were refined with no restraints. R1/wR2 [I > 2σ(I)]: 0.0240 / 0.0654. R1/wR2 [all refl.]: 0.0298 / 0.0680. S = 1.038. Residual electron density between -0.50 and 0.49 e/Å^3. Geometry calculations and checking for higher symmetry was performed with the PLATON program.[23]

X-ray crystal structure determination of complex 3 (l1118a)

$C_{37}H_{51}Fe_2KN_2O_9P_2$, Fw = 880.53, red plate, 0.23 × 0.13 × 0.03 mm^3, triclinic, P $\overline{1}$ (no. 2), a = 8.9778(5), b = 14.3123(7), c = 17.4153(10) Å, α = 80.797(4), β = 83.740(3), γ = 76.749(2) °, V = 2144.0(2) Å^3, Z = 2, D_x = 1.364 g/cm^3, μ = 0.90 mm^{-1}. The diffraction experiment was performed on a Bruker Kappa ApexII diffractometer with sealed tube and Triumph monochromator (λ = 0.71073 Å) at a temperature of 150(2) K up to a resolution of $(\sin\theta/\lambda)_{max}$ = 0.61 Å^{-1}. The intensity data were weak and the integration was performed with the Eval15 software.[19] A multi-scan absorption correction and scaling was performed with SADABS (correction range 0.65-0.75).[20] A total of 41157 reflections was measured, 7997 reflections were unique (R_{int} = 0.116), 4513 reflections were observed [I>2σ(I)]. The structure was solved with Patterson superposition methods using SHELXT.[21] Structure refinement was performed with SHELXL-2018 on F^2 of all reflections.[22] Non-hydrogen atoms were refined freely with anisotropic displacement parameters. Hydrogen atoms were introduced in calculated positions and refined with a riding model. 486 Parameters were refined with no restraints. R1/wR2 [I > 2σ(I)]: 0.0618 / 0.1337. R1/wR2 [all refl.]: 0.1328 / 0.1581. S = 1.036. Residual electron density between -0.41 and 0.84 e/Å^3. Geometry calculations and checking for higher symmetry was performed with the PLATON program.[23]

X-ray crystal structure determination of complex 5 (l1177a)

$C_{31}H_{43}Fe_2KN_2O_6P_2$, Fw = 752.41, dark red needle, 0.47 × 0.11 × 0.07 mm^3, monoclinic, C2/c (no. 15), a = 24.9530(8), b = 10.2928(4), c = 28.5081(9) Å, β = 106.275(1) °, V = 7028.5(4) Å^3, Z = 8, D_x = 1.422 g/cm^3, μ = 1.08 mm^{-1}. The diffraction experiment was performed on a Bruker Kappa ApexII

diffractometer with sealed tube and Triumph monochromator (λ = 0.71073 Å) at a temperature of 150(2) K up to a resolution of $(\sin\theta/\lambda)_{max}$ = 0.65 Å^{-1}. A split-mosaic model was used for the intensity integration with the Eval15 software[19] A numerical absorption correction and scaling was performed with SADABS (correction range 0.68-1.00).[20] A total of 62898 reflections was measured, 8081 reflections were unique (R_{int} = 0.053), 6498 reflections were observed [I>2σ(I)]. The structure was solved with Patterson superposition methods using SHELXT.[21] Structure refinement was performed with SHELXL-2018 on F^2 of all reflections.[22] Non-hydrogen atoms were refined freely with anisotropic displacement parameters. All hydrogen atoms were located in difference Fourier maps and refined with a riding model. The hydrogen positions at C1 and C10 were refined with a disorder model (sp^2/sp^3 hybridization). 406 Parameters were refined with no restraints. R1/wR2 [I > 2σ(I)]: 0.0340 / 0.0777. R1/wR2 [all refl.]: 0.0481 / 0.0827. S = 1.049. Residual electron density between -0.32 and 0.52 e/Å^3. Geometry calculations and checking for higher symmetry was performed with the PLATON program.[23]

X-ray crystal structure determination of complex 6 (l1199a)

$C_{27}H_{36}Fe_2N_2O_5P_2 \cdot 1.5(C_6H_6)$, Fw = 759.38, brown needle, 0.63 × 0.09 × 0.02 mm^3, monoclinic, $P2_1/c$ (no. 14), a = 9.2797(4), b = 23.4414(12), c = 16.6539(8) Å, β = 95.972(2) °, V = 3603.1(3) Å^3, Z = 4, D_x = 1.400 g/cm^3, μ = 0.94 mm^{-1}. The diffraction experiment was performed on a Bruker Kappa ApexII diffractometer with sealed tube and Triumph monochromator (λ = 0.71073 Å) at a temperature of 150(2) K up to a resolution of $(\sin\theta/\lambda)_{max}$ = 0.65 Å^{-1}. A split-mosaic model was used for the intensity integration with the Eval15 software.[19] The presence of additional small crystal fragments was ignored during the integration. A numerical absorption correction and scaling was performed with SADABS (correction range 0.62-1.00).[20] A total of 66913 reflections was measured, 8268 reflections were unique (R_{int} = 0.109), 5542 reflections were observed [I>2σ(I)]. The structure was solved with Patterson superposition methods using SHELXT.[21] Structure refinement was performed with SHELXL-2018 on F^2 of all reflections.[22] Non-hydrogen atoms were refined freely with anisotropic displacement parameters. One isopropyl group was refined with a disorder model. The hydrogen atoms of the ordered part were located in difference Fourier maps. The hydrogen atoms in the disordered part were included in calculated positions. All hydrogen atoms were refined with a riding model. 437 Parameters were refined with 91 restraints (distances, angles and displacement parameters in the disordered group). R1/wR2 [I > 2σ(I)]: 0.0494 / 0.0961. R1/wR2 [all refl.]: 0.0927 / 0.1087. S = 1.089. Residual electron density between -0.46 and 0.62 e/Å^3. Geometry calculations and checking for higher symmetry was performed with the PLATON program.[23]

CCDC 2110888-2110891 contain the supplementary crystallographic data for this paper. These data can be obtained free of charge from The Cambridge Crystallographic Data Centre via www.ccdc.cam.ac.uk/data_request/cif.

Structural characteristics

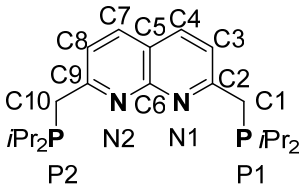

Atom labelling in $^{i\text{Pr}}$PNNP for $^{i\text{Pr}}$PNNP* methine linker is labelled as C1

Table S3: Selected distances and angles of compounds **1**, **3**, **5** and **6** in Å and °, respectively.

Atoms	**1**	**3**	**5**[a]	**6**
Fe–Fe2	-	-	2.5585(4)	2.5538(7)
Fe1–P1	2.2193(2)	2.2362(15)	2.1918(6)	2.1986(10)
Fe2–P2	2.2599(2)	2.2752(16)	2.1888(6)	2.1795(11)
Fe1–-N1	2.0796(7)	2.071(4)	2.0636(16)	2.052(3)
Fe2–N2	-	-	2.0554(17)	2.034(3)
Fe1–C23	1.7801(8)	1.766(6)	1.930(2)	1.949(3)
Fe2–C23	-	-	1.9494(19)	1.956(3)
Fe1–C24	1.7918(9)	1.792(6)	1.727(2)	1.729(4)
Fe1–C25	1.7409(9)	1.730(6)	1.786(2)	1.802(4)
Fe2–C26	1.7823(9)	1.795(7)	1.734(2)	1.732(4)
Fe2–C27	1.7934(9)	1.786(7)	1.792(2)	1.801(4)
P1–C1	1.8305(9)	1.781(5)	1.782(2)	1.837(4)
P2–C10	1.8559(8)	1.827(5)	1.800(2)	1.824(3)
C1–C2	1.4950(11)	1.364(7)	1.405(3)	1.500(5)
C9–C10	1.5035(11)	1.514(6)	1.455(3)	1.495(5)
P1–C1–C2	111.15(5)	115.6(4)	113.81(16)	108.0(2)
P2–C10–C9	114.73(5)	117.5(4)	111.86(17)	107.6(2)

[a] Structure disordered at C1/C10.

Table S4: Selected distances of compounds **1**, **3**, **5** and **6** in Å.				
Atoms	**1**	**3**	**5**[a]	**6**
C1–C2	1.4950(11)	1.364(7)	1.405(3)	1.500(5)
C2–C3	1.4144(11)	1.447(7)	1.422(3)	1.392(5)
C3–C4	1.3621(12)	1.341(7)	1.351(3)	1.363(5)
C4–C5	1.4119(12)	1.432(7)	1.414(3)	1.405(5)
C5–C6	1.4183(11)	1.447(7)	1.439(3)	1.418(5)
N1–C2	1.3401(10)	1.401(6)	1.383(3)	1.352(4)
N1–C6	1.3896(10)	1.382(6)	1.358(3)	1.372(4)
C5–C7	1.4120(12)	1.394(7)	1.397(3)	1.401(5)
C7–C8	1.3678(12)	1.379(7)	1.367(3)	1.352(5)
C8–C9	1.4142(11)	1.405(8)	1.401(3)	1.403(5)
C9–C10	1.5035(11)	1.514(6)	1.455(3)	1.495(5)
N2–C9	1.3257(10)	1.348(6)	1.376(3)	1.357(4)
N2–C6	1.3518(10)	1.349(6)	1.363(3)	1.376(4)
[a] Structure disordered at C1/C10.				

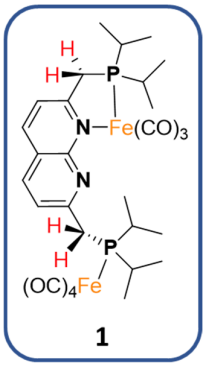

1

Single crystals of **1** suitable for X-ray diffraction were grown by vapor diffusion of hexane into a concentrated benzene solution of **1**. The solid-state structure of **1** contains the ^{iPr}**PNNP** ligand bound to an iron tricarbonyl fragment as well as an iron tetracarbonyl fragment as described in the main text. The iron tetracarbonyl fragment displays a slightly distorted trigonal bipyramidal geometry (P2–Fe2–C27 = 174.27(3)°) with the phosphine coordinated on an axial position. The Fe2–P2 bond length is 2.2599(2) Å and the Fe2–C bonds have similar lengths (from 1.7823(9) Å to 1.7984(10) Å), which is comparable to reported $PR_3Fe(CO)_4$ (R = alkyl) complexes.[24] The iron tricarbonyl fragment is bound in a bidentate fashion by a phosphine and the naphthyridine nitrogen. The geometry around iron Fe1 is distorted trigonal bipyramidal with phosphorus on an equatorial and nitrogen on an axial position. This arrangement has been found in other iron(0) tricarbonyl complexes bearing a chelating ligand.[25] The Fe–C bond lengths of the equatorial carbonyl ligands (1.7801(8) and 1.7918(9) Å) are longer than the axial Fe–C25 bond length (1.7409(9) Å).

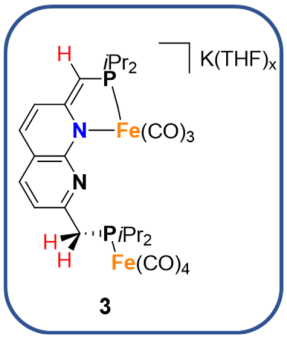

3

Single crystals of **3** suitable for X-ray diffraction were grown by slow evaporation of a THF solution of **3**. Anionic complex **3** forms a one-dimensional coordination polymer that runs in the crystallographic a-direction. The complex is linked to potassium in a chain through carbonyl ligands as described in the main text. These findings in the crystal structure are consistent with the IR results which show that the carbonyl bands are observed at lower wavenumbers compared to **1** (see S35)[26] and the carbonyl bands that are significantly broader compared to **1**. This could be due to the presence of various binding modes involving the potassium cation with carbonyl ligands that exist in non-crystalline material.

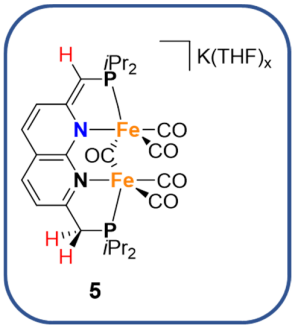

5

Long needles of **5** suitable for X-ray diffraction were grown by slow evaporation of a concentrated THF solution. The diironpentacarbonyl core in anionic complex **5** contains four terminal carbonyl ligands. Additionally, a bridging carbonyl ligand is present bonded perpendicular to the naphthyridine plane. The bridging carbonyl ligand is closer to Fe1 (1.930(2) Å) than to Fe2 (1.9494(19) Å) and these bond lengths are comparable to other diiron carbonyl complexes with a bridging carbonyl ligand.[27] The terminal axial and equatorial carbonyl ligands on both inequivalent iron centers are located within and perpendicular to the naphthyridine plane, respectively. The terminal carbonyl ligands in **5** are coordinated to potassium ions through their oxygen atoms (see figure S89 for packing). Therefore, the structure forms a one-dimensional coordination chain in the b-direction, which is the needle direction of the macroscopic crystal. The hydrogen atoms at the methine/methylene linker (C1/C10) of the ^{iPr}**PNNP*** ligand in **5** were refined with a disorder model in the ratio of 2/3 : 1/3, respectively. We assume that the disorder not only affects the atoms C1 and C10 but indicates an orientational disorder about the central naphthyridine bond. Both orientations of the molecule are then arranged on top of each other (''whole molecule disorder''), and the derived C–C bond lengths of the ligand are averages of both orientations. Therefore, assignment of the ''protonated half'' or ''deprotonated half'' of the molecule is not possible in the crystal packing.

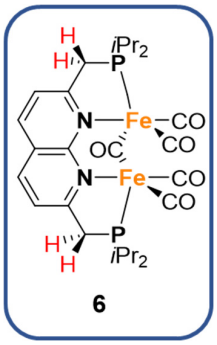

6

Crystals of **6** suitable for X-ray diffraction were grown from a saturated benzene solution at ambient temperature. The crystal structure contains neutral complex **6** and co-crystallized benzene molecules. One of the benzene molecules is located in a general position and another is located on an inversion center. Therefore, the asymmetric unit contains 1.5 benzene molecules. One of the isopropyl substituents of the ^{iPr}**PNNP** ligand in **6** is refined with a disorder model. Both the solid-state structure of **6** and of complex **5** show the same diiron pentacarbonyl core with the iron centers displaying heavily distorted trigonal bipyramidal geometries.

Packing of complexes 3 and 5 in the crystal

Complexes **3** and **5** are mono-anionic complexes with a potassium counter-ion. In complex **3**, a one-dimensional coordination polymer is formed that links the complexes with a potassium$^+$-$(THF)_2$ fragment through coordination of the oxygen atoms of the CO ligands, see figure S88 for the packing. In complex **5**, a one-dimensional coordination polymer is formed. All oxygen atoms of the five CO ligands are coordinated to a potassium$^+$(THF) fragment, see the packing of the structure in figure S89.

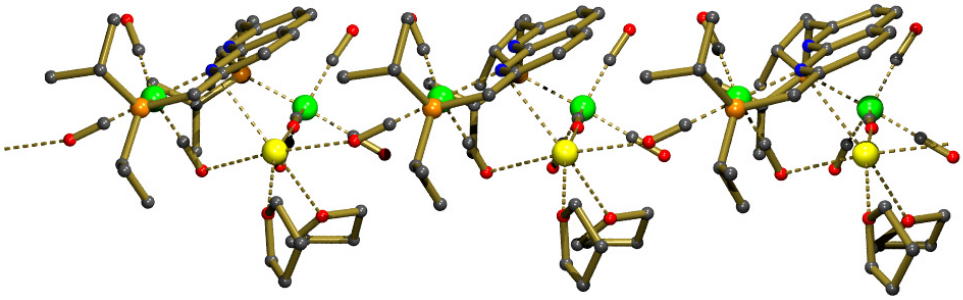

Figure S88: Coordination polymer in the crystal structure of **3**. Hydrogen atoms are omitted for clarity. Iron is drawn in green, potassium in yellow.

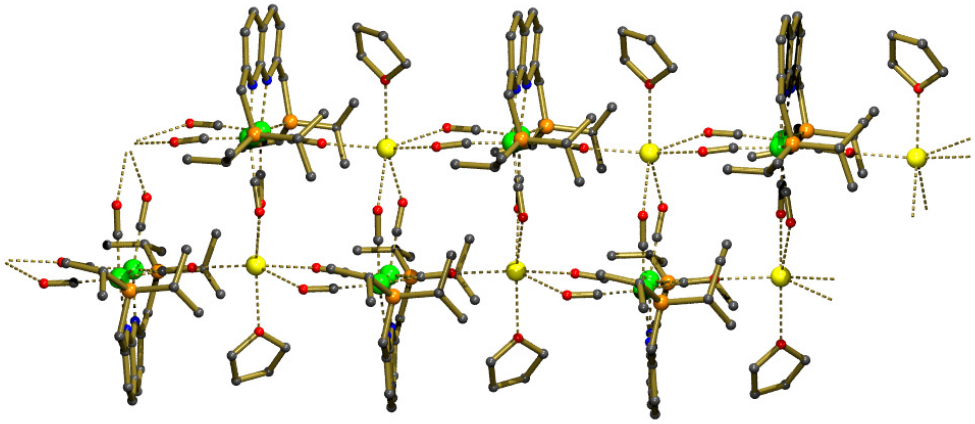

Figure S89: Coordination polymer in the crystal structure of **5**. Hydrogen atoms are omitted for clarity. Only the major disorder form is shown. Iron is drawn in green, potassium in yellow.

Computational methods

All calculations were performed using DFT with the ORCA program package, version 4.2.1.[28] All calculations were performed using the BP86[29] or the B3LYP[30] functional in combination with the scalar relativistically recontracted version of the Ahlrichs triple-ζ basis set def2-TZVP[31] on all atoms in the molecule. Additionally, the atom-pairwise dispersion correction with the Becke-Johnson damping scheme (D3BJ)[32] was used for all atoms in every calculation. For all structures, the geometry was optimized using the BP86 functional. For complexes **4** and **7**, the geometry was also optimized at the B3LYP level to allow accurate calculation of the EPR parameters. Single point calculations were performed at the B3LYP level for the computational evaluation of the BDFE values of the ligand's pseudobenzylic C–H bond in the various complexes and $^{i\text{Pr}}$**PNNP**. The atom coordinates used for geometry optimizations were taken from the single crystal X-ray diffraction structures. The keyword 'TightSCF' was included for tightly converging SCF calculations. Geometry optimizations were performed with the keyword 'TightOpt' to tightly converge the optimization.

Example of an input file for the geometry optimization of $^{i\text{Pr}}$**PNNP:**

```
! RKS BP86 Opt NumFreq def2-TZVP def2/J Grid4 NoFinalGrid
! TightSCF D3BJ TightOpt

%pal nprocs 24 end

%scf MaxIter 500 end


* xyz 0 1
[Cartesian coordinates here]
*
```

Example of an input file for the calculation of EPR parameters of complex **4**:

```
! UKS B3LYP def2-TZVP def2/J Grid4 NoFinalGrid
! TightSCF D3BJ TightOpt

%pal nprocs 24 end

%scf MaxIter 500 end

* xyz 0 2
[Cartesian coordinates here]
*

%eprnmr gtensor true ori CenterOfElCharge
Nuclei = all N { aiso, adip, fgrad, rho}
Nuclei = all H { aiso, adip, fgrad, rho}
Nuclei = all P { aiso, adip, fgrad, rho}
end
```

Example of an input file for an NBO calculation of complex **5**:

```
! RKS BP86 def2-TZVP def2/J Grid4 NoFinalGrid
! TightSCF D3BJ TightOpt

%nbo
NBOKEYLIST      = "$nbo plot archive file= [filename] nlmo bndidx $end"
end

%pal nprocs 24 end

%scf MaxIter 500 end


* xyz -1 1
[Cartesian coordinates here]
*
```

Optimized geometries of paramagnetic complexes

The geometry of the different diiron carbonyl complexes was optimized (BP86/def2-TZVP). The open shell paramagnetic complexes **4** and **7** show different geometry around the metal center Fe1 compared to their one-electron reduced counterparts complexes **5** and **3**, respectively. As expected for five coordinated low-spin Fe(0) carbonyl complexes, the Fe centers have (distorted) trigonal bipyramidal geometry in diamagnetic complexes **5** and **3**. However, the open shell paramagnetic Fe1 centers in complexes **4** and **7** display a distorted square pyramidal geometry. The spin density in these complexes is located primarily on iron (see main text) and the singly occupied molecular orbital (SOMO) for both these complexes is the d_{z^2} orbital that is oriented towards the sixth empty coordination site. In Figure S90, the optimized geometry of complexes **4** and **5** are presented. For complex **4**, the distance between the bridging CO ligand and Fe1 is increased (2.09 Å) compared to **5** (1.92 Å), opening up space for the SOMO. This change is more clearly observed when the geometries of **4** and **5** are optimized using the functional B3LYP (basis set def2-TZVP) with 2.71 Å for complex **4** and 1.92 Å for complex **5**. Because of the small metal-metal spacing in **4**, the angles around the basal ligands surrounding Fe2 deviate clearly from 120 ° as well. The geometry change is noticed clearly between complexes **3** and **7** as shown in Figure S91. A slightly distorted trigonal bipyramidal geometry is present on Fe1 in complex **3**. However, in complex **7** the basal CO ligands move away from another giving the paramagnetic Fe1 a square pyramidal geometry with the phosphine and the sixth empty coordination site on the axial positions. The spin density and SOMO are oriented towards the axial positions as shown in the main text.

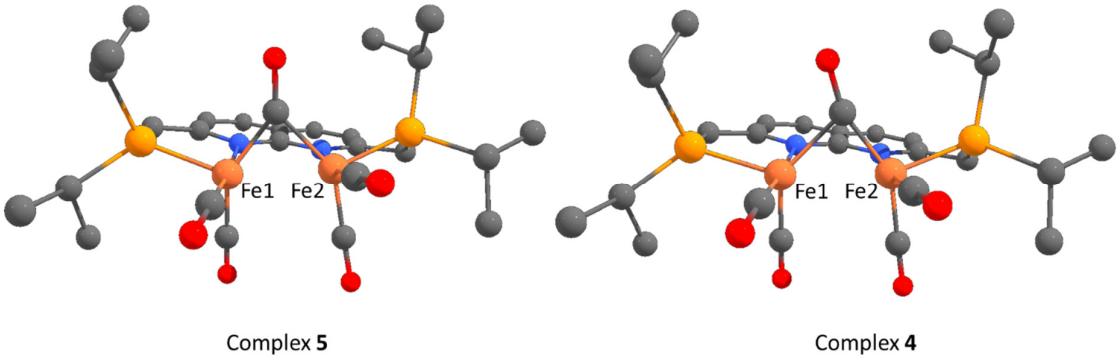

Figure S90: Geometry optimized structures (BP86/def2-TZVP) of complexes **4** and **5** displaying their change in geometry (hydrogen atoms are omitted for clarity).

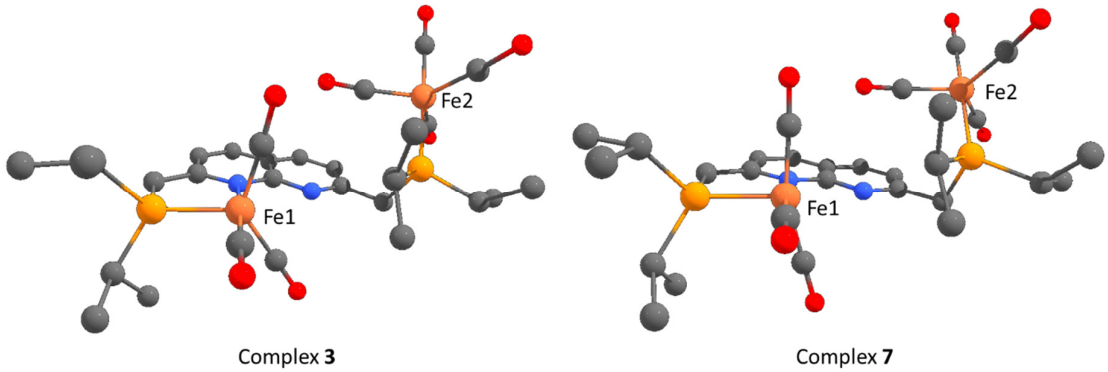

Figure S91: Geometry optimized structures (BP86/def2-TZVP) of complexes **3** and **7** displaying their change in geometry (hydrogen atoms are omitted for clarity).

DFT calculated BDFE of pseudobenzylic C–H bonds

The DFT calculated gas-phase bond dissociation free energy (BDFE) values of the pseudobenzylic C–H bond in ^{iPr}**PNNP** and various diiron carbonyl complexes described in this work were determined by comparison of the calculated single point energies (B3LYP/def2-TZVP) from geometry optimized structures (BP86/def2-TZVP). The homolytic bond cleavage reactions XH → X$^{\cdot}$ + H$^{\cdot}$ requires an accurate energy evaluation of both molecules (XH and X$^{\cdot}$) and the hydrogen atom (H$^{\cdot}$). In other work, it was shown that using this method to evaluate the bond dissociation enthalpies (BDE) from iridium amido and imido complexes leads to an underestimation of the BDE in the order of 4-5 kcal·mol^{-1}, which was explained by inaccurate treatment of the hydrogen atom by DFT methods.[33] To circumvent the necessity to calculate the energy of the hydrogen atom, an isodesmic reaction is evaluated computationally that transfers the hydrogen atom from the molecule of interest to an organic radical, as shown here below for complex **1**. The BDFE value can then be derived from the reaction energy (single point energy of products subtracted by starting compounds) that is calculated for the four components. To this end, the reaction energy is then added to the O–H BDFE of the phenoxyl radical (TBP) that has experimentally been determined (O–H BDFE$_{DMSO}$ = 80.6 kcal·mol^{-1})[34]. The resulting value obtained is the C–H BDFE of the molecule of interest.

TBP has been well studied in CPET reactivity, because of the stability of the radical species and its accessibility.[2] The O–H BDFE of TBP–H has to the best of our knowledge not been determined

experimentally in THF yet. Therefore, the O–H BDFE reported in DMSO (80.6 kcal·mol^{-1}) is used as a reference for the calculated C–H BDFE of ^{iPr}**PNNP** and diiron carbonyl complexes. Since the O–H BDFE of TBP–H varies between solvents ($BDFE_{benzene}$ = 76.7 kcal·mol^{-1}, $BDFE_{MeCN}$ = 77.1 kcal·mol^{-1}) (approx. 4 kcal·mol^{-1} between benzene and DMSO) and only gas phase energies were calculated, a systematic error in the obtained C–H BDFE is expected. The calculated BDFE for the C–H bond in **1** (66 kcal·mol^{-1}) agrees well with the experimentally determined value (70 kcal·mol^{-1}). The calculated BDFE values for the different compounds are shown in Table S5.

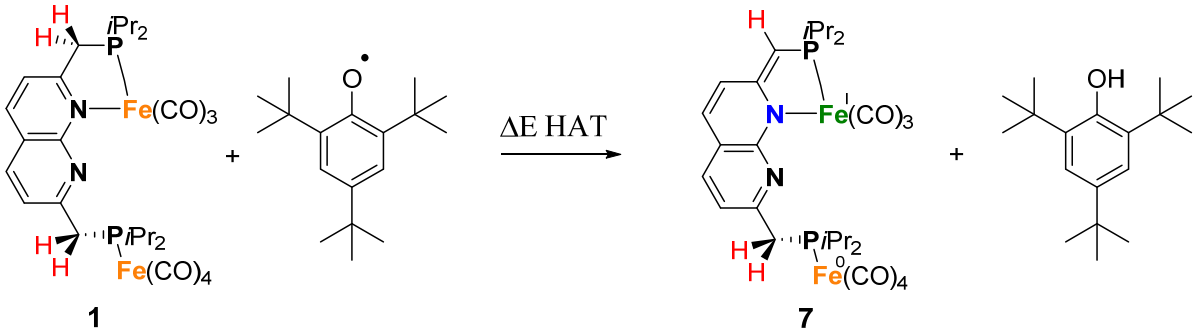

Figure S92: Isodesmic reaction that is computationally evaluated for the C–H BDFE calculation for complex **1**. The ΔE HAT calculated in this process depends on the O–H BDFE of TBP-H.

Table S5: DFT calculated and experimental BDFE C–H (O–H) values of the ligand and in various diiron carbonyl complexes.

Compound	***calculated BDFE (kcal·mol^{-1})***	***experimental BDFE (kcal·mol^{-1})***
^{iPr}**PNNP**	90	-
1	66	70
2	91	-
6	56	-
2,4,6-*t*Bu$_3$PhOH	-	80.6 (DMSO)

DFT calculated vibrational spectrum of complexes **4**, **5** and **6**

The DFT (BP86/def2-TZVP) calculated vibrational IR spectra of complexes **4**-**6** with indicated vibration modes are displayed in Figures S93-S99. All three complexes contain a diiron pentacarbonyl core that contain four terminal carbonyl ligands around the two iron centers and a bridging carbonyl ligand for complexes **5** and **6**. Paramagnetic complex **4** displays a semi-bridging carbonyl ligand that is closest to the Fe(0) center (C–Fe 1.84 Å) and further away from the Fe(I) center (C–Fe 2.09 Å). When the structure of complex **4** is optimized using the B3LYP functional, this effect is a lot more pronounced (for Fe(0) C–Fe 1.80 Å, for Fe(I) C–Fe 2.71 Å). The calculated position of the vibration of this bridging CO ligand is at 1788 cm^{-1}. Although a weak and sharp vibration is observed at 1633 cm^{-1} in the IR spectrum of **4** (Figure S40) we have assigned this to the vibration of the localized double bonds in the dearomatized ring (see Figure S98). This is in agreement with previously reported dinuclear complexes bearing a partially dearomatized PNNP ligand.[1] Moreover, the stretching vibrations of the bridging CO ligands in the IR spectra of **5** and **6** – complexes that are more electron rich and therefore expected to have a more activated bridging CO ligand – are at higher energies than the band observed at 1633 cm^{-1} in the IR spectrum of **4**. The expected higher degree of π-backdonation in **5** and **6** is observed in the calculated vibrational IR spectra of **4**-**6** show wherein the stretching frequencies of the bridging CO ligand in **5** and **6** is observed at lower energies than the semibridging carbonyl in **4.** All together, this suggests that no bridging CO is present in paramagnetic complex **4**.

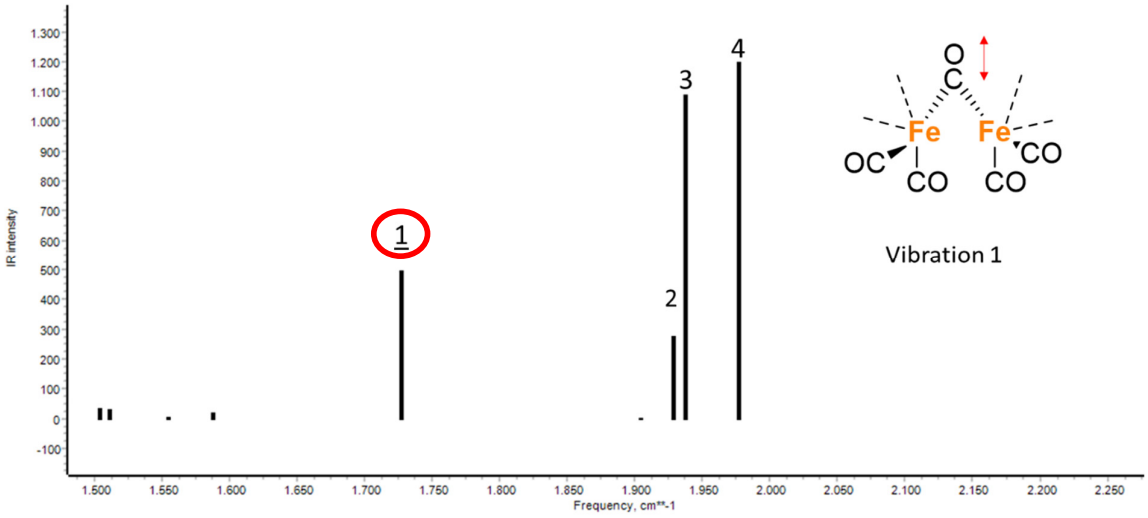

Figure S93: Zoom in of the DFT calculated (BP86/def2-TZVP) vibrational IR spectrum of complex **6** displaying the movement of the carbonyl ligands for vibration 1.

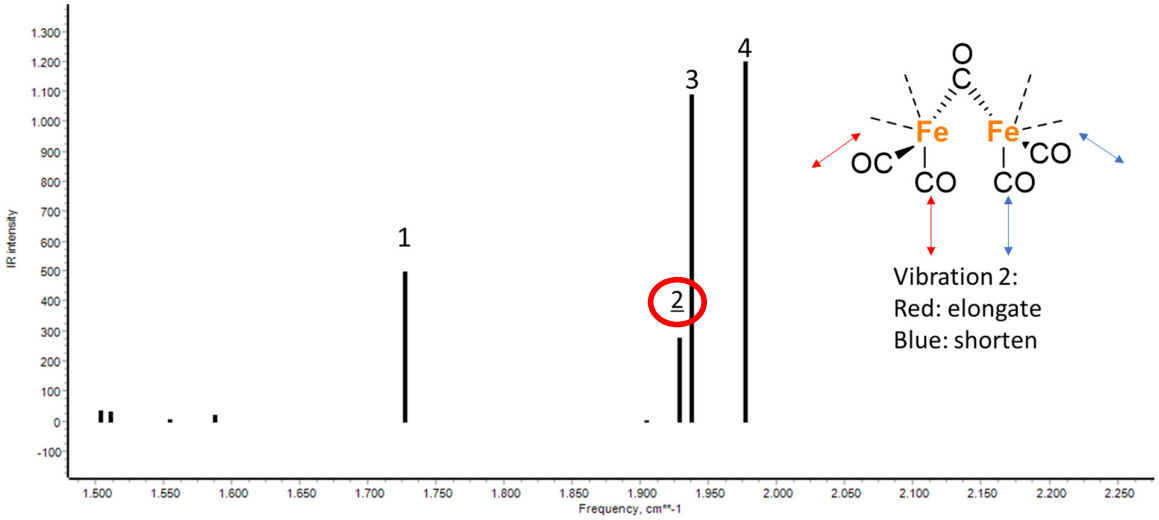

Figure S94: Zoom in of the DFT calculated (BP86/def2-TZVP) vibrational IR spectrum of complex **6** displaying the movement of the carbonyl ligands for vibration 2.

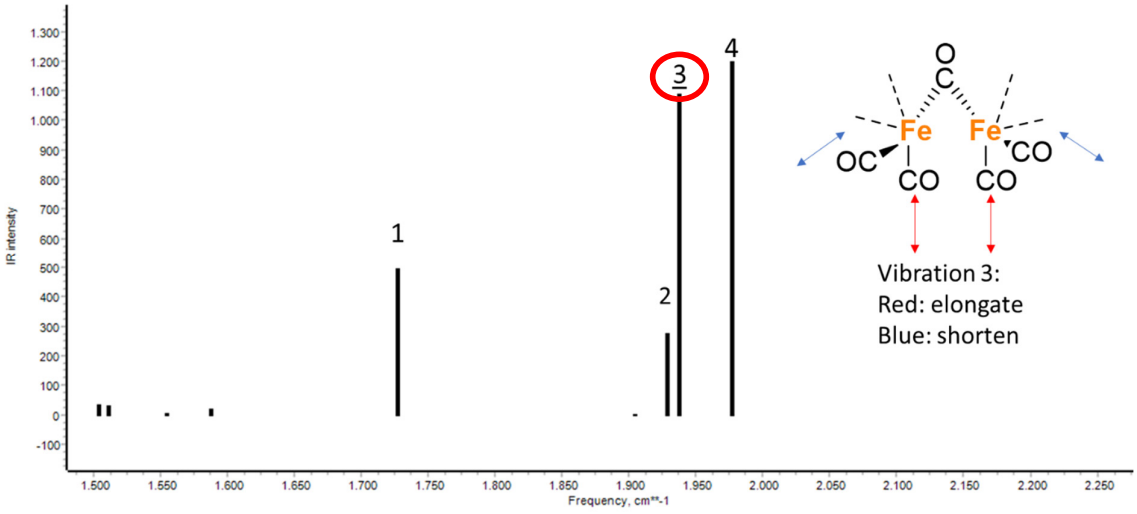

Figure S95: Zoom in of the DFT calculated (BP86/def2-TZVP) vibrational IR spectrum of complex **6** displaying the movement of the carbonyl ligands for vibration 3.

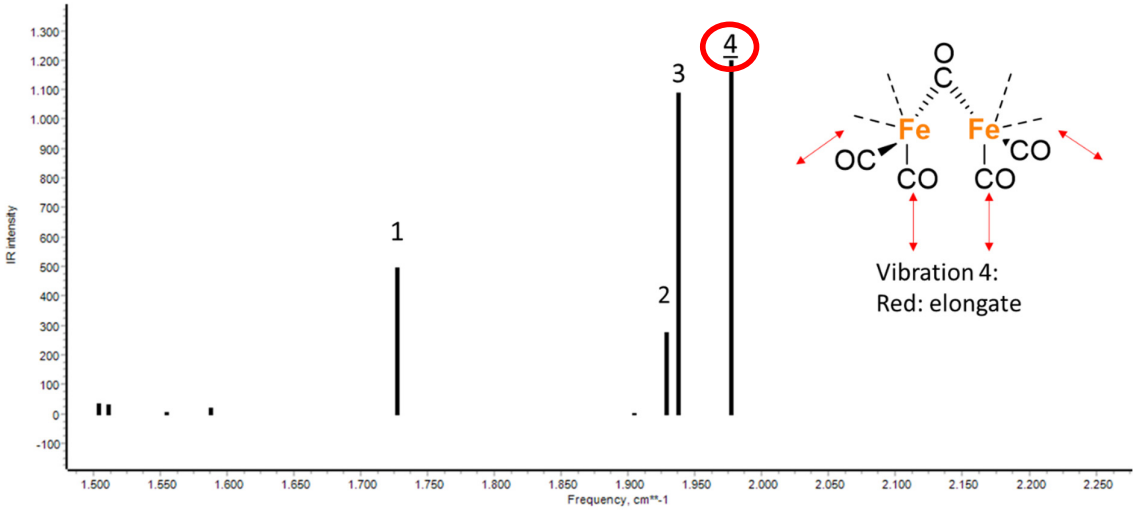

Figure S96: Zoom in of the DFT calculated (BP86/def2-TZVP) vibrational IR spectrum of complex **6** displaying the movement of the carbonyl ligands for vibration 4.

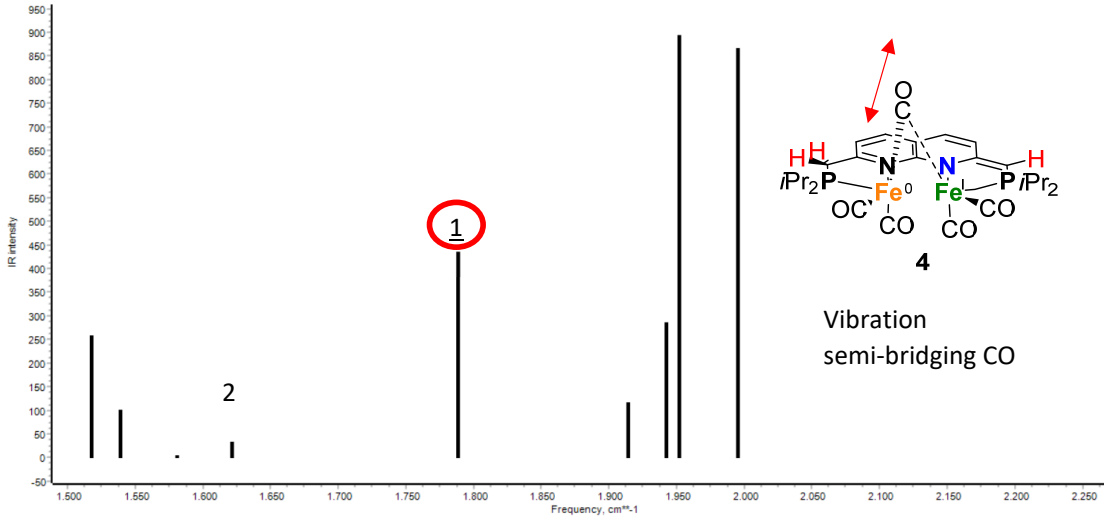

Figure S97: Zoom in of the DFT calculated (BP86/def2-TZVP) vibrational IR spectrum of complex **4** displaying the movement of the semi-bridging carbonyl ligand for vibration 1.

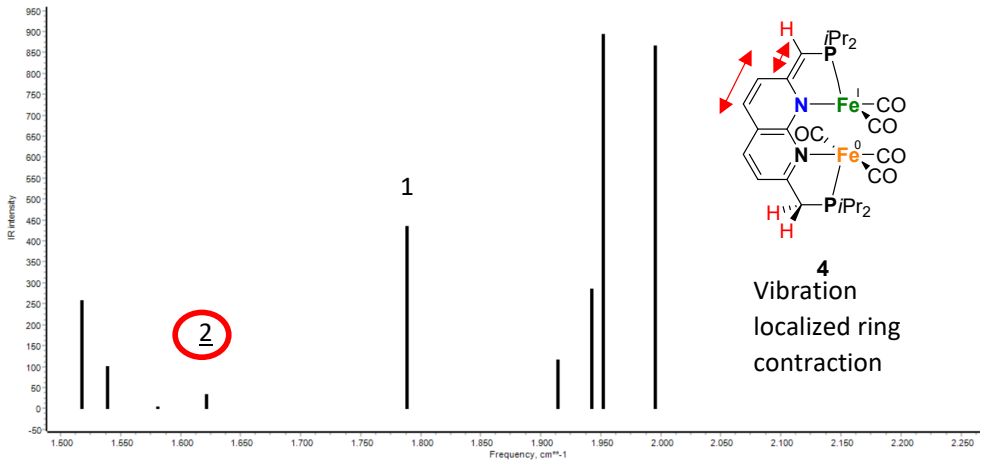

Figure S98: Zoom in of the DFT calculated (BP86/def2-TZVP) vibrational IR spectrum of complex **4** displaying the movement of the localized double bonds in the dearomatized ring in the ligand for vibration 2.

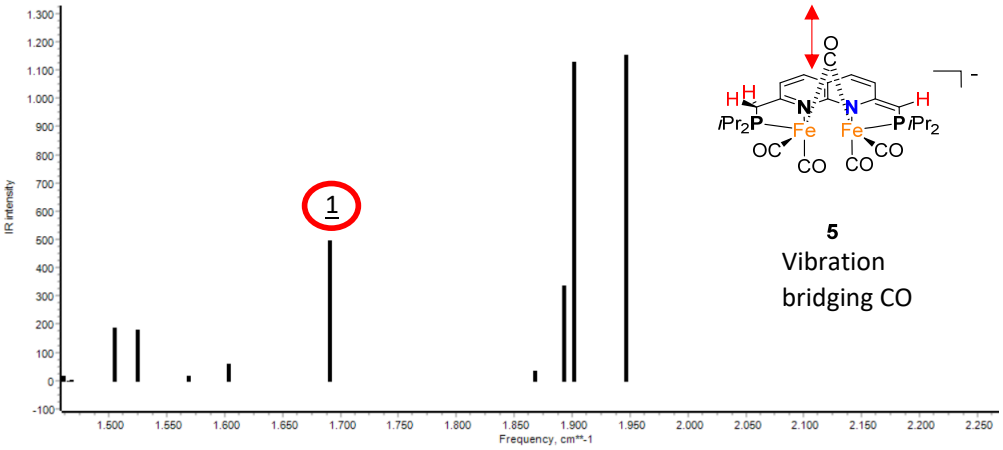

Figure S99: Zoom in of the DFT calculated (BP86/def2-TZVP) vibrational IR spectrum of complex **5** displaying the movement of the bridging carbonyl ligand for vibration 1.

Protonation and reduction of complex **6**

In order to gain insight into how H_2 is generated upon the electrochemical reduction of **6** in the presence of acid, we investigated the reactivity of **6** with a proton source and/or chemical reductants. Addition of an excess of phenol or TEA to complex **6** in THF does not lead to a color change. However, the ^{31}P and ^{1}H NMR spectra of complex **6** are affected when an excess of TEA is added. With the addition of 1 equiv of TEA to complex **6** in THF, a broader resonance is observed in the $^{31}P\{^{1}H\}$ NMR spectrum. Treating complex **6** with 5 equiv of TEA leads to the observation of a broad resonance of complex **6** in combination with additional resonances (see Figure S100). Furthermore, the ^{1}H NMR spectrum of the reaction mixture display a broad resonance in the aromatic region and two new aromatic resonances (see Figure S101). It appears that the resonances for complex **6** are broadened and are not clearly identified. In the hydridic region there are no resonances observed, indicating that a clear protonation of the metal center is not observed in THF. The broad resonances of complex **6** could be explained by an equilibrium of **6** with a protonated species. Similar observations are made in MeCN-h_3 solution as shown in Figures S102 and S103. However, in this case a broad signal in the hydride region of the ^{1}H NMR spectrum is also observed. These observations suggest that in the presence of an excess TEA, the diiron core in **6** can be protonated.

In light of the observation that protonation of complex **6** can lead to iron hydride species, a frozen THF solution (cooled by a liquid N_2 bath) of complex **6** was treated with one equiv of $[H{\cdot}OEt_2]BArF_{24}$ (Brookhart's acid) in THF in a J-Young NMR tube. Upon thawing of the frozen solution, a green-brown mixture formed and ^{31}P and ^{1}H NMR analysis showed full conversion of **6** to multiple species. The $^{31}P\{^{1}H\}$ NMR spectrum displays four resonances as observed in Figure S104. The ^{1}H NMR spectrum (Figure S105) show multiple sets of aromatic resonances for the different products. Notably, two distinct hydride resonances are observed at -7.50 ppm (a doublet of doublets) and at -8.15 ppm (triplet), respectively. Given that no H_2 formation was observed in this reaction, the green-brown mixture was frozen and was treated with one equiv of KC_8 suspended in THF. Upon thawing of the mixture, gas formation was observed leading to a dark brown solution. The ^{1}H NMR spectrum of this mixture displays only broad resonances suggestive of the formation of paramagnetic species. The broadness of the resonances prevented observation of H_2 in the ^{1}H NMR spectrum, but headspace analysis by GC, qualitatively confirmed the presence of H_2. This indicates that stoichiometric protonation of the complex followed by reduction results in H_2 formation.

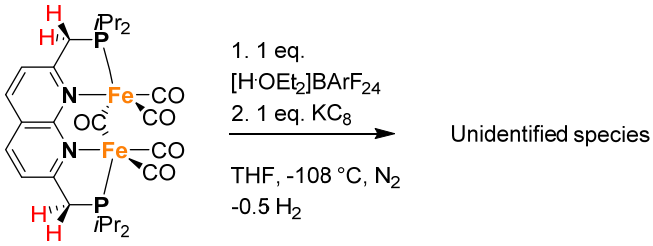

6

As described in the previous section, stoichiometric protonation using a (strong) acid leads to iron hydride complexes that release H_2 after reduction. Given that the one-electron reduction of **6** becomes irreversible in the presence of acid, yet is still observed, we decided to investigate the chemical reduction of **6** followed by treatment with acid. To this end, a solution of complex **6** in THF was frozen in an J-Young NMR tube and then treated with one equiv of KC_8. Upon thawing, a dark brown mixture was obtained that was analyzed by NMR spectroscopy. The $^{31}P\{^{1}H\}$ NMR spectrum shows full

conversion of **6** without the appearance of any new resonance (see Figure S106). The ^{1}H NMR spectrum contains a few broad resonances of low intensity (see Figure S107), which suggests that a paramagnetic complex has formed. When this mixture was again frozen using a liquid nitrogen bath, one equiv of TEA in THF was added and the NMR tube was closed immediately. Upon thawing of the frozen solution, gas formation was observed, and a brown solution formed. According to ^{31}P and ^{1}H NMR analysis, complex **6** was formed after protonation. However, the resonances in the ^{31}P{^{1}H} NMR spectrum (Figure S106) and many resonances in the ^{1}H NMR spectrum (Figure S107) are broadened. A singlet at 4.55 ppm indicates the presence of dissolved H_2, which was confirmed by headspace analysis of this NMR tube using GC. This shows that stoichiometric reduction followed by protonation leads to the formation of H_2 concomitant with re-formation of complex **6**. Direct reduction of the proton source by excess KC_8 still remaining in the NMR tube was ruled out by performing the reaction with substoichiometric amounts of the reductant and acid (0.5 equiv), which also led to the regeneration of complex **6** and formation of H_2.

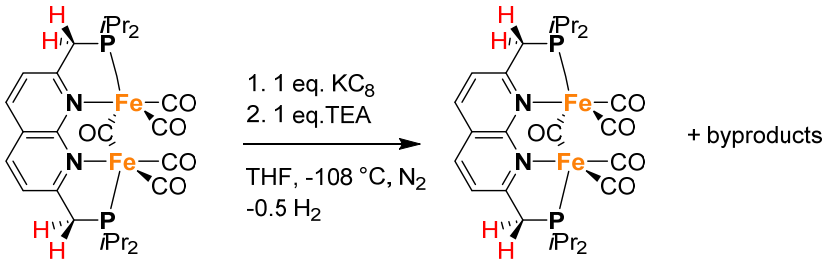

6 **6**

Altogether, these results show that H_2 formation is possible by either first reducing **6** and then protonating it and vice versa. However, it is currently still unclear how H_2 is formed under the electrochemical conditions, and future studies will focus on obtaining additional mechanistic understanding.

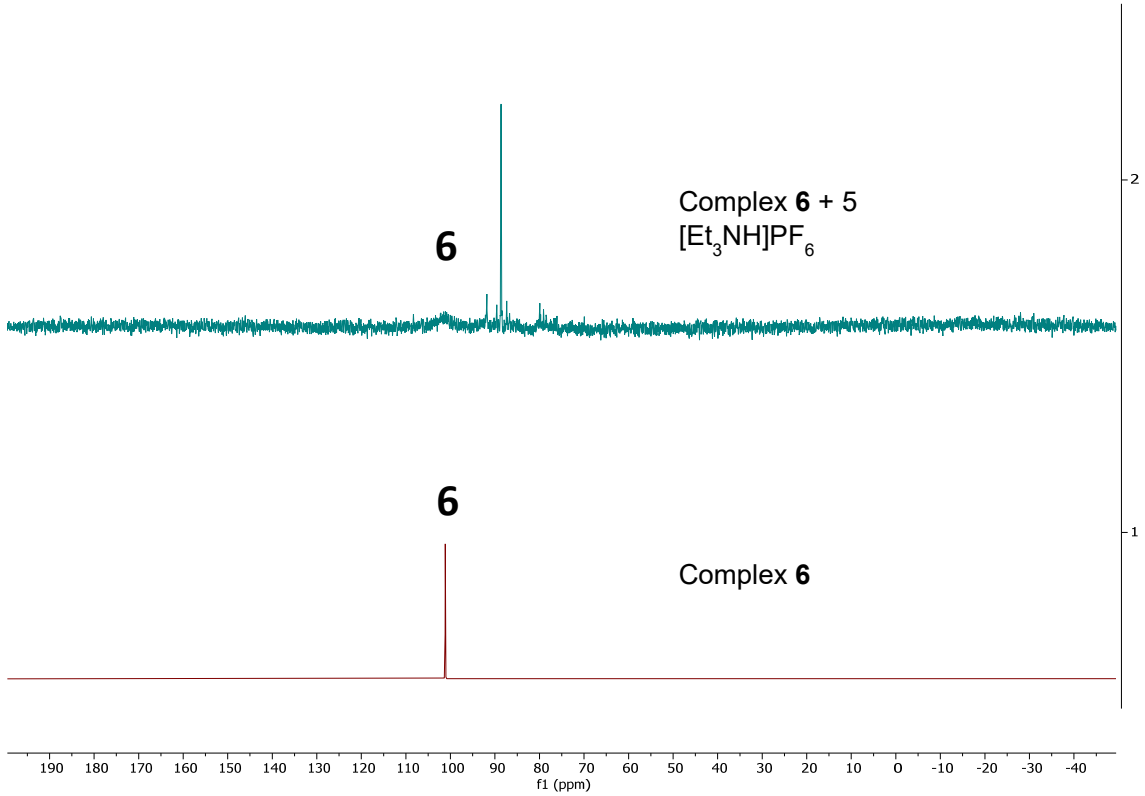

Figure S100: The stacked $^{31}P\{^{1}H\}$ NMR spectra of the reaction between complex **6** and 5 equiv of TEA after 4 h in THF-h_8 (top spectrum) or THF-d_8 (bottom) at 298 K. The top spectrum displays the spectrum of the reaction mixture, the bottom spectrum is a reference spectrum for complex **6**.

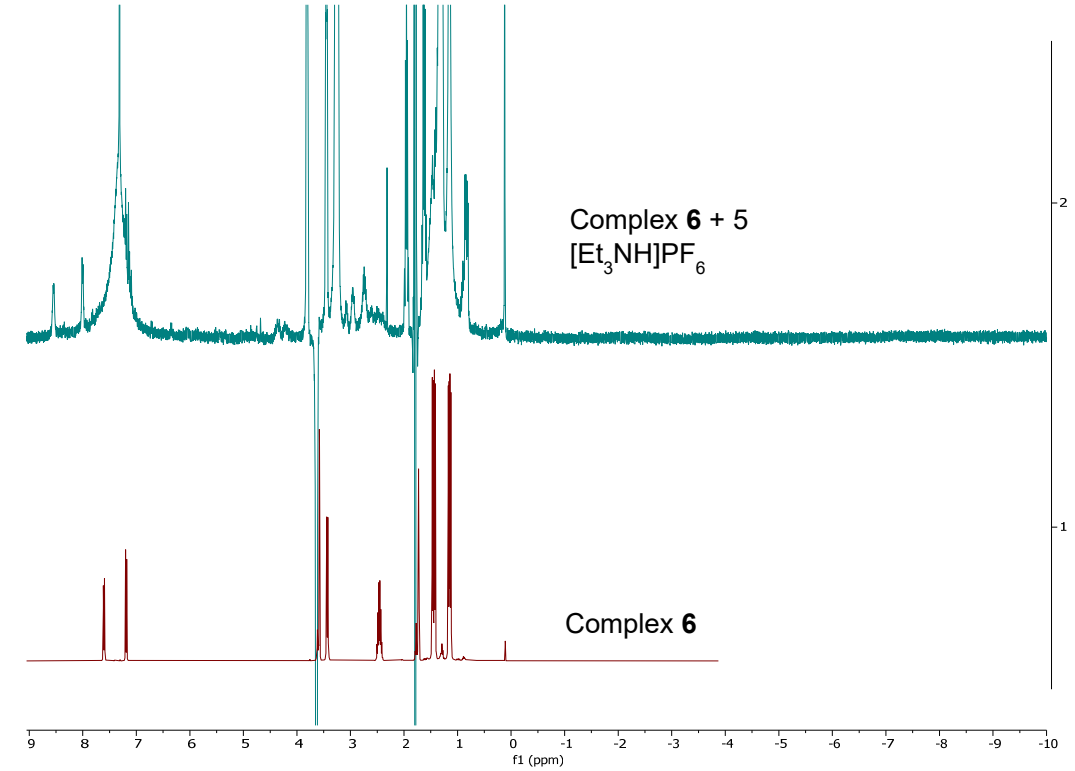

Figure S101: The stacked ^{1}H NMR spectra of the reaction between complex **6** and 5 equiv of TEA after 4 h in THF-h_8 (top spectrum) or THF-d_8 (bottom) at 298 K. The top spectrum displays the spectrum of the reaction mixture, the bottom spectrum is a reference spectrum for complex **6**.

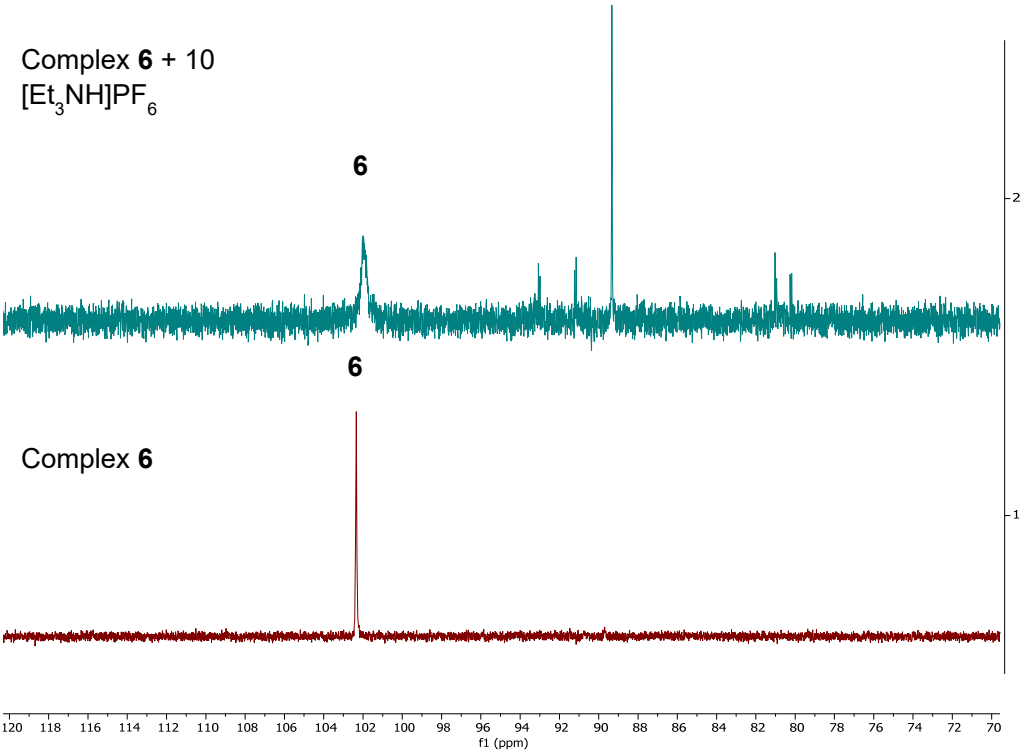

Figure S102: The stacked ^{31}P{^{1}H} NMR spectra of the reaction between complex **6** and 10 equiv of TEA after 1 h in MeCN-h_3 at 298 K. The top spectrum displays the spectrum of the reaction mixture, the bottom spectrum is a reference spectrum for complex **6**.

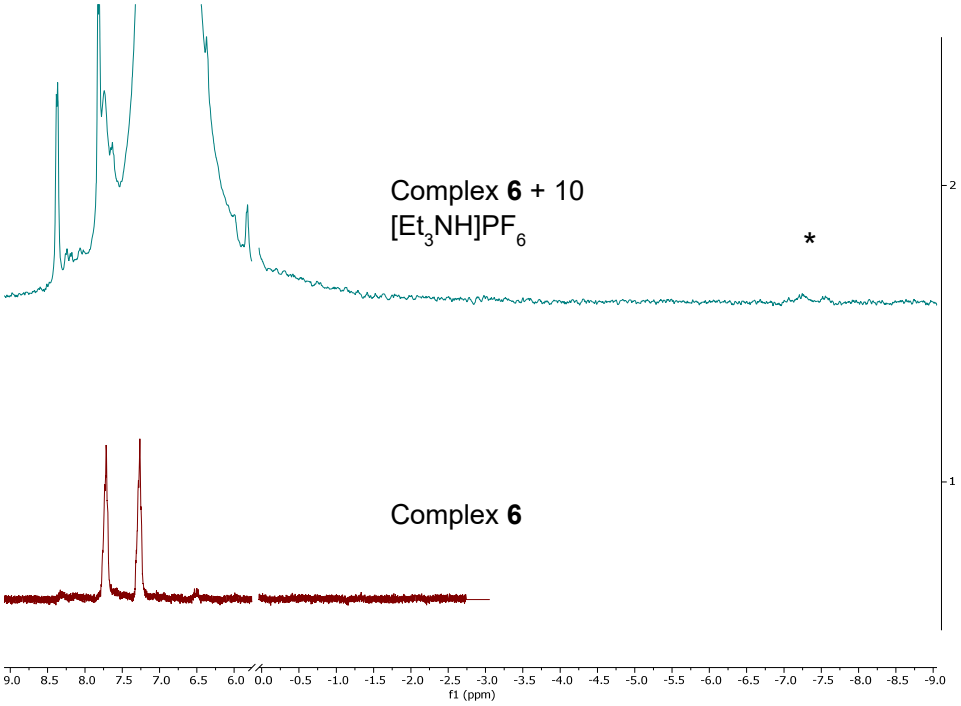

Figure S103: The stacked ^{1}H NMR spectra displaying the aromatic and hydridic region of the reaction between complex **6** and 10 equiv of TEA after 1 h in MeCN-h_3 at 298 K. The top spectrum displays the spectrum of the reaction mixture, the bottom spectrum is a reference spectrum for complex **6**. The resonances with a star are assigned to hydridic protons.

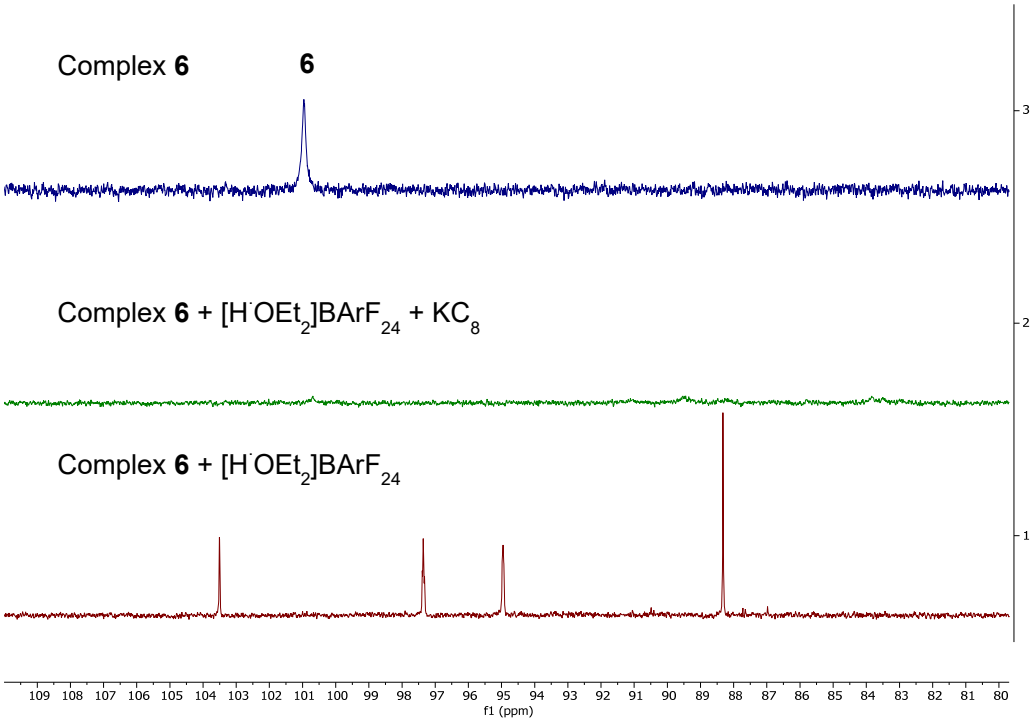

Figure S104: The stacked ^{31}P{^{1}H} NMR spectra of the reaction between complex **6** and 1 equiv of Brookhart's acid (bottom) followed by reduction using 1 equiv KC_8 (middle) in THF-h_8 at 298 K. The top spectrum displays a reference spectrum for complex **6**.

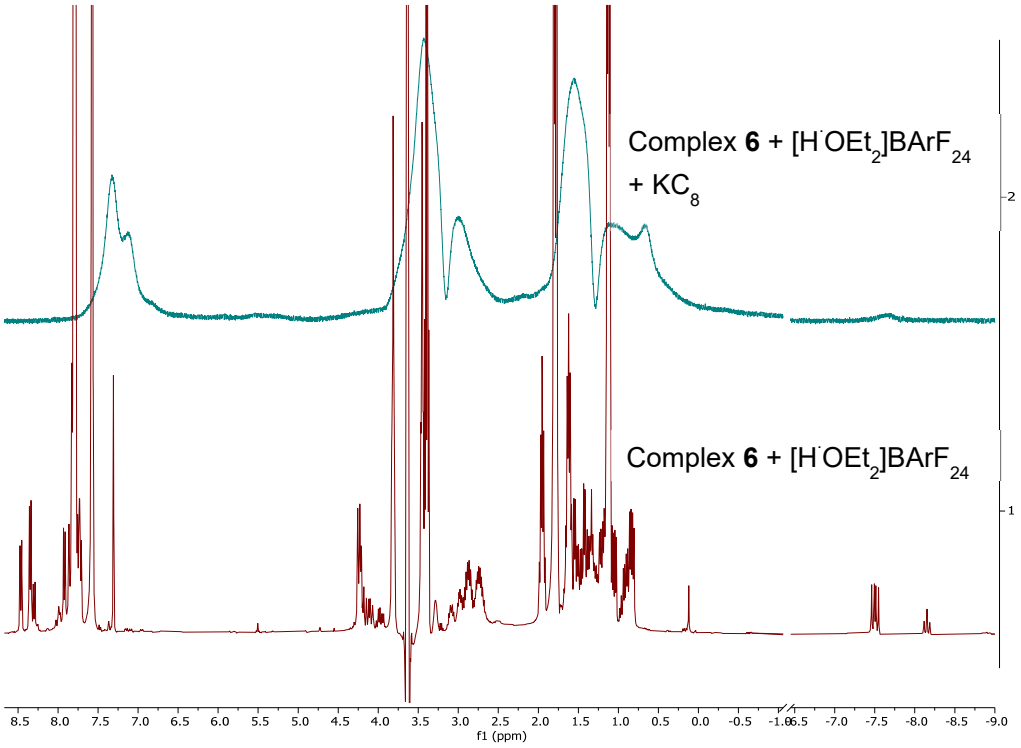

Figure S105: The stacked ^{1}H NMR spectra of the reaction between complex **6** and 1 equiv of Brookhart's acid (bottom) and followed by reduction using 1 equiv KC_8 (top) in THF-h_8 at 298 K. Broad resonances are observed after reduction as seen in the top.

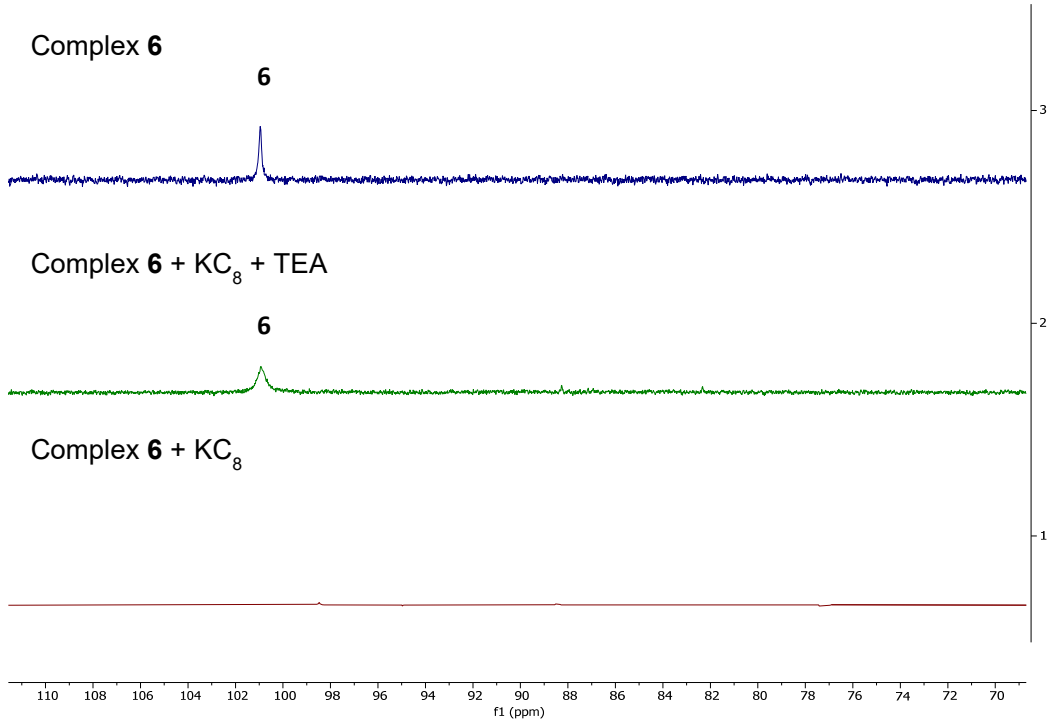

Figure S106: The stacked $^{31}P\{^{1}H\}$ NMR spectra of the reaction between complex **6** and 1 equiv of KC_8 (bottom) followed by protonation using 1 equiv TEA (middle) in THF-h_8 at 298 K. The top spectrum displays a reference spectrum for complex **6**.

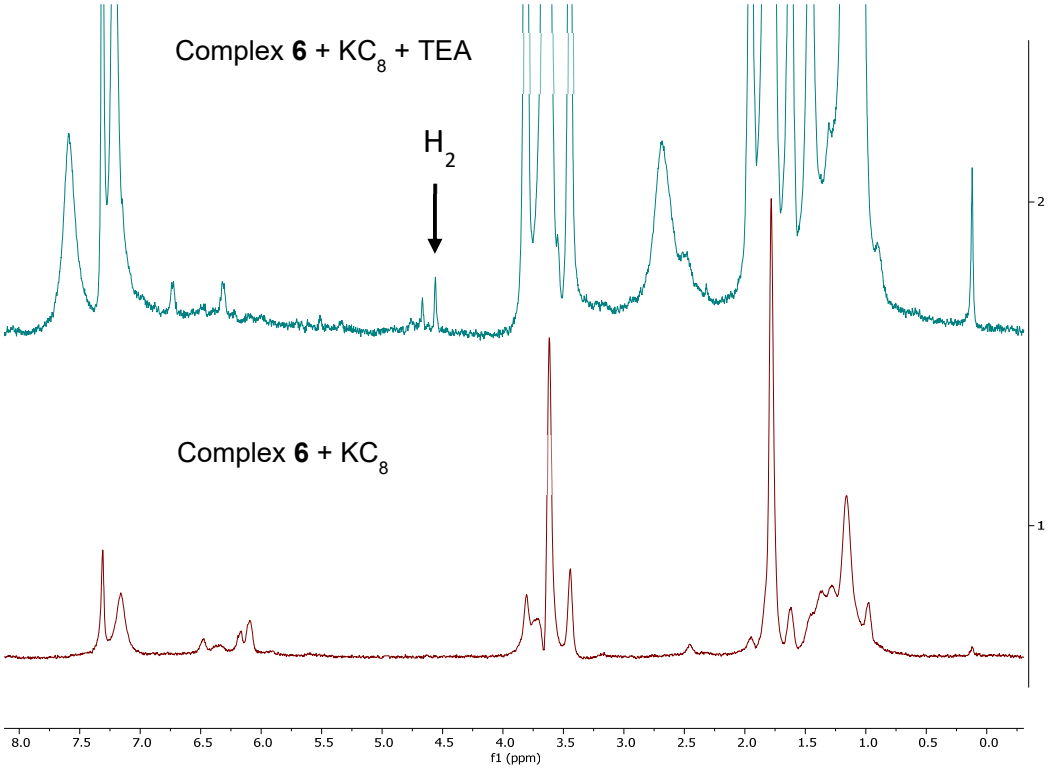

Figure S107: The stacked ^{1}H NMR spectra of the reaction between complex **6** and 1 equiv of KC_8 (bottom) and followed by reduction using 1 equiv TEA (top) in THF-h_8 at 298 K. After the protonation, the resonances become broad, but have a much higher intensity.

Bulk electrolysis using complex **6** and TEA

Having established that complex **6** shows activity for the electrochemical hydrogen evolution reaction in CV experiments, an initial bulk electrolysis experiment using 1 mM complex **6** with 10 mM TEA in THF with a 0.2 M [*n*-Bu_4N]PF_6 electrolyte was performed in a 2-compartment electrolysis cell. A rotating glassy carbon working electrode (5mm, 800 rpm), platinum wire counter electrode (behind a fine glass filter) and Ag/$AgNO_3$ double junction reference electrode were used. A steady flow of N2 was bubbled through the mixture at a rate of 5.0 mL/min. The electrochemical cell was placed in line with a gas GC that injects a sample every minute to detect and quantify H_2 gas. A constant potential of -2.4 V vs. Fc^+/Fc was applied for 60 min. During the measurement, the orange to brown solution lost some of the intensity of the color.

The measured hydrogen evolution, charge consumption and Faradaic efficiency of the measurements of one hour are summarized in Table S6. In total 3600 mL N_2 was passed through the system in 60 min containing an average H_2 concentration of 309 ppm, corresponding to 4.08 µmol H_2, with a Faradaic efficiency of 54% based on the consumed charge. A Faradaic efficiency close to 100% is expected for a selective catalyst for the hydrogen evolution reaction. The low Faradaic efficiency observed for this bulk electrolysis experiment is ascribed to an unstable complex under these conditions, as indicated by the color change.

Table S6: Bulk electrolysis 1 mM complex **6** at -2.4 V vs. Fc^+/Fc.		
10 mM [Et_3NH]PF_6 in THF (0.2 M electrolyte)		
Hydrogen		
Flow rate	5	mL/min
Time	3600	s
	60	min
Volume	300	ml
Pressure	1	bar
Gas constant	83.14	K mol cm^3 bar
Temperature	273	K
Moles of N_2	0.013217478	mol
concentration of product	309	ppm
moles of product 4.0842E-06		
Necessary Coulombs	0.7881	C
Consumed Coulombs	1.456	C
Faraday constant	96485.33	C/mol e
Faradaic efficiency	54.13%	

References

[1] E. Kounalis, M. Lutz, D. L. J. Broere, *Chem. Eur. J.* **2019**, *25*, 13280–13284 ; E. Kounalis, M. Lutz, D. L. J. Broere *Organometallics* **2020**, *39*, 585-592

[2] V. W. Manner, T. F. Markle, J. H. Freudenthal, J. P. Roth, J. M. Mayer, *Chem. Commun.* **2008**, 256–258.

[3] F. G. Bordwell, J. C. Branca, J. E. Bares, R. Filler, *J. Org. Chem.* **1988**, *53*, 780-782.

[4] G. C. Vougioukalakis, M. M. Roubelakis, M. Orfanopoulos, A. Paraskevi, *J. Org. Chem* **2010**, *75*, 4124–4130.

[5] S. Saba, R. Hernandez, C. Chin Choy, K. Carta, Y. Bennett, S. Bondi, S. Kolaj, C. Bennett, *J. Fluor. Chem.* **2013**, *153*, 168-171.

[6] S. Stoll, A. J. Schweiger, *Magn. Reson.* **2006**, *178*, 42−55. EasySpin is available free of charge at http://easyspin.org

[7] Thomas Casey (2021). cwEPR (https://www.mathworks.com/matlabcentral/fileexchange/73292-cwepr), MATLAB Central File Exchange.

[8] a) F. Kong, S. Gu, C. Liu, D. A. Dickie, S. Zhang, T. B. Gunnoe, *Organometallics* **2020**, *39*, 3918–3935; b) E. R. M. Habraken, A. R. Jupp, M. B. Brands, M. Nieger, A. W. Ehlers, J. C. Slootweg, *Eur. J. Inorg. Chem.* **2019**, *2019*, 2436–2442.

[9] Metal-Ligand Interactions: From Atoms, to Clusters, to Surfaces, Vol 378 (Eds.: D.R. Salahub, N. Russo), Springer, 1992.

[10] F. G. Bordwell, *Acc. Chem. Res.* **1988**, *21*, 456–463.

[11] K. Abdur-Rashid, T. P. Fong, B. Greaves, D. G. Gusev, J. G. Hinman, S. E. Landau, A. J. Lough, R. H. Morris, *J. Am. Chem. Soc.* **2000**, *122*, 9155–9171.

[12] The known pK_a^{DMSO} value was converted to pK_α^{THF} using Morris' empirical relationship: pK_a^{DMSO}(HA) = 0.85 pK_α^{THF} (HA) – 9.6.

[13] D. A. Bors, M. J. Kaufman, A. Streitwieser, *J. Am. Chem. Soc.* **1985**, *107*, 6975–6982.

[14] J. F. Coetzee, B. K. Deshmukh, C.-C. Liao, *Chem. Rev* **1990**, *90*, 827–835.

[15] a) F. G. Bordwell, *Acc. Chem. Res.* **1988**, *21*, 456–463; b) I. M. Kolthoff, M. K. Chantooni, S. Bhowmik, *J. Am. Chem. Soc.* **1968**, *90*, 23–28.

[16] R. M. Fuoss, *J. Am. Chem. Soc.* **1958**, *80*, 5059–5061.

[17] M. J. Kaufman, S. Gronert, A. Streitwieser, *J. Am. Chem. Soc.* **1988**, *110*, 2829–2835.

[18] S. Tretiakov, L. Witteman, M. Lutz, M. Moret, *Angew. Chemie Int. Ed.* **2021**, *60*, 9618–9626; *Angew. Chem.* **2021**, *133*, 9704-9712.

[19] A. M. M. Schreurs, X. Xian, L. M. J. Kroon-Batenburg, *J. Appl. Cryst.* **2010**, *43*, 70-82.

[20] G. M. Sheldrick, **2014**, SADABS. Universität Göttingen, Germany.

[21] G. M. Sheldrick, *Acta Cryst.* **2015**, *A71*, 3-8.

[22] G. M. Sheldrick, *Acta Cryst.* **2015**, *C71*, 3-8.

[23] A. L. Spek, *Acta Cryst.* **2009**, *D65*, 148-155.

[24] J. Pickardt, L. Rösch, H. Schumann, *J. Organomet. Chem.* **1976**, *107*, 241–248.

[25] a) M. R. Ringenberg, F. Wittkamp, U.-P. Apfel, W. Kaim, *Inorg. Chem.* **2017**, *56*, 7501–7511; b) H. T. Dieck, G. Hahn, *Z. Anorg. Allg. Chem.* **1989**, *577*, 74–82.

[26] a) A. K. Hickey, C. H. Chen, M. Pink, J. M. Smith, *Organometallics* **2015**, *34*, 4560–4566; b) J. P. Shupp, A. R. Rose, M. J. Rose, *Dalt. Trans.* **2017**, *46*, 9163–9171.

[27] a) C. M. Alvarez, M. A. Alvarez, M. E. García, R. González, A. Ramos, M. A. Ruiz, *Inorg. Chem* **2011**, *50*, 10937-10948; b) R. J. Wright, W. Zhang, X. Yang, M. Fasulo, T. D. Tilley, *Dalt. Trans.* **2012**, *41*, 73–82.

[28] F. Neese, The ORCA program system. *Wiley Interdiscip. Rev. Comput. Mol. Sci.* **2012**, *2*, 73–78.

[29] a) A. D. Becke, *J. Chem. Phys.* **1986**, *84*, 4524-4529; b) J. P. Perdew, *Phys. Rev. B* **1986**, *33*, 8822–8824.

[30] A.D. Becke, *J. Chem Phys.* **1993**, *98*, 5648-5652.

[31] a) D. A. Pantazis, X.-Y. Chen, C. R. Landis, F. Neese, *J. Chem. Theory Comput.* **2008**, *4*, 908–919; b) F. Weigend, R. Ahlrichs, *Phys. Chem. Chem. Phys.* **2005**, *7*, 3297–3305.

[32] a) S. Grimme, J. Antony, S. Ehrlich, H. Krieg, *J. Chem. Phys.* **2010**, *132*, 154104; b) S. Grimme, S. Ehrlich, L. Goerigk, *J. Comput. Chem.* **2011**, *32*, 1456–1465.

[33] M. G. Scheibel, J. Abbenseth, M. Kinauer, F. W. Heinemann, C. Würtele, B. de Bruin, S. Schneider, *Inorg. Chem.* **2015**, *54*, 9290–9302.

[34] J. J. Warren, T. A. Tronic, J. M. Mayer, *Chem. Rev.* **2010**, *110*, 6961–7001.